Flow and diffusion in microfluidic environments bounded by fluid walls with applications in neuroscience

Federico Nebuloni

Kellogg College

Department of Engineering Science

University of Oxford

Academic supervisor

Prof. Edmond J. Walsh

September 2023

To Cesare Nebuloni,
the father and engineer I hope to become,
this thesis is dedicated to you.
One day we will read it together.

Table of Contents

Abstract 6
Acknowledgments 7
Chapter 1: Introduction 8
Objectives 10
List of Publications 12
Chapter 2: Literature review 13
Origins of microfluidics 13
Engineered cell cultures and their relevance 15
Open Microfluidics 17
Chapter 3: A primer on fluid-walled microfluidics 20
Sessile drops 20
Conduits 22
Flows through fluid walls 23
Interfacial tension 25
Chapter 4: Stable diffusion gradients in microfluidic conduits bounded by fluid walls 29
Abstract 29
Introduction 30
Theory 32
Morphing fluid walls 32
Parallel laminar streams 34
Diffusion gradients across parallel streams 34
Materials and Methods 37
Reagents 37
Microscopy and imaging 37
Circuit fabrication 38
Infusion pumps and tubing 38
Determining h(z) from fluorescence intensity 38
Determining diffusion gradients of fluorescein across conduits 39
Results 39
Deriving a calibration curve 40
Diffusion gradients across parallel streams 42
Discussion 46
References 50
Supplementary Information 52
Chapter 5: Flow in fluid-walled conduits driven by Laplace pressure 58

Abstract **58**
Introduction **59**
Problem formulation **60**
Governing equation **62**
Comparison with the numerical solution **65**
Drainage time **66**
Experimental setup **67**
Results **68**
Source drops with contact angles smaller than 40° 68
Source drops with contact angles greater than 40° 69
Discussion **71**
Significance and conclusions **73**
References **74**
Chapter 6: A fluid-walled microfluidic platform for human neuron microcircuits and directed axotomy **77**
Abstract **77**
Introduction **78**
Results **79**
Jet-printing of fluid-walled micro-circuits shaped like dumbbells 79
Local pressures in dumbbells 81
Ensuring cells remain where deposited 83
Axons outgrow from CNs through the conduit to the distal chamber 85
A unidirectional circuit between cortex and striatum 87
Axotomy using a micro-jet 88
Regeneration after axotomy 90
Discussion **92**
Materials and methods **93**
Fluorocarbon 40 (FC40) 93
The fluid printer 94
Generation of iPSC-derived post-mitotic cortical neurons 94
Generation of iPSC-derived post-mitotic medium spiny neurons 94
Fabrication of dumbbells 95
Maturation media used for culturing in dumbbells 95
Plating CNs in left-hand chambers and transduction 96
Varying conditions on d 0 96
Culturing CNs in dumbbells without MSNs after d 0 97
Culturing CNs in dumbbells with MSNs after d 0 97
Axotomy 97
Imaging 98
Immunostaining 98

Measuring pressures and volumes in chambers 99
Statistical analysis 99
References 101
Supplementary Information 106
Determination of concentration gradients in dumbbells 106
Chapter 7: Discussion 114
Chapter 8: Conclusions and Future developments 117
Conclusions 117
Future developments 118
Laplace pressure in drops with non-circular footprints 118
Three-dimensional (3D) cultures within fluid-walled microfluidics 119
Connecting of neuronal 3D cultures/organoids 121
References 123

Abstract

Efforts towards the recapitulation of in-vivo systems in vitro remains a key goal of biological sciences. Microfluidic developments have the potential to revolutionise biology assays by providing better spatial and temporal control of cellular microenvironments. To this end, a wide range of microfluidic platforms have been proposed in literature to generate more biologically relevant and advanced cell-based models for drug discovery. However, less than 10% of microfluidics articles have authorship outside of core engineering or related disciplines, even fewer in pure biological sciences journals where traditional methods remain unchanged for decades. There are many reasons for this; some relevant ones to this thesis include the biocompatibility of the materials used to fabricate microfluidic platforms, poor ability to fabricate microenvironments on-demand and the inaccessibility of cells behind solid walls. Our group has led the development of a new microfluidics approach to overcome many existing limitations by forming microenvironments inside standard Petri dishes and confining them using 'fluid walls' (interfaces between immiscible liquids) rather than solid ones. This allows the microfluidic environments to be naturally biocompatible, easy to fabricate, integrated into traditional biology workflows, and cells are accessible everywhere simply by piercing through the bounding fluid interface. In addition, the method enables the microenvironments to be reshaped as fluid walls can be destroyed and rebuilt at will without harming the cultured cells.

The innovative fluid-walled technology also introduces an innovative engineering challenge: during flows, fluid walls shape is dependent on pressure and can morph in response to pressure changes. This thesis characterises properties of such morphing microenvironments to derive semi-analytical models predicting flows through them. The developed models are applied, with biology collaborators, to design, fabricate, and operate microfluidic environments to study neuronal interactions between different compartments of the human brain. As a whole, this work broadens the applications possible with microfluidics and provides an extended analytical basis to support wider adoption of the technology by providing accessible design and operational solutions to biologists.

Acknowledgments

No achievements are solely the result of individual contributions; they are invariably the outcome of collective efforts. Here, I would like to express my appreciation for all the people who have been by my side over the past four years, making this work possible.

I would first like to thank my supervisor, Prof. Edmond Walsh, for his wise guidance throughout my degree. His passion for engineering research has been of great inspiration to always improve myself. I have always admired people able to see beyond immediate results, and I couldn't have asked for a better teacher.

To Prof. Peter Cook, my adoptive supervisor, for hosting the lab in the great Dunn School. I appreciate his daily guidance and the private lessons he provided to enhance my writing skills. His dedication to science, persistent pursuit of excellence, and capacity to excel in diverse areas, regardless of his background, truly define him as the epitome of a scientist.

To Cristian, Cyril, Nick, and Joe for being amazing colleagues and for having made the lab naturally feel like a family. I am so grateful for every moment spent with such an amazing team. My whole life in Oxford would not have been the same without them.

To Charlotte, Herbert, Alonso, Barnaby, and Yao, my first flatmates in the glorious house on Walton Street. They managed to transform a pandemic into an enjoyable experience. I couldn't have found better people to start my new life in England.

To Herbert, Christina, Lizzie, and all members of Kellogg (Social) Tennis for all the happy memories on and off the courts. They made me enjoy Sunday mornings more than I would have ever thought.

To Henry who has been my flatmate for most of my Oxford time. I will always be grateful to him for having made the house a happier place and being such a loyal friend.

To Antonin, Silvia, Marin, and all my Oxford friends, for having made me feel like home. They brought joy to my life every single day (…and night). Memories of all the laughs, trips, dinners, ergs, and parties will last forever in my heart.

To all my home friends in Italy and abroad, who showed me an incessant support I could really feel even from far away. They are the pillars that hold me up, like bricks in a building that can't be moved without causing a collapse.

To Erika for having supported all my choices regardless of future implications and for having stood by my side during the most difficult moment of my life.

To Mathilde for her continuous encouragement during the whole final year of the DPhil and especially in the last few months before submission. It's hard to express just how grateful I am that we (re-)found each other.

To my family Daniele, Elena, Claudia, Cristina, Michele, Zia Silvia Nebu and Armando, Zia Silvia Facchi, Zia Biba and Nat, Giorgia, Filippo, and Marco who have always cheered me throughout my academic degrees. Nothing could have been achieved without them.

To my parents, Ornella and Cesare, who have always been my first supporters. Words cannot adequately convey my gratitude for them. They have consistently led by example, teaching me the invaluable lesson that perseverance and hard work inevitably yield rewards. This work is the result of all their sacrifices that allowed me to attend best schools and follow my dreams. Without them, this thesis would surely not exist, and I dedicate it to them.

Chapter 1: Introduction

Human organs are highly organised structures where multiple cellular populations are connected following a well-defined hierarchy. Current *in-vitro* studies have shortcomings trying to model such structures, as biological cultures usually consist of single populations of cells growing inside polystyrene Petri dishes where *in-vivo* conditions can hardly be recreated. These methods provide controllable environments that allows biologists to outline fundamental biological processes at the cellular level, but they are now of difficult applications to replicate organ-specific structural organization (Huh et al., 2013).

Disadvantages of traditional *in-vitro* models induced collaborations between biologists and engineers, who adapted microfabrication methods from the electronic industry (Whitesides, 2006) to generate innovative bio-engineered microenvironments where cells can grow. Microfluidics has introduced promising benefits in the biomedical sciences. These benefits include reagents and cost savings, alongside with novel methods to culture cells (Bhatia & Ingber, 2014). In particular, compared to traditional dishes, microfluidic environments have enabled to replicate biological conditions *in vitro* that more closely resemble the native ones *in vivo* (Battat et al., 2022).

Nevertheless, microfluidics has been struggling to replace conventional cell cultures which are still mostly used by biologists. Reason for this is that microfabricated environments have biocompatibility and operational concerns that prevent their usage to be widely employed (Sackmann et al., 2014). Namely, microfluidic devices are made of solid plastics (usually polydimethylsiloxane, PDMS) (E. Berthier et al., 2012) that completely bury cells behind inaccessible solid walls; requiring bio-scientists to change their well-established culturing protocols. Additionally, PDMS walls are normally tightly bonded over microscopy glass slides and cannot be easily removed nor reshaped, reducing the versatility of the technology.

To overcome many of these issues, a new microfluidic field, called ‘open microfluidics’, emerged (Zhang et al., 2021). In this new field, aqueous micro-circuits are fully or partially bounded by liquid interfaces (either with air or other immiscible fluids) acting as confining walls

held in place by interfacial tensions; therefore, samples become accessible (C. Li et al., 2020; Walsh et al., 2017; Yu et al., 2019). Recently, an innovative branch of open microfluidics, called ‘fluid-walled microfluidics’ (Deroy, Nebuloni, et al., 2021; Walsh et al., 2017), enabled creation of aqueous circuits sitting inside standard polystyrene Petri dishes under an overlay of an immiscible oil (typically a bio-inert fluorocarbon, FC40) to prevent evaporation. This technology enables users to create microfluidic environments in minutes using only cell-growth media and Petri dishes already used for decades by biologists. This characteristic is crucial as it enables fluid-walled microfluidics to be seamlessly integrated into well-established biological protocols. Compared to other technologies, it solely requires usage of tools and consumables that are already present in any biological laboratory. Additionally, the absence of solid plastic walls (other than the polystyrene floor) allows direct access to samples/cells at every location in the microenvironment by simply piercing a pipette tip through the fluid walls that re-seal once the pipette is removed. Uniquely, fluid walls can be destroyed and re-formed at any time and hence providing the potential to introduce spatiotemporal studies which is not possible with any other microfluidic approach. In conclusion, fluid-walled microfluidics exploits benefits of miniaturization of cell cultures while preserving almost unaltered the biosciences’ experimental workflows. Alongside all benefits, fluid nature of bounding walls introduces innovative challenges that are not present in standard PDMS devices; unlike solid ones, fluid walls morph in response to pressure changes complicating the modelling of fluid dynamics.

In the last few years, fluid-walled microfluidics showed the relevance of these characteristics in biological applications ranging from single-cell cloning (Soitu et al., 2018, 2019) to chemotactic studies on macrophages (Deroy, Rumianek, et al., 2022) and bacteria (Oliveira et al., 2022).

This thesis aims to advance the technology and focusses on modelling fluid walls during flow and developing a simple functional unit of a human organ, i.e., the brain. It begins by analysing the formation of stable concentration gradients of molecules diffusing across laminar streams, then it models an automatic pumping system that exploits the intrinsic pressure across fluid walls to drive the flow. Finally, it proposes a fluid-walled microenvironment that

mimics the fundamental unidirectional connectivity between cortex and striatum, opening this new technology to the ‘roaring’ field of Organs on Chip.

Objectives

The objectives of this thesis are:

1. Derive and validate a mathematical model to predict diffusion of solutes across laminar stream flowing in conduits bounded by fluid walls.
2. Derive and validate a mathematical model that predicts the passive flow in fluid-walled conduits driven by Laplace pressure between a source and sink in a transient manner.
3. Design a fluid-walled microenvironment amenable to mimic human brain connections in vitro.
4. Design and implement an assay to induce unidirectional growth of axons to model the cortex-striatum circuit of the brain.
5. Develop a method to sever axons growing in fluid-walled microenvironments to study axonal damage and healing.

This thesis comprises a total of 8 chapters initially introducing state-of-the-art of the field and fluid-walled microfluidics, then addressing the listed objectives, and finally discussing the work outlined and future developments.

Chapter 2 undertake a brief literature review. It starts by describing the origins of microfluidics outlining some of the main applications in the field of precision medicine. Finally, current limitations and emerging technologies are discussed from the perspective of the core topic of this thesis – microfluidics with fluid walls.

Chapter 3 introduces key concepts of fluid-walled microenvironments defining parameters and equations that will be used throughout this thesis. First, it presents geometry and properties of sessile drops and conduits. Then, it introduces equations that describe pressure shape of fluid walls during laminar flows through a straight conduit.

Chapter 4, submitted to Microsystem and Nanoengineering and currently under revision, presents a mathematical model to accurately predict flow and concentration gradients of solutes across parallel laminar streams flowing through a conduit with fluid walls. Such models are experimentally validated using a fluorescent tracer and found to provide excellent agreement with the developed analytical models. Main aim of this chapter is to provide an *'a priori'* method of predicting gradients through fluid-walled microenvironments that shall otherwise be measured case-by-case.

Chapter 5 is the publication in Journal of Fluid Mechanics. It proposes a method for passive pumping of liquids through fluid-walled circuits that exploits the intrinsic Laplace pressure across liquid interfaces (fluid walls) to drive the flow. The analysis is restricted to a simple circuit where a single drop (source) is connected to a large sink by a straight conduit. A novel equation describing volume variation of the source drop over time is presented and validated experimentally. The aim here is to provide a simple analytical solution that allows future users for quick estimation of perfusion, hence feeding, time in their cell culture and design their microenvironments accordingly.

Chapter 6, submitted to Lab on a Chip and currently under revision, presents a fluid-walled microfluidic design able to induce directional outgrowth of axons between different neuronal populations. Two chambers, hosting cell bodies and dendrites, are connected by a thin conduit where only axons can grow. Such design proved to recreate the cortico-striatal circuit of the brain, where the cortex unidirectionally contact the striatum. Moreover, it introduces an innovative method to damage axons growing in the conduit using a hydro-jet. Severed axons are then exposed to different chemical gradients to compare regrowth.

Chapter 7 discusses the thesis in its entirety linking the result chapters while highlighting main advantages and limitations.

Chapter 8 is the final in this thesis. It concludes on the objectives listed above and proposes future developments.

List of Publications

The work outlined in this thesis resulted in the following papers for which I am lead-author on 5 and co-author on 2.

Under revision

- **Nebuloni, F.**, Do, Q., Cook, P. R., Walsh, E. J., & Wade-Martins, R. (2023). A fluid-walled microfluidic platform for human neuron microcircuits and directed axotomy.
- **Nebuloni, F.**, Deroy, C., Cook, P. R., & Walsh, E. J. (2023). Stable diffusion gradients in microfluidic conduits bounded by fluid walls.

2023

- **Nebuloni, F.**, Cook, P. R., & Walsh, E. J. (2023). Flows in fluid-walled conduits driven by Laplace pressure. Journal of Fluid Mechanics, 969, A28.
- **Nebuloni, F.**, Morgan, J., Walsh, E. J., & Cook, P. R. (2023). A platform for modular assembly and feeding of micro-organoids on standard Petri dishes. Biology open, 12(5).

2022

- Deroy, C., Rumianek, A. N., Wheeler, J. H., **Nebuloni, F.**, Cook, P. R., Greaves, D. R., & Walsh, E. J. (2022). Assaying Macrophage Chemotaxis Using Fluid-Walled Microfluidics. Advanced Materials Technologies, 7(9), 2200279.

2021

- Deroy, C., Stovall-Kurtz, N., **Nebuloni, F.**, Soitu, C., Cook, P. R., & Walsh, E. J. (2021). Predicting flows through microfluidic circuits with fluid walls. Microsystems & Nanoengineering, 7(1), 93.
- **Nebuloni, F.**, Deroy, C., Cook, P. R., & Walsh, E. J. (2021). Microfluidics on standard Petri dishes for bioscientists. Small Methods, 5(11), 2100724.

Chapter 2: Literature review

Origins of microfluidics

The term “microfluidics” encompasses both the science and the technology that enable the control and manipulation of small volumes of fluids (10^{-6} to 10^{-12} litres) confined within sub millimetric environments. The first microfluidic observation was done by Felix Savart (1833), who noted that cylindrical microjets can always be divided in two segments: an “upper continuous” and a “lower troubled” section consisting of aligned separate droplets. (Figure 1A). Nearly half a century later, Lord John William Strutt of Rayleigh (1879) explained the theory behind this observation. He argued that a falling continuous capillary jet tends to separate into discrete droplets to minimize surface area as surface tensions dominates over inertial behaviours.

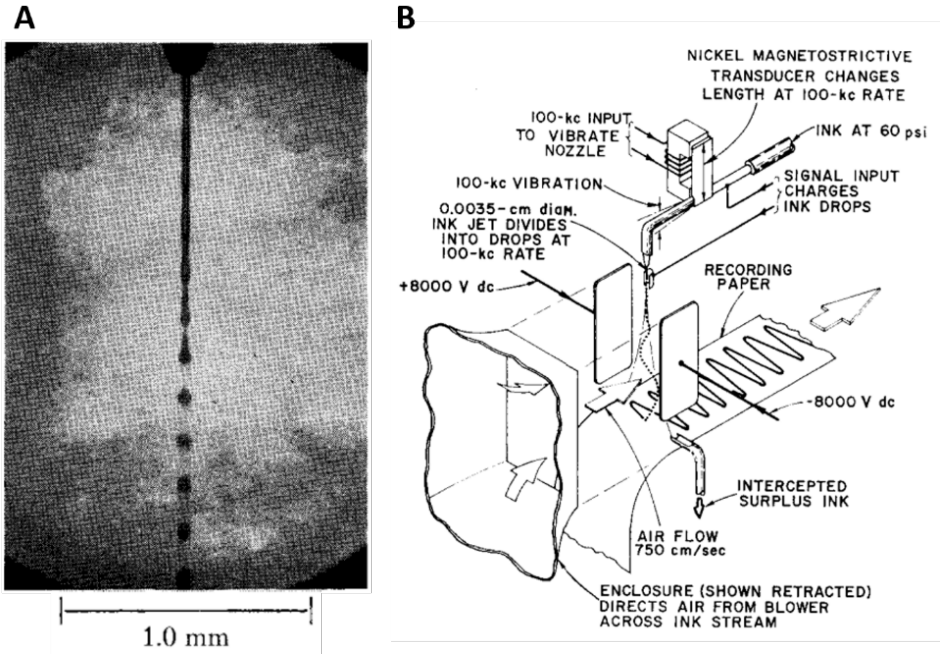

Figure 1. **Origin of microfluidics.**

(A) An *‘upper continuous’* cylindrical jet breaking up in a *‘lower troubled’* line of droplets.

(B) Schematic of Inkjet printing method proposed by Sweet in 1965. Sweet displaced drops falling through an electric field and controlled deflections to patterned droplet contact on substrates.

(Images from R.G.Sweet ‘High Frequency Recording with Electrostatically Deflected Ink Jets’ 1965).

Richard G. Sweet (1965) exploited such properties of microjets to prototype the first ink-jet printer (Figure 1B). He proposed a high speed oscillograph able to *"produce instantly visible, high frequency records with inexpensive writing materials"* (i.e. print on paper). Sweet's oscillograph was the ancestor of the first commercial inkjet printer designed by Ichiro Endo at Canon in 1977.

Inkjet printheads are considered as the first microfluidic devices, and they allowed the development of Micro Electro Mechanical Systems (MEMS) by the 1980's. Initially, MEMS were mainly employed as probes or pumps, and they were often fabricated with glass or silicon using microfabrication processes adapted from computer chip industry (Huh et al., 2013; Whitesides, 2006). Soon after, Rohr *et al*. (1991) thought of employing MEMS into the biomedical field. They demonstrated the ability to pattern the growth of ventricular myocytes of neonatal rats in strands of different sizes on top of simple glass coverslips previously modified with photolithographic techniques (Figure 2A). This work highlighted how cell culture environments could significantly influence cell behaviour in vitro, with different cellular organizations and impulses observed in strands of varying widths.

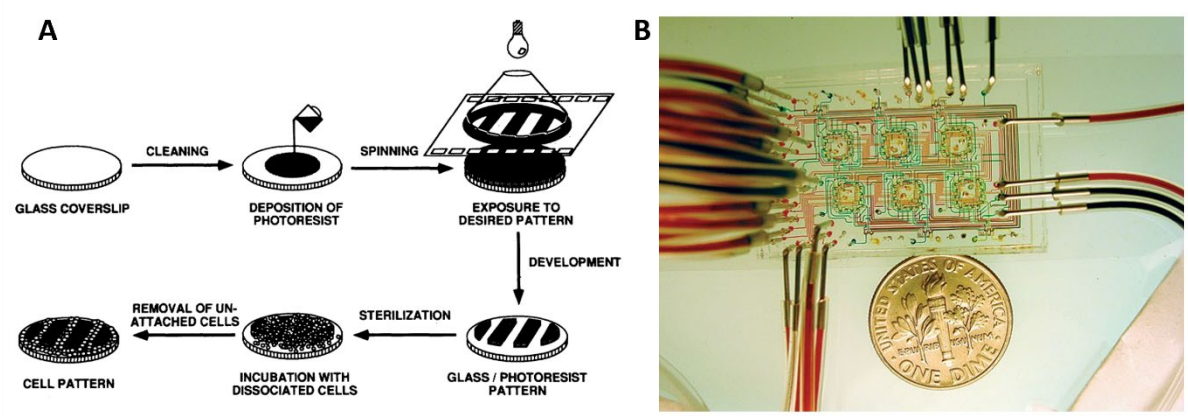

Figure 2. **First microfluidic devices.**

(A) Fabrication of a patterned cell culture on a glass coverslip proposed by Rohr *et al*. in 1991. Depending on the width of the channels, myocytes strands showed different cellular organization that led to differences in impulse propagation along bundles. (Image from Rohr et al. 'Patterned growth of neonatal rat heart cells in culture. Morphological and electrophysiological characterization" Circulation Research.' 1991).

(B) Top view of an integrated microfluidic chip made with PDMS (Image from G. Whitesides 'The origins and the future of microfluidics' 2006).

More recently, the replacement of glass and silicon, which posed fabrication challenges, with polydimethylsiloxane (PDMS) eased the creation of micro and nano features due to its thermosetting properties (Mata et al., 2005). This advancement accelerated the adoption of integrated devices where a wide range of biological/chemical operations can be performed simultaneously onto single devices as small as computer chips (Figure 2B) (Kim et al., 2012; Whitesides, 2006). At such a small scale, gravitational effects are negligible compared to interfacial forces, and flows are typically laminar, a regime where viscosity-related effects dominate over inertial ones, resulting in more predictable fluid behavior (E. Berthier & Beebe, 2014; Zhou & Papautsky, 2013). Additionally, microfluidic chips benefit from (i) reduced costs, (ii) increased sensitivity, (iii) smaller volumes, and (iv) high processing speed. In general, miniaturization implies short transport distances, enhancing the efficiency of mass and energy transfer. These characteristics, combined with PDMS's optical transparency and gas permeability, made microfluidics conceptually suitable for high-throughput engineered cell culture (Battat et al., 2022).

Engineered cell cultures and their relevance

Developing new drugs or drug delivery systems involves coordinated study of several variables. These include precise analysis of toxicity, cellular internalization, molecular binding, and many others. Despite the extremely strict approval processes and the decreasing number of new drugs annually approved, the occurrence of severe adverse drug events remains significant. Just in the United States it has been estimated that severe adverse events requiring emergency department visits occurred to 4 out of 1,000 patients in 2013-2014 (Shehab et al., 2016). This unveils big lacunae in the approval protocols that suffer understanding of important biological/molecular mechanisms and lack predicting off-target organ failures. To overcome some of these issues, the concept of precision medicine where medical treatments are tailored for each patient began to rise in the early 2000s (Friedman et al., 2015). However, since its conceptualization, precision medicine has encountered

numerous obstacles, among which, the lack of technological solutions is the most relevant to the topic of this thesis. Patient-specific treatments requires sensitive but inexpensive platforms where individual responses to different drugs can be tested. A recent review (Ayuso et al., 2022) claims traditional Petri dish-based assays overlook the complexity of native tissues and neglect functional assays defined as “tests that quantify the behaviour of cells to directly evaluate treatment response”. In this context, the same authors envision microfluidics as a versatile tool to generate innovative platforms where such assays can be performed. Therefore, the development of engineered *in-vitro* solutions enabling to fill existing gaps becomes crucial (Esch et al., 2015; Ferrari et al., 2023; Ferrari & Rasponi, 2021; Low et al., 2021; Mastrangeli et al., 2019).

In this scenario, Viravaidya *et al.* (2004) developed one of the first platforms to recreate simplified models of functional human organs where different cell types, each representing a different organ, were interconnected. Their platform consisted of four compartments (“lung”, “liver”, “other tissue”, and “fat”) and it was applied to probe the naphthalene systemic toxicity (Figure 3A). Since then, a wide range of organ-specific cultures have been developed, like heart (Marsano et al., 2016), liver (Carraro et al., 2008; Lee et al., 2007), gut (Kimura et al., 2008; Mahler et al., 2009), brain (Harris & Shuler, 2003), blood vessel (Song et al., 2004), lung (Huh et al., 2007), muscle (Lam et al., 2009), bone (Jang et al., 2008), and kidney (Jang & Suh, 2010). Some of these cultures have also been integrated with electro-mechanical actuators to provide physiological stimulations. Huh et al. (2010) proposed a Lung-on-Chip in which epithelial and endothelial cells are attached on both sides of a membrane that can be stretched to mimic respiratory dynamics (Figure 3B). Over the years, microfluidic platforms showed their capability to recapitulate simplified in-vivo functionality in vitro. The micrometric scale and consequent reduced operational costs make them a fit candidate to be employed for testing of patient-specific treatments. Such setups can range from simple models where patient-derived cells are cultured in 2D monolayers to highly complex and three-dimensional ones. Nevertheless, microfluidic devices still must face important challenges before being widely used in precision medicine. Main challenges revolve around their ability to be integrated

into biological/clinical workflows that are well established and remained almost unchanged for several decades.

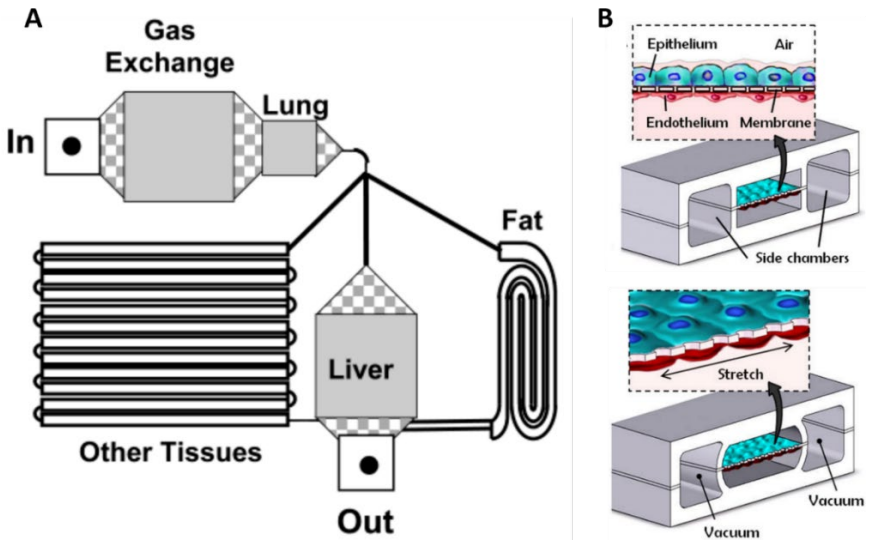

Figure 3. Organ-specific microfluidic platforms.

(A) Schematic of the platform proposed by Shuler et al in 2004. Naphthalene systemic toxicity has been studied after inhalation and after being processed by the liver. (Image from Viravaidya et al. 'Development of a microscale cell culture analog to probe naphthalene toxicity' 2004).

(B) Example of an engineered culture integrated with mechanical actuators. When the vacuum is created within side chambers the flexible PDMS thin walls are bent and the membrane between them is stretched. (Image from Huh et al. 'Reconstituting Organ-Level Lung Functions on a Chip' 2010).

Open Microfluidics

Although microfluidic cultures have demonstrated unprecedent advancements, adoption in biology and clinical research is negligible compared to initial expectations. Evidence of this can be found observing the number of microfluidic-related papers published every year in biology and medicine journals. Sackmann at al. (2014) conducted an analysis during the first decade of the 21st century and found that approximately 85% of microfluidic papers are published in engineering journals, with less than 10% appearing in biomedical-focussed publications. Several factors contribute to this challenge. One suggested reason for this issue relates to the incompatibility between the materials used in constructing microfluidic devices and cell cultures, as well as established biological protocols (E. Berthier et al., 2012). Engineers developed complex and efficient platforms in which micro channels are confined

between PDMS walls, and flow is driven by syringe pumps. Biologists, instead, work with fully open polystyrene dishes and move liquids with pipets. Another potential reason for the limited adoption in biomedicine is that microfluidics offers incremental enhancements to biological assays without having yet found a 'killer application' (Sackmann et al., 2014).

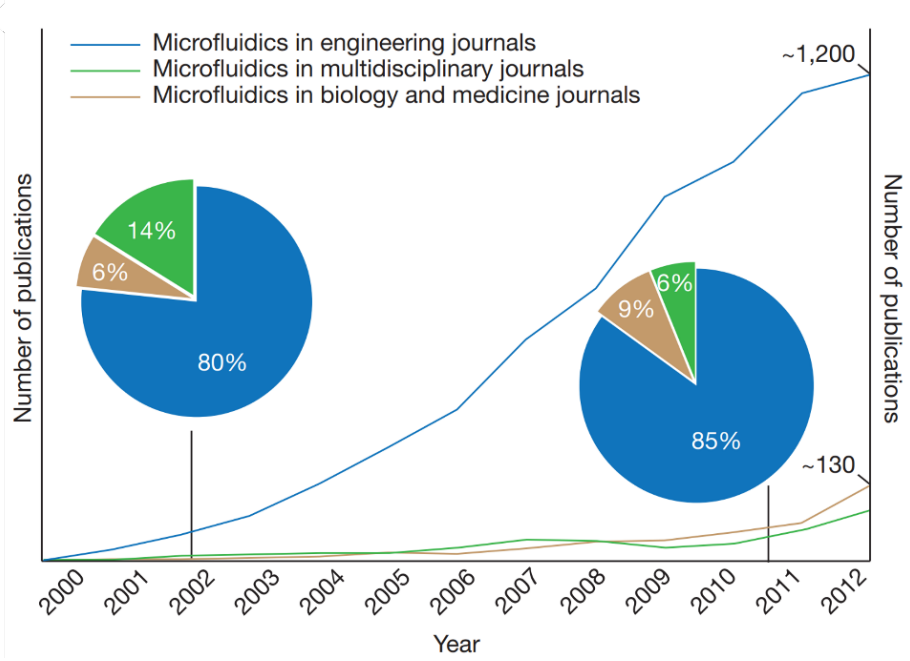

Figure 4. Microfluidic papers per year published in different fields' journals

Although the number of papers regarding microfluidics rocketed in the ten-year period in analysis, they remained confined just among engineers. (From Sackmann et al. 'The present and future role of microfluidics in biomedical research' 2014).

Open microfluidics overcomes some of these issues. It exploits fluid characteristics at reduced scales, and density or viscosity mismatches to generate multiphase fluid systems just partially bounded by solid walls (Casavant et al., 2013; Yu et al., 2019; Zhang et al., 2021). In particular, 'fluid-walled microfluidics', introduced by Walsh and his group (Deroy, Nebuloni, et al., 2021; Walsh et al., 2017) is raising significant interest because of its augmented biocompatibility (Soitu et al., 2018),versatility and ease of use (Soitu et al., 2019). Microfluidic devices can be fabricated within minutes using only cell-friendly materials such as Petri Dishes and tissue culture media (Soitu et al., 2020). Media is freely patterned into polystyrene dishes and overlaid with an immiscible and bioinert fluorocarbon (FC40) to prevent evaporation; then, the user has open access from above, and patterns can be easily reconfigured (Figure 5).

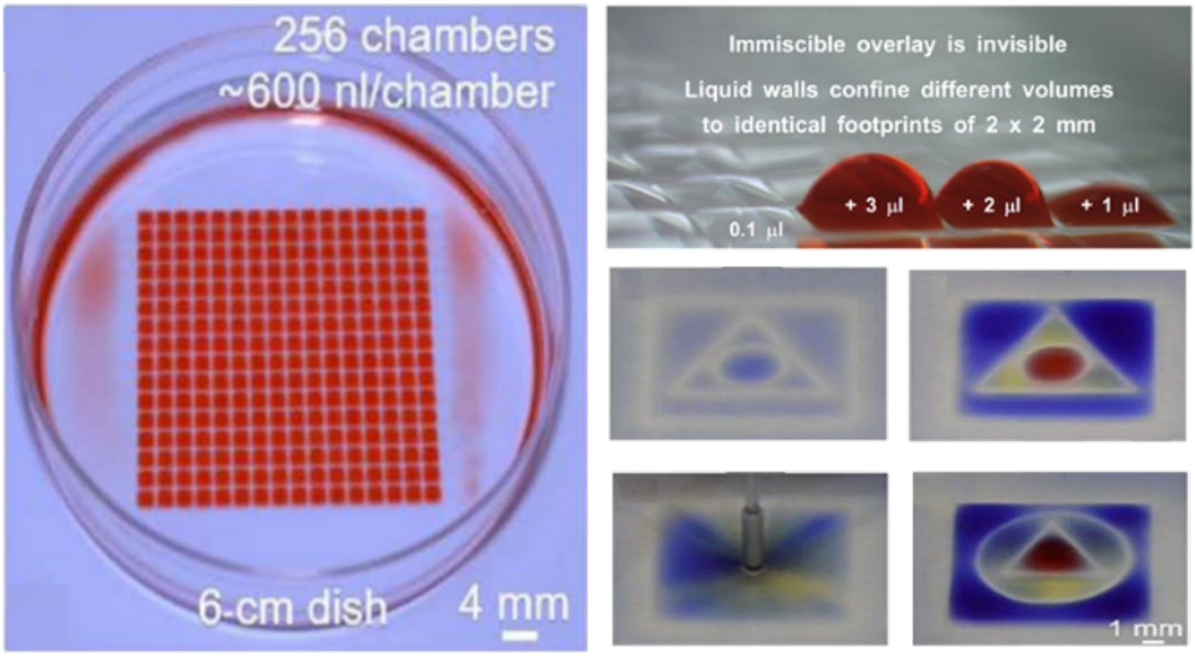

Figure 5. Fluid-walled microfluidics.

Microenvironments fabricated on polystyrene dishes; each chamber is separated from others by immiscible fluid walls. The absence of solid walls allows direct filling of chambers and easy reconfiguration. (Images from Soitu et al. 'Raising fluid walls around living cells' 2019).

Chapter 3: A primer on fluid-walled microfluidics

Microenvironments bounded by fluid walls have some boundaries that morph as a consequence of Laplace and hydrostatic pressure changes. The geometry of such interfaces impacts the behaviour of fluid-walled circuits, making it important from both fabrication and operational perspectives. This chapter introduces key parameters and equations which we use as foundation for the model derived in this thesis. It starts from the simplest fluid-walled environments, sessile drops, to end describing the shape of fluid walls of a conduit during steady flows.

Sessile drops

The shape of the drop sitting on a flat plane depends on the balance between gravitational and interfacial forces. When interfacial forces dominate, a sessile drop is a perfect cap of a sphere and its geometry is analytically defined, whereas presence of gravity (or buoyancy) distort its spherical shape and geometry can be only defined by complex numerical interpolations. The transition between the two conditions is described by the capillary length λ_c:

$$\lambda_c = \sqrt{\frac{\gamma}{\Delta\rho g}} \tag{1}$$

where γ is the interfacial tension, g the gravitational constant, and $\Delta\rho$ the density difference between the drop and the surrounding fluid. Capillary length defines the maximum size of a sessile drop to not be affected by gravitational forces. For drops mostly used in this work (cell-growth medium droplets under fluorocarbon FC40), the capillary length is of the order of 1.5 mm, but this value varies for different fluid pairs as in Chapter 5.

In this thesis, most of the sessile drops fall below λ_c of the system, hence their geometry is fully defined by any two of the following parameters: drop height (h), footprint radius (a), radius

of curvature of the interface (R), and the contact angle (θ). From Figure 6, one gets the relationship between these parameters:

$$R = \frac{a^2 + h^2}{2h}, \tag{2}$$

$$a = Rsin\theta, \tag{3}$$

$$h = R(1 - cos\theta), \tag{4}$$

$$h = \frac{a}{sin\theta}(1 - cos\theta)\,. \tag{5}$$

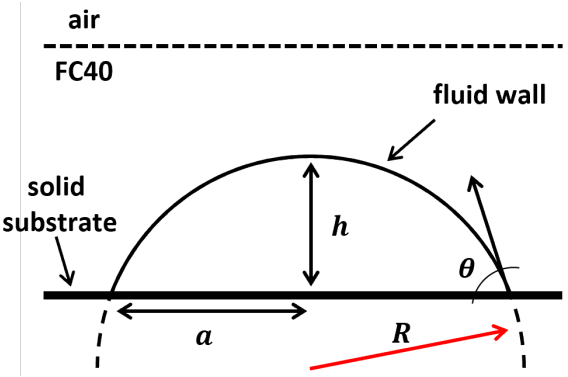

Figure 6: Cross section of a sessile drop under FC40.
Below the capillary length, sessile drops are shaped like perfect spherical caps and their geometry is fully defined by any three of the four parameters shown; a represents the footprint radius, R is the radius of curvature of fluid walls, θ is the contact angle, and h indicates the central height of the drop.

A drop of known volume on a flat surface has footprint radius and contact angle defined by the equilibrium of forces at the pinning line; line of contact between the three phases (solid-liquid-gas, Figure 6), and the volume in the drop is given by the equation:

$$V_{drop} = \frac{\pi h}{6}(3a^2 + h^2)\,. \tag{6}$$

Adding more volume, the drop varies its height and contact angle, such variation leaves the pinning line unchanged until the advancing contact angle (θ_A) is reached. After that, the footprint radius starts expanding. Similarly, removal of volume flattens the sessile drop over a fixed footprint up until the receding contact angle (θ_R) is breached; then, footprint shrinks. Sessile drops of cell growth medium in air have an advancing contact angle close to the equilibrium one (~50°), meaning very little volume can be added without the footprint

increasing in area. The FC40 overlay changes the equilibrium at the pinning line, shifting θ_A well above 90°, thus expanding the range of volumes that a drop can contain.

Finally, in absence of gravity, the pressure in the drop equals the Laplace pressure across the curved fluid interface, and it is defined by the Young-Laplace equation:

$$\Delta P = \gamma\left(\frac{1}{R_1}+\frac{1}{R_2}\right) \tag{7}$$

where R_1 and R_2 are the principal radii of curvature of the interface (J. Berthier et al., 2016). As sessile drops are symmetrical around the central height (h), radii of curvature are equal, and the equation simplifies to:

$$\Delta P = \frac{2\gamma}{R} = \frac{4\gamma h}{a^2+h^2}. \tag{8}$$

Conduits

If in nature sessile drops have circular footprints, fluid-walled technology allows to create footprints of any two-dimensional shape. Namely, a 'drop' sitting over a thin rectangular footprint (length is much greater than its width, Figure 7), can be considered as a fluid-walled conduit. Like drops, conduit cross sections are shaped like segments of a circle where a_c is the half width of the footprint, R_c is the radius of curvature of the fluid walls, and the height of fluid walls (h_c) across the width (z-axis) is defined as:

$$h_c(z) = \sqrt{R_c^2 - z^2} - \left(R_c - h_{c,max}\right), \tag{9}$$

where $h_{c,max} = h_c(z=0)$. Throughout this work, sections are conventionally in the zy-plane while flow is along the x-axis. In a conduit, the pressure generated by fluid walls is half compared to the pressure of a sessile drop with a circular footprint of diameter '$2a_c$'. Along the length of the conduit the radius of curvature of fluid walls can be considered infinitely large, therefore the Young-Laplace equation simplifies to:

$$\Delta P = \frac{\gamma}{R_c} = \frac{2\gamma h_{c,max}}{a_c^2 + h_{c,max}^2}. \tag{10}$$

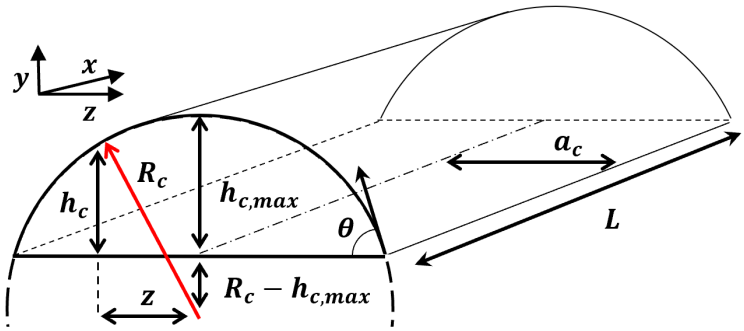

Figure 7: Three-dimensional schematic of a fluid-walled conduit.
When the length of the rectangular footprint is much greater than its width ($L \gg 2a_c$), curvature of fluid walls along x-axis becomes negligible and cross sections of the conduit are shaped like segments of a circle. During flows fluid walls morph in response to the pressure gradient.

Flows through fluid walls

Like a sessile drop morph above an unchanging footprint as volumes, hence pressures, change so does a conduit bounded by the same interface. During flows, a pressure gradient is applied along the length of the conduit, and so fluid walls morph in response to such gradient.

Our group derived a simple power law that describes the shape of conduit fluid walls during flow at steady state. Here, a summary of the derivation is reported; the full derivation can be found in the Supplementary Information of a paper titled 'Predicting flows through microfluidic circuits with fluid walls' (Deroy, Stovall-Kurtz, et al., 2021). Such law is inferred approximating flows as laminar, unidirectional, and fully developed reducing the Navier-Stokes equation along the x-axis to:

$$\frac{\partial P}{\partial x} = \mu \frac{\partial^2 u}{\partial y^2} \tag{11}$$

where P is pressure, μ the viscosity of the flowing fluid, and u is the velocity component along x-axis. Then, assuming the velocity profile as between infinite parallel plates, the solid

polystyrene floor and the morphing fluid ceiling located at $y = \pm\frac{h_{c,max}}{2}$ respectively, and assuming a perfect no-slip condition on both plates, one gets:

$$u(y) = \frac{1}{2\mu}\frac{\partial P}{\partial x}\left(y^2 - \frac{{h_{c,max}}^2}{4}\right). \tag{12}$$

If the no-slip condition is obvious on the solid floor, it is not on the interface between the cell-growth medium and the overlaying fluorocarbon. However, growth medium contains several proteins which are adsorbed to the interface, we believe these proteins form a thin monolayer which act as a 'solid' boundary. Although the cause is still unknown, the no-slip condition on fluid walls has been experimentally proven in a previous publication by our group (Deroy, Stovall-Kurtz, et al., 2021).

Volumetric flow rate is given by the integration of the velocity over the conduit cross section:

$$Q = \int_{-a}^{a}\int_{-\frac{h}{2}}^{\frac{h}{2}} u(y)dydz \tag{13}$$

Evaluating the integral along y-axis is trivial and leads to:

$$Q = \frac{2}{3}\frac{u_{max}}{h_{c,max}}\int_{-a_c}^{a_c} h_c^3(z)\,dz = \frac{2}{3}\frac{u_{max}}{h_{c,max}}\int_{-a_c}^{a_c}\left(\sqrt{R^2 - z^2} - \left(R - h_{c,max}\right)\right)^3\,dz \tag{14}$$

where $u_{max} = u(y=0) = -\frac{h_{c,max}^2}{8\mu}\frac{dP}{dx}$ represents the maximum of the velocity profile in the centre of the conduit. Evaluation of the integral along z-axis does not provide a simple solution that can be easily handled by users. Nevertheless, the integral can be normalized by substituting $\eta = \frac{z}{a_c}$ and dividing the integrand by $h_{c,max}^3$. If $h_{c,max} \ll a_c$, the nondimensional integral can be approximated to a constant value of ~0.92 with less than ~2.5 % error when the ratio $\frac{h_{c,max}}{a_c}$ varies from 5% to 50%. This approximation simplifies the above equation that can be rewritten in terms of the pressure gradient:

$$\frac{dP}{dx} = \frac{13.04\mu Q}{a_c h_{c,max}^3} \tag{15}$$

Given the millimetric scale of the cross sections, one can assume negligible the hydrostatic forces, therefore the pressure difference between two points along a conduit is given by Laplace pressure only. Furthermore, assuming $a_c \gg h_{c,max}$ at all times, the Eq. (x) can be simplified to $\Delta P = \frac{\gamma}{R_c} = \frac{2\gamma h_{c,max}}{a_c^2}$, and its derivative becomes $\frac{dP}{dx} = \frac{2\gamma}{a_c^2}\frac{dh}{dt}$.

Eq (x) then becomes:

$$\frac{dh}{dx} = \frac{6.52 Q \mu a_c}{\gamma h_{c,max}^3} \tag{16}$$

which can be simply solved by separation of variables resulting in the semi-analytical solution:

$$h_{c,max}(x) = \left(\frac{26.08 a_c \mu Q x}{\gamma} + h_{c,max(x=0)}^4\right)^{0.25} \tag{17}$$

Reintroducing $\Delta P = \frac{2\gamma h_{c,max}}{a_c^2}$ into Eq. (x) solves for pressure as:

$$P(x) = \left(\frac{417.28 \mu \gamma^3 Q x}{a_C^7} + \mathrm{P}_{(x=0)}^4\right)^{0.25} \tag{18}$$

Here, the position x = 0 corresponds at the end of the conduit, hence $h_{c,\max\,(x=0)}$ represents the central height of the outlet cross section, and $P_{(x=0)}$ the pressure of the same cross section. These constitute the governing equations of the field as the pressure drop (Eq.(x)) from inlet to outlet is not linear (as is the case for solid-walled conduits) and the height equation (Eq.(x)) provides all the information to quantify how fluid walls morph in response to pressure variations.

Interfacial tension

Fluid-walled microenvironments are held in place by interfacial tensions at the triple-contact point between the solid substrate, aqueous phase, and the liquid fluorocarbon overlay. Specifically, the tension across the interface between the two liquids directly influences the behaviour of fluid walls and, as such, represents a fundamental parameter in this thesis.

The interfacial tension is a force per unit length that arises from differences in energy between molecules at the interface and those within the bulk of the fluid. It describes the tendency of liquid interfaces to minimise their surface area and it only depends on the properties of the fluids in contact. Various methods can be employed to quantify this force. In this thesis, the pendant drop method is used to measure the interfacial tension, here a droplet of one liquid is suspended from a needle in a pool of the other liquid. It compares the shape of the pending droplet, deformed by gravity, with that of an undeformed sphere with the same volume. In cases of weak interfacial tension, gravity dominates, causing greater distortion in the pendant drop shape.

The Worthington number (Wo) plays a critical role to characterise precision of experimental measurements using the pendant drop method. It is defined as the dimensionless ratio between gravitation and capillary forces.

$$Wo = \frac{\Delta\rho \; g \; V_{drop}}{\gamma \; \pi D_{needle}} \tag{19}$$

Berry *et al*. (2015) showed experimental results are reliable when $0.3 \leq Wo < 1$, whereas measurements tend to underestimate the interfacial tension when $Wo < 0.3$. Therefore, all interfacial tensions reported in this thesis have been obtained with $Wo \geq 0.5$. Additionally, experimental data of interfacial tension between distilled water and FC40 were employed as a control to validate the experimental set-up. This particular fluid pair exhibits a well-documented interfacial tension of 52.06 $\pm$ 0.66 mN m^{-1} (Mazutis & Griffiths, 2012), that remains constant over time. Figure 8A,B depicts a 2.5 µl drop of FC40 in a pool of distilled water during a 30-minute recording. The drop's shape remains unchanged and so does the interfacial tension value (measured at 51.79 $\pm$ 0.74 mN m^{-1}), which closely aligns with values found in the literature (Figure 8C).

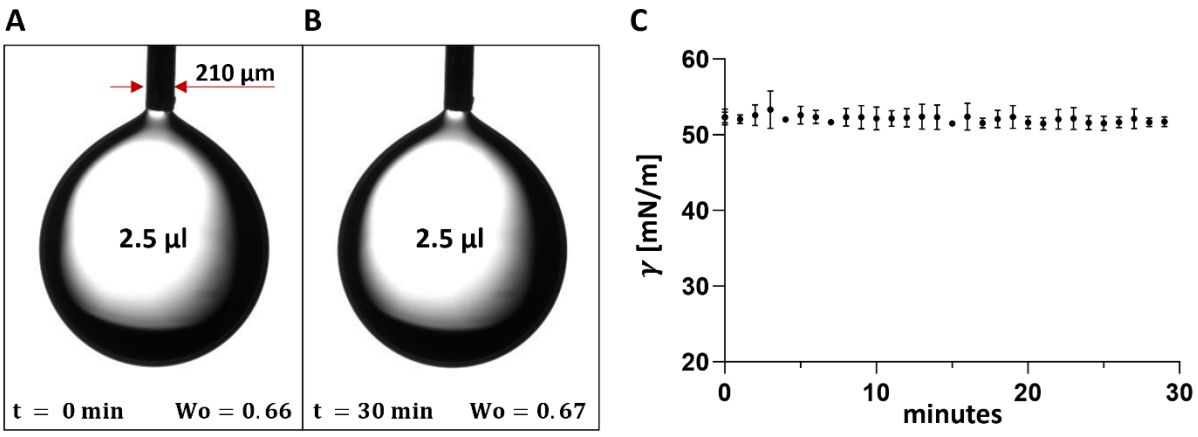

Figure 8: Interfacial tension (γ) between distilled water and FC40.

(A) Representative images of FC40 drops pending in a pool of distilled water at $t = 0$ min.

(B) Representative images of FC40 drops pending in a pool of distilled water at $t = 30$ min.

(C) Plot of interfacial tension measurements over time.

While interfacial tension is typically constant for 'clean' fluid pairs, this principle does not hold for fluids containing dispersed insoluble macromolecules. Interfacial tensions of such fluids lower over time as some of the suspended molecules are adsorbed onto the interface (Beverung et al., 1999; Ward & Regan, 1980). Once the interface becomes saturated, the system reaches equilibrium, and the interfacial tension stabilises. This phenomenon is relevant to fluid-walled microenvironments as cell-growth media are usually supplemented with animal sera that contain a wide range of large proteins involved in cellular metabolism. Figure 9A shows a 0.8 µl drop of FC40 pending in a pool of cell-growth medium (DMEM) + 10% fetal bovine serum (FBS) at $t = 0$. As serum proteins adsorb to the interface, the droplet shape is progressively deformed by gravity (Figure 9B) indicating a decrease of the interfacial tension. Once the interfacial surface becomes saturated, the tension stabilises to an equilibrium value of 22.8 $\pm$ 0.43 mN m^{-1} (Figure 9C). The same equilibrium interfacial tension is maintained at lower concentrations of FBS, indicating that this level is above the critical micelle concentration (CMC).

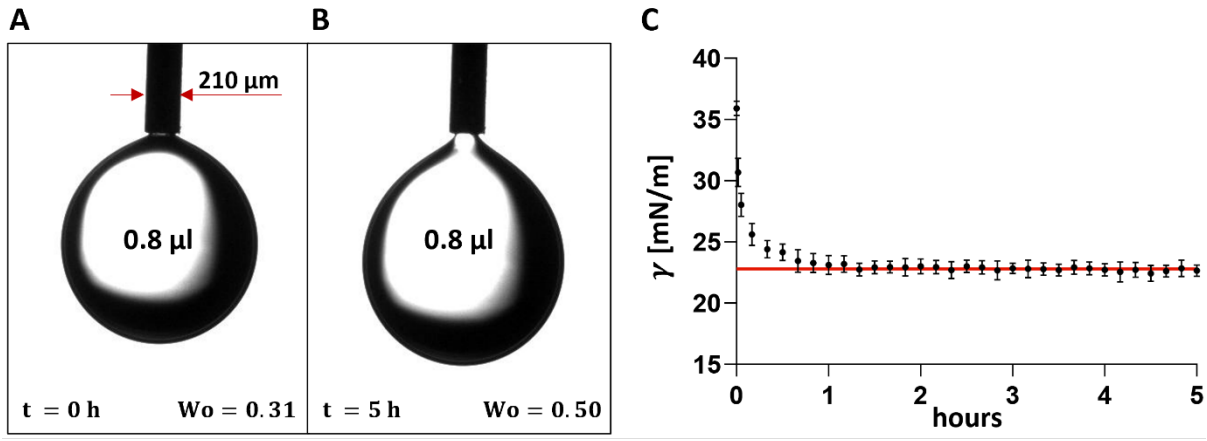

Figure 9. Interfacial tension (γ) between DMEM+10%FBS and FC40.

(A) Representative images of FC40 drops pending in a pool of DMEM+10%FBS at $t = 0$ h.

(B) Representative images of FC40 drops pending in a pool of DMEM+10%FBS at $t = 5$ h.

(C) Plot of interfacial tension measurements over time (red line represents the measured average between 3 h and 5 h).

Chapter 4: Stable diffusion gradients in microfluidic conduits bounded by fluid walls

Submitted to Microsystems & Nanoengineering on September 15th, 2023

Authors: Federico Nebuloni, Cyril Deroy, Peter R. Cook, and Edmond J. Walsh

Abstract

Molecular diffusion is functional to countless biological phenomena triggered by concentration gradients. Hence, mimicking of such gradients *in vitro* becomes critical in biomedical research. The reduced scale of microfluidic devices successfully enables precise control of diffusing molecules, opening to novel assays for sample purification and chemotaxis. However, such devices are usually fabricated using solid plastics that shield biological samples and prevent direct access. Therefore, open microfluidics proposes to simplify fabrication and usage of standard microfluidic devices by substituting solid boundaries with interfaces between immiscible fluids. Among open technologies, fluid-walled microfluidics raised particular interest as it allows to form accessible aqueous circuits inside standard Petri dishes. Here, all upper surfaces of such circuits are bounded by 'fluid walls' between cell-culture medium and a bio-inert immiscible fluorocarbon. However, these walls morph as pressures change; consequently, traditional equations describing flows through solid pipes no longer apply. We develop a mathematical model of the fluid dynamics as two or three aqueous streams with equal viscosity flow (non-turbulently) down a straight conduit with fluid walls, predict diffusion of molecules between such streams, and validate predictions experimentally.

Introduction

Diffusion represents fundamental mass transport, and many (perhaps all) cellular responses are triggered by concentration gradients of specific molecules. For example, during a bacterial infection, macrophages circulating in the blood stream exit vascular vessels to target the source of infection; such precise movement is driven by concentration gradients of secreted bacterial proteins [1] and host hormones [2]. Similarly, migration of platelets towards wounds is driven by diffusion of subendothelial molecules into lacerated vessels where they activate the coagulation cascade [3,4].

Despite the obvious importance of such phenomena, existing in vitro assays of cellular responses to molecular gradients have shortcomings. For example, chemotaxis is often studied using the transwell assay pioneered by Boyden [5,6]; however, diffusion gradients are unstable, the method is low throughput, and cells cannot be imaged as they respond in real time. Recently, the introduction of microfluidic approaches has overcome many of these limitations [7], but uptake of these methods still remains poor [8]. Reasons cited for this include fabrication complexity [9], and the inaccessibility of bio-samples contained behind solid plastic walls in devices that are often made of polydimethylsiloxane (PDMS). Consequently, more open-microfluidic technologies are being developed [10,11].

In fluid-walled microfluidics [12], the solid walls of conventional devices are replaced by liquid ones (i.e., interfaces between two immiscible phases). This counter-intuitive approach is possible due to specific properties of fluids at the micro scale where gravitational effects become negligible, and interfacial forces govern interface geometry. This approach has been used to fabricate and operate complex micro-circuits in simple cell-friendly ways [12–14]. For example, circuits are created in a standard Petri dish using a custom “fluid printer” that reshapes nanolitre volumes of cell-culture medium under an immiscible and bio-inert fluorocarbon (FC40) added to prevent evaporation (Fig. 1A). The printer consists of a 3D traverse equipped with a blunt needle (internal diameter ~70 μm) connected to a syringe pump. A submerged jet of FC40 is pushed through the nozzle to sweep away underlying

medium in the dish to leave FC40 "pinned" to the substrate (Fig. 1Aiii). The traverse moves the nozzle above the dish, without contacting media or dish, to reshape the aqueous phase into the desired pattern; such ‘jet-printing’ can make simple two-dimensional circuits in seconds [15–18] (Fig. 1Aiv).

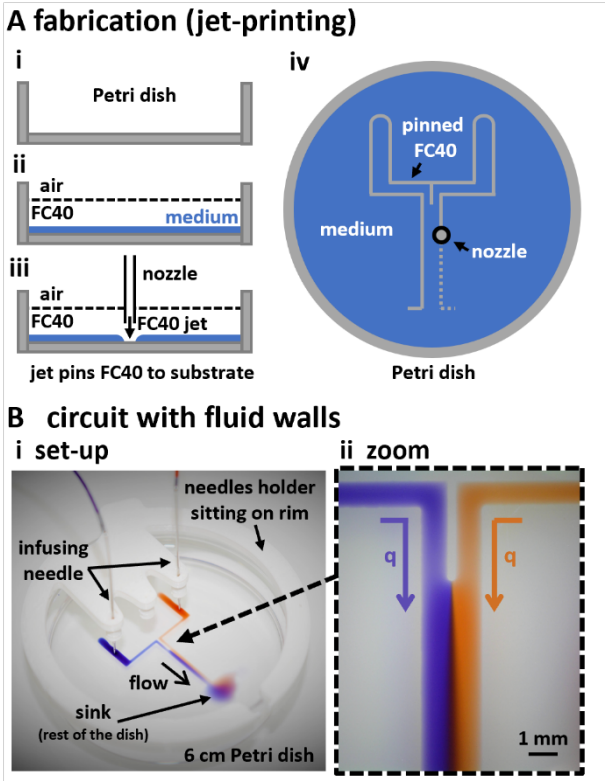

Figure 1. Making and operating a Y-shaped micro-circuit with fluid walls.

(A) Fabrication by jet-printing. (**i**) A virgin polystyrene Petri dish. (**ii**) Add a thin layer of medium and quickly overlay with FC40. (**iii**) More FC40 is jetted through the overlay to locally sweep medium away to leave FC40 pinned to the polystyrene substrate. (**iv**) A 3-axis traverse moves the jetting nozzle above the dish so it "prints" the Y-shaped footprint of the circuit without contacting polystyrene (dotted grey line: future path of jetting nozzle).

(B) Operation. (**i**) Experimental setup. The circuit sits in a 6 cm dish, with a 3D-printed needle holder clipped on to the rim. After lowering two needles through the holder and into each arm of the Y, red and blue dyes are infused into the circuit (using an external syringe pump that is not visible); red and blue dyes merge at the junction in the Y to flow as laminar streams down the central arm, through the open end, and out into the sink (the rest of the dish). (**ii**) Zoom of central arm illustrating diffusion of blue dye rightwards, and red dye leftwards, between laminar streams (this gives a widening purple zone towards the bottom). q: flow rate

To model molecular diffusion across parallel laminar streams, we designed a ‘Y’-shaped circuit consisting of two inlet branches that converge into a single conduit that empties into a

large sink (the rest of the dish). At the junction, inlet streams merge and flow side-by-side down the conduit as laminar streams, and the contents of these streams do not mix other than by diffusion across the inter-stream plane (Fig. 1Bii). From above, this circuit resembles similar ones made of PDMS [19–21] (Fig, 1Bi), but differs in one important respect – unlike solid plastic walls, these fluid walls morph according to pressure changes. This work develops, and experimentally validates, a semi-analytical model to predict diffusion gradients between laminar streams flowing through fluid-walled conduits of known width and length.

Recently, similar fluid-walled circuits have been employed in chemotactic studies of bacteria [15] and macrophages [17]; they have one big advantage over solid-walled circuits: they are bio-friendly in the sense that they fit seamlessly into existing biomedical workflows. For example, circuits are made of standard cell-growth media and Petri dishes [22], the fluid walls are easily pierced by pipets and automatically re-heal when pipets are withdrawn (so cells can be recovered from any part of a circuit), fluid walls can be destroyed and rebuilt during experiments [16]. Additionally, as gravitational forces are negligible due to the sub-millimetric scale of the circuits ($Bo \ll 1$), dishes can be moved around the working lab (i.e., in/out of incubators, in/out of biological hoods, or on/off the microscope stage for imaging) without altering the geometry of the circuit nor affecting its integrity. Therefore, a model facilitating prediction of concentration gradients of molecules flowing through conduits bounded by fluid walls becomes necessary.

Theory

Morphing fluid walls

In the Y-shaped circuit, streams of two aqueous and miscible liquids converge at the junction to flow down the single straight conduit (width – 2 mm, length – 12 mm, height < 100 μm; Fig. 2Ai). Conduit sections sit in the zy-plane, while flow is along the x-axis. Our circuit sits in a standard polystyrene Petri dish and is capped by the interface formed with the overlaying fluorocarbon. Due to the fluid nature of the upper boundary, circuit cross-sections are shaped

like segments of a circle (Fig. 2Aii). During flow, circuit footprint remains unchanged, but fluid walls/ceilings inevitably morph as pressures change. After fabrication, fluid walls and ceilings are initially flat above the circuit footprint, but when flow begins, they 'inflate' to accommodate the increasing pressure. During steady flow, fluid walls stop morphing but their height varies in the streamwise direction to reflect the local pressure in the conduit [18]. Consequently, the maximum height of conduit cross-section (h_0) decreases along the x-direction, being minimal at the outlet (Fig. 2Aii). At different flow rates, h_0 at any point down the conduit also differs (Fig. 2Aiii).

Fluid dynamics at the microscale is typically characterised by low Reynolds numbers and laminar flows. This regime yields important simplifications and increased predictability of flows, allowing analytical solutions of the Navier-Stokes equations under well-defined boundary conditions. Recently, Deroy et al. [18] derived a simple power law that describes the variation of h_0 down straight conduits of known geometry at constant flow rates (see Supplementary Information, and Supplementary Fig. 1) showing that flows at steady state can be modelled like those between infinite parallel plates. Then, using notations illustrated in Figure 2Aiii, one can derive equations of the flow velocity profile and of any cross-section profiles along the conduit:

$$\begin{cases} h(z) = \sqrt{\left(\dfrac{(a^2 + h_0^2)}{2h_0}\right)^2 - z^2} - \dfrac{a^2 - h_0^2}{2h_0} & (1) \\ u(y,z) = \dfrac{1}{2\mu}\dfrac{dP}{dx}\left(y^2 - \dfrac{h(z)^2}{4}\right) & (2) \\ u_{max}(z) = \dfrac{Q}{0.61 h_{(z)} a} & (3) \end{cases}$$

where a represents conduit half width, h_0 is the central height of the cross section that varies along the x-axis as pressure decreases, $\frac{dP}{dx}$ and u are the pressure gradient and local velocity of the fluid in the streamwise direction respectively, and u_{max} is the maximum velocity in a cross section. u_{max} varies as h changes along the z- and x-axes; it has a local maximum in each cross section at $z = 0$: $u_{\max\,(0,x)} = \frac{Q}{0.61 h_0 a}$.

Parallel laminar streams

When flow is laminar, the two input streams run side-by-side down the central conduit and mass transport between streams is by diffusion only. If the two inputs have identical viscosities, stream widths depend solely on the difference between flow ratio of the input streams [23,24] (Fig. 2B). Hence, the volumetric flow rate of each stream is given by the integral of velocity, u(y,z), over the portion of the cross section wetted by that fluid, and the ratio is:

$$\frac{q_A}{q_B} = \frac{\int_s^a \int_{-\frac{h}{2}}^{\frac{h}{2}} \frac{1}{2\mu}\frac{\partial P}{\partial x}\left(y^2 - \frac{h(z)^2}{4}\right) dydz}{\int_{-a}^s \int_{-\frac{h}{2}}^{\frac{h}{2}} \frac{1}{2\mu}\frac{\partial P}{\partial x}\left(y^2 - \frac{h(z)^2}{4}\right) dydz} \tag{4}$$

$$\therefore \frac{q_A}{q_B} = \frac{\int_s^a h(z)^3 dz}{\int_{-a}^s h(z)^3 dz}$$

where $\pm a$ are the edges of the channel footprint, and q_A plus q_B are input flow rates, respectively (with total flow rate $Q = q_A + q_B$). Every cross section (normalized over half width) can be theoretically divided in two regions by a vertical line in position 's' ($-1 < s < 1$) across its width representing the contact plane between streams (Fig. 2Bii). However, given the variation of aqueous height across the conduit, there is no simple analytical equation predicting s – unlike the case for rectangular channels in laminar flow [23]. Therefore, a predictive numerical solution for 's' is required; as expected, the trend is non-linear (Fig. 2Biii).

Diffusion gradients across parallel streams

Laminar flow and steady-state conditions significantly simplify modelling of mass transport between parallel streams, as diffusion is the only driving factor. The advection-diffusion equation at steady state for a solute (of concentration $\boldsymbol{c}$ and diffusion coefficient D) dissolved in an incompressible and isotropic fluid flowing with velocity $\mathbf{v}$ is:

$$D\nabla^2 \boldsymbol{c} - \mathbf{v} \cdot \nabla \boldsymbol{c} = 0 \tag{5}$$

Considering fully-developed laminar flow, and unidirectional along x, Eq. (5) simplifies to Fick's law as:

$$\frac{\partial c}{\partial x} = \frac{D}{u}\frac{\partial^2 c}{\partial z^2} \tag{6}$$

where u is the velocity along the x-axis. Assuming diffusion between infinitely-large reservoirs, the solution to Eq. (6) is:

$$c(z,x) = \frac{C_0}{2} erfc\left(\frac{z}{2\sqrt{\frac{D}{\overline{u}}x}}\right) \tag{7}$$

We will use η as the bracketed term. Diffusing molecules initially occupy a finite region, and the initial state is defined as $c = C_0$ if $z \leq 0$, and $c = 0$ if $x > 0$. In Eq. (7), C_0 is the concentration of the solute in one of the inlet branches, and $\overline{u}$ represents the mean velocity of the parabolic profile (defined as $\overline{u} = \frac{2}{3}u_{\max}$). It is understandable from Eq. (3) and Eq. (7) that concentration gradients do not simply depend on the position (z, x) but are affected by velocity changes along both x- and z-axes.

Finally, we define the flow time of molecules along the conduit $\left(t = \frac{L}{\overline{u}_{av}}\right)$, where L is the length of the conduit and $\overline{u}_{av}$ the average of all mean velocities down the conduit of the contact plane between streams, and the diffusion time across the conduit $\left(t_d = \frac{a^2}{D}\right)$. The ratio of flow time over diffusion time defines the Fourier number (Fo):

$$Fo = \frac{t}{t_d} = \frac{DL}{a^2 \overline{u}_{av}} \tag{8}$$

It represents a dimensionless contact time between streams flowing in the conduit; in other words, it defines the time molecules have to diffuse before reaching the outlet. We design our

circuit so that $Fo \ll 1$ for all flow rates tested. This condition allows observation of diffusion in the proximity of the contact plane between streams without altering inlet concentrations near conduit boundaries. In other words, as our model assumes that diffusion happens between infinite reservoirs, it is valid as long as $Fo \ll 1$. Nevertheless, Eq. (8) represents the definition of Fo when input rates are equal, the contact plane sits in the middle ($s = 0$), and the two streams occupy equal portions of the conduit. In cases where $s \neq 0$, we can define two Fourier numbers depending on which portion of the conduit is analysed. Thus, $Fo = \frac{DL}{[a(s+1)]^2 \bar{u}_m}$ if $q_A < q_B$, and $Fo = \frac{DL}{[a(1-s)]^2 \bar{u}_m}$ if $q_A > q_B$ describing if any of the two flowing solutions alters inlet concentration near the opposite boundary.

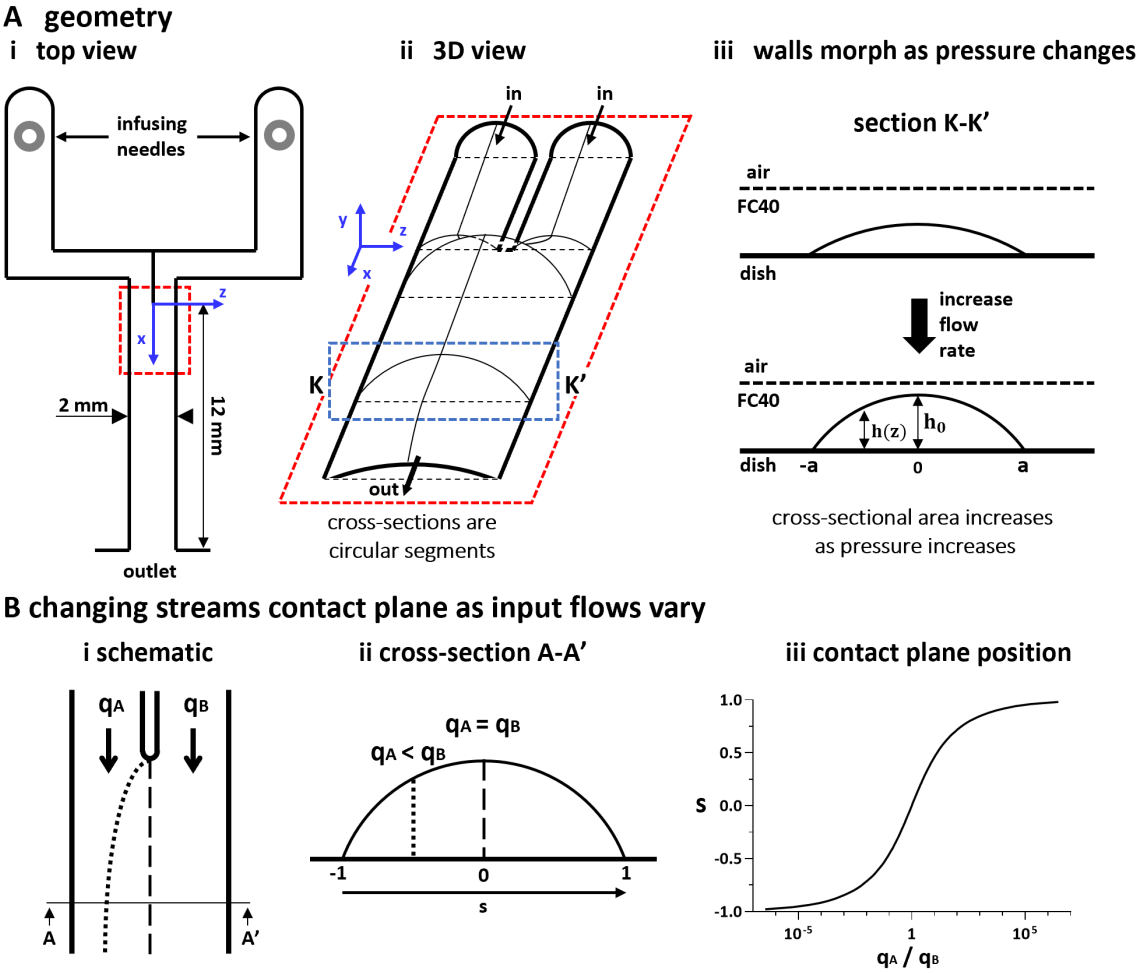

Figure 2. As flows change, conduit cross-sections change above unchanging footprints. **(A)** (**i**) Footprint of Y-shaped circuit. (**ii**) 3D schematic of area within the dashed red line in (i); not to scale. As the circuit is bounded by fluid ceilings, cross sections of all aqueous arms are shaped like circular segments. (**iii**) Fluid walls morph as flows change to reflect pressure variations in an arm over

an unchanging footprint, illustrated here at position K-K' – the area within the dashed blue line in (**ii**). The central height h_0 and cross-sectional area increase as the flow rate rises.
(B) Changes in position of the contact line between laminar streams as input flow rates vary. (**i**) Top view of footprint at junction (q_A and $q_B$are flow rates of the two inputs). Dashed and dotted lines: inter-stream contact planes when $q_A = q_B$ (dashed), and $q_A < q_B$ (dotted). (**ii**) Cross-sectional view at position A-A' in (**i**) showing two different locations 's' of the contact plane at different input flow rates. (**iii**) Position 's' of the contact plane across the width of the conduit for a range of inlet flow-rate ratios (log scale).

Materials and Methods

Reagents

Cell culture medium used in this work is always DMEM (Dulbecco's Modified Eagle Medium, Sigma-Aldrich) supplemented with 10% fetal bovine serum (FBS, Gibco). The overlaying fluorocarbon (FC40) is purchased from 3M Fluorinert™ and subsequently treated (protocol property of iotaSciences Ltd) to obtain FC40STAR. The fluorescein solution used to calibrate measurements and observe diffusion gradients is prepared by dissolving fluorescein-dextran 9 kDa (FD-10S, Sigma-Aldrich) 300 μM in sterile PBS (phosphate-buffered saline, Gibco). Throughout this article, every time we mention medium/media, FC40, or fluorescein, we are referring to DMEM+10%FBS, FC40star, and fluorescein-dextran 9kDa in PBS respectively.

Microscopy and imaging

All experiments have been performed on an inverted microscope (Olympus IX53) equipped with a 4x objective connected to a single-lens reflex camera (Nikon D7100 DSLR). Fluorescein molecules were excited by a LED light (CooLED λ = 470 nm, light intensity 15%) and fluorescent images were recorded with shutter exposure of 0.25 s. All fluorescent images have been recorded focusing on the FC40 walls pinned to the dish using phase contrast, then switching to fluorescence without adjusting focus position. The image in Figure 1Bi was taken using a Nikon D5100 DSLR camera, and the one in Figure 1Bii with Dino Capture 2.0 camera.

Circuit fabrication

All circuits presented in this paper are jet-printed using standard clean polystyrene Tissue Culture Treated 60 mm Petri Dishes (Corning Inc, Life Sciences). First, the dish is filled with 1 ml cell culture medium to wet its surface, as much volume as possible is then carefully removed by pipet in order to leave just a thin layer wetting the surface. This layer is then quickly overlaid with FC40 to prevent evaporation. The dish is placed on a custom designed fluid-shaping printer (iotaSciences). Then, the tip of a blunt needle (70 μm inner diameter; iotaSciences) held by the 3D traverse unit of the printer is lowered into the FC40 overlay until ~ 0.3 mm above the bottom of the dish, and additional FC40 jetted out of the needle at 480 μl/min (the needle is connected via a Teflon tube to a 1 ml glass syringe (Hamilton) driven by a syringe pump integrated in the printer). The jet sweeps the medium layer off the substrate as the traverse moves the needle above the dish. The conduit is designed with a width of 2 mm, however as the fluid walls that bound the conduit have thickness ~150 um, the actual conduit width is ~1.85 mm. Circuit patterns and printer control commands are written using G-code.

Infusion pumps and tubing

All experiments are performed with syringe pumps (PhD ULTRA, Harvard Apparatus) equipped with two 100 μl glass syringes (Hamilton) connected to 25G stainless steel blunt infusing needles (Hamilton) through 28G Teflon tubes (Adtech). Needles are held vertically in position over inlet arms by home-made 3D-printed holders that clip on the rims of dishes (similarly to Deroy et. Al [16]).

Determining h(z) from fluorescence intensity

Fluorescence intensities in arbitrary units (a.u.) given by fluorescein seen in images are converted to local conduit height using linear calibration curves constructed as follows. A 2-inlet conduit is infused using the same fluorescein solution in both inlets at three different total

flow rates (where $q_A = q_B$), and nine images are recorded at every millimetre down the conduit between 2-10 mm from the junction. All images are then analysed using ImageJ (RRID:SCR_003070) to plot intensity profiles at each location across the conduit, and corresponding theoretical cross-section profiles are computed using Eq. (1) and divided by the pixel intensity in the same location 'z' to determine the height-to-intensity ratios. The three flow rates tested are 5, 10, and 20 µl/h (values refer to total flow rate Q).

Determining diffusion gradients of fluorescein across conduits

In these experiments, PBS + fluorescein is infused into the left-hand arm, and PBS into the right-hand one. Intensity profiles of flowing fluorescein are then measured across conduit width at every millimetre down the length of the conduit between 2-10 mm from the junction. Pixel intensity [a.u.] is converted into height [µm] using a linear calibration curve, and subsequently divided by theoretical height of the conduit cross section (Eq. (1)) at the same location along x-axis.

Results

Mass transport by diffusion of fluorescein between parallel streams flowing through a straight fluid-walled conduit is observed by microscopy. The fluorescein solution is infused into one inlet branch (conventionally the left one), and PBS into the other one. After the junction, fluorescent molecules diffuse rightward between laminar streams to yield increasing concentrations on the right as distance from the junction increases. A fluorescence image of the conduit is collected, and intensity profiles of green fluorescence are then measured across conduit width at every millimetre down its length between 2-10 mm from the junction. Then, the intensity profile is converted into an equivalent height profile, and local concentration computed as the height ratio between the equivalent profile traced by fluorescein and the theoretical profile of the cross-section described by Eq. (1). In other words, if the height of the

fluorescent equivalent profile at a specific location equals the theoretical one, no diffusion happened so the concentration there equals the infused concentration C_0.

Deriving a calibration curve

Pixel intensity (a.u.) at a specified point in the resulting image must now be converted into a concentration, and this is usually achieved using a direct calibration done, for example, by measuring intensities of a dilution series of the fluorescein [25]. However, as bounding fluid walls/ceiling are not flat and morph as flow rates change, this induces the same concentration C_0 to correspond to multiple intensities depending on z-location and flow velocity. This prompted us to develop a calibration method that yields a linear curve applicable to all conditions used.

To develop the calibration method, the same fluorescein solutions are infused into both inlets so there is no gradient between streams (Fig. 3Ai), and images of the conduit are collected with the focus on the base of the fluid walls pinned to the dish. These pinned walls are visible in phase-contrast images (Fig. 3Aii), but not in fluorescence ones (Fig. 3Aiii) where they are shown as dashed white lines here and in subsequent images. Two trends are visible in fluorescence images: intensity increases between 0 and 2 mm from the junction ($x = 0$ at the junction), before progressively declining towards the exit. The increase is due to the sudden change of width and flow rate that happens at the junction. Fluid walls/ceiling height lift to accommodate such changes (~ 4-fold increment), hence a brighter intensity is visible. Such height variation is not immediate but occurs over the first couple of millimetres after the junction, however complexity of the curvature of the fluid walls/ceiling in this section does not allow for analytical predictions (Supplementary Fig. 1). As Eq. (1) does not apply within 1-2 mm of the junction(Deroy, Stovall-Kurtz, et al., 2021), we sample intensities every millimetre from 2-10 mm (Fig. 3B shows intensity profiles at 2 and 10 mm from the junction for three different flow rates). As conduit heights vary to balance pressure, intensity profiles decrease towards the outlet but increase as flow rate increases. Next, intensities are sampled every 0.1

increments across the normalised width of the cross section (for all 3 flow rates) and plotted against conduit heights calculated from Eq. (1). They fall on a straight line with slope 0.79 ± 0.03. This line is derived from the use of intensities in all pixels measured ($n = 45{,}495$) across the 9 cross sections and for the 3 flow rates (Fig. 3C). In other words, there is a linear relationship between height [µm] and pixel intensity [a.u.] – where $equivalent\ height = 0.79 \times intensity$ – over a wide range of conditions. Theory fits well with experimental points inside the depth of field of the objective (~80 µm, $\pm 40\ \mu m$ around focal plane; manufacturer's data), and as expected it begins to diverge outside this range. Therefore, this linear approximation enables prediction of all heights across the width of the conduit at different distances from the junction (Fig. 3D), although errors progressively increase when height exceeds the depth of field (Fig. 3D, compare red circles with upper black line) and this becomes a limiting factor of the method.

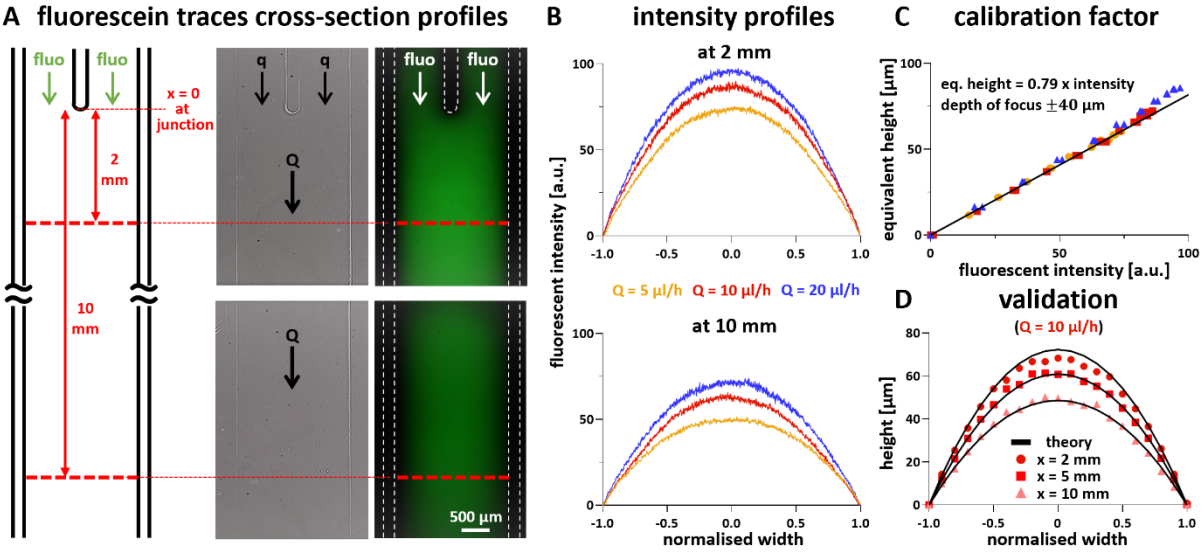

Figure 3. Calibration – a linear relationship between calculated height and fluorescent intensity.
(A) Setup (Y-shaped circuit). After infusing fluorescein (fluo) into both input arms ($q_A = q_B$), images are collected along the conduit below the junction, and fluorescence intensities analysed across conduit widths every millimetre from 2 mm to 10 mm from the junction. Phase-contrast images with pinned FC40 walls visible. Fluorescence images show intensity decreases as pressures fall towards the outlet.
(B) Fluorescence intensity (a.u.) profiles of conduit cross-sections at 2 and 10 mm from the junction for three different flow rates.
(C) Linear relationship between fluorescence intensity and height. Data points are obtained by sampling intensity plots like those in (B) every 0.1increments along the normalised width for all flow rates at the

2 mm cross-section, with colours reflecting flow rates in (B). The maximum error between experimental data shown in the graph and the calibration line ~7% for $\mathrm{Q} = 5\ \mu\mathrm{l/h}$ (yellow data points, $\mathrm{n} = 19$) or $\mathrm{Q} = 10\ \mu\mathrm{l/h}$ (red date points, $\mathrm{n} = 19$), while it increases up to ~12% when $\mathrm{Q} = 20\ \mu\mathrm{l/h}$ (blue data points, $\mathrm{n} = 19$). Expanding the error analysis to the whole data set ($\mathrm{n} = 45{,}495$), the average error made to convert pixel intensity to equivalent heights using the calibration equation presented is ~4%.

(D) Plot of heights derived from intensities as in (C) against normalised width at 2, 5, and 10 mm from the junction. ($Q = 10\ \mu l/h$). Black curves: heights calculated from Eq. (1). Experimental data shown in the graph diverge from theoretical prediction by 2.66% on average ($\mathrm{n} = 63$) with a maximum error of 7.08% for the $\mathrm{x} = 2\ \mathrm{mm}$ cross section.

Diffusion gradients across parallel streams

We now return to the original setup where fluorescein in PBS, and just PBS, are infused into the left- and right-hand input arms to flow as laminar streams down the central arm (Fig. 4Ai). Soon after the junction, fluorescein diffuses across the contact plane between the two laminar streams (Fig. 4Aii). We quantify diffusion by recording pixel intensity across the conduit at x = 2-10 mm as before, and convert intensities to equivalent heights using the calibration factor (Fig. 3C). The equivalent height profile across the conduit can be paired with a related one derived from Eq. (1). Such pairs are now overlaid by normalizing widths and heights with respect to $s = 0$ and h_0 (Fig. 4Aiii). Equivalent-height profiles perfectly follow the theoretical ones on the left of the conduit, and – in the absence of diffusion – they should fall immediately to zero (at normalised width 0) in accordance with Eq.(7); instead, they decline gradually. Each of the resulting profiles is equivalent to the corresponding concentration profile, as the ratio of equivalent to theoretical heights (red to black in Fig. 4Aiii) at each point across the conduit reflects the local fluorescein concentration. Thus, where the equivalent height equals the theoretical one, the fluorescein is undiluted (100% C_0); where the ratio is zero, there is no fluorescein (0% C_0). When concentrations derived from intensities in this way are compared to the predictive model (Eq. (7)), there is excellent agreement across conduits at all three flow rates (Fig. 4Bi, Supplementary Fig. 2). All results obtained from theory and experiment are now collapsed into one chart (Fig. 4Bii); the excellent convergence between the two validates the theory for predicting diffusion profiles as velocities vary down a conduit (Fig. 4Biii).

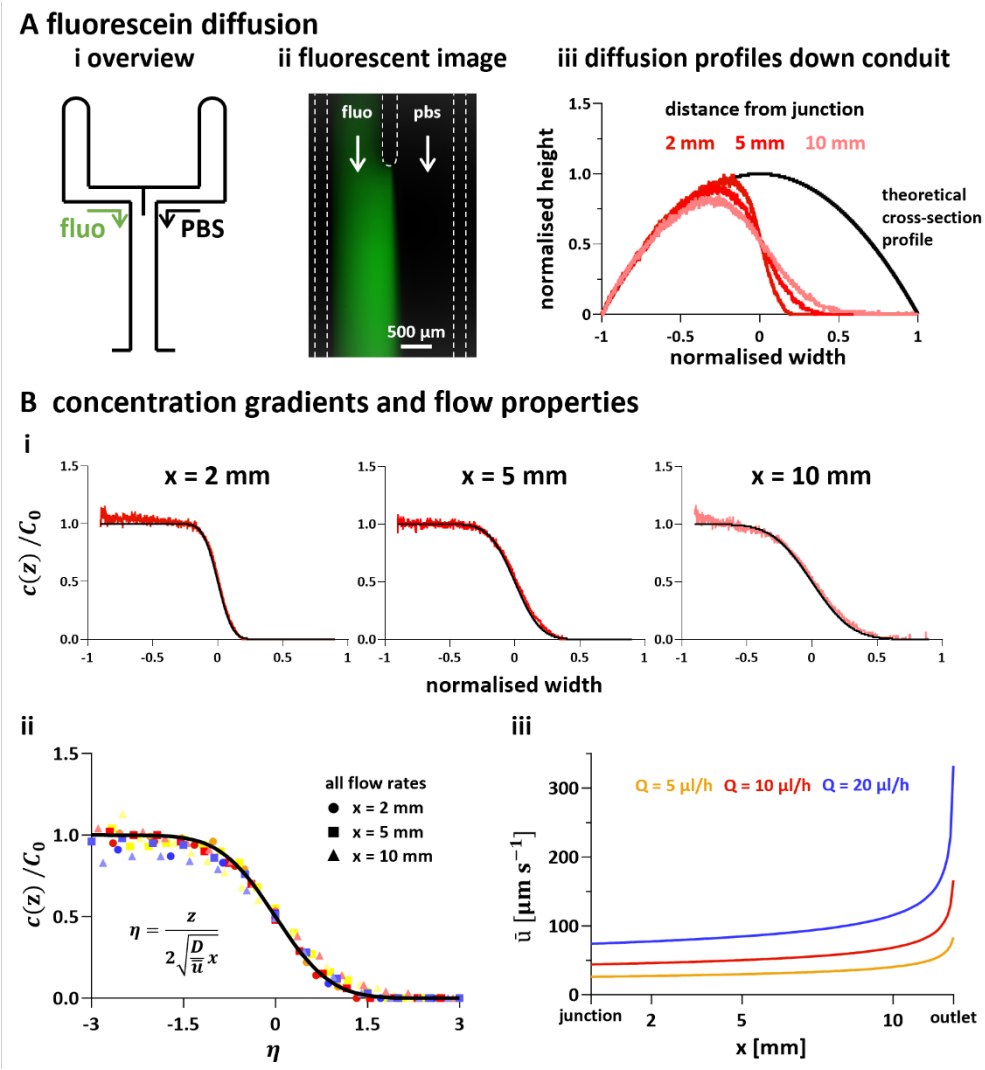

Figure 4. Diffusion of fluorescein from one laminar stream into a fluorescein-free stream flowing at the same rate.

(A) Overview. (**i**) Schematic. Fluorescein solution (fluo) is inputted into the left-hand arm, and PBS into the right-hand one (Q = 10 µl/h; $q_A = q_B$). (**ii**) Representative fluorescent image of the junction. Dashed lines mark fluid walls pinned to the dish. (**iii**) Diffusion profiles across the central conduit at positions 2, 5, and 10 mm from the junction. For each distance from the junction, there is one black curve (derived using Eq. 1) plus an associated red curve (derived from intensities measured in images like that in (A)ii, and then converted to equivalent heights using the calibration factor). Pairs of curves are overlaid by normalizing widths and heights with respect to h_0 on each black curve.

(B) Concentration gradients and flow properties. (**i**) Concentration profiles (red) measured 2, 5, and 10 mm from the junction compared to predictions from Eq. (7) (black line). Experimental gradients are computed as the ratio of a diffusion profile (shown in (A)iii) and the corresponding cross-section profile at each point across the width. (**ii**) Collapsed experimental data for all flow rates tested (for η see Eq. (7); colours refer to flow rates and shapes of data points indicate distances from junction) and predicted curve from Eq. (7) (black line). (**iii**) Mean velocities in the centre of the conduit for different flow rates (from Eq. 3).

The position of the contact plane between parallel streams can also be controlled precisely in our system using Eq. (4). We illustrate this by moving the contact plane away from the centre of the conduit to position $s = -0.5$. Thus, setting $\frac{q_A}{q_B} = 0.0763$ (and $Q = q_A + q_B = 10\ \mu l/h$) should induce the required shift (Fig. 2Biii) – and it does (Fig. 5Ai). Conversely, in solid-walled conduits with fixed height, the same movement would be achieved with $\frac{q_A}{q_B} = 0.25$ (Fig. 5B). Therefore, corrections for local velocities, $\overline{u}(s,x)$, are included when computing concentration profiles using Eq. (7); again, there is good correspondence between theory and experiment.

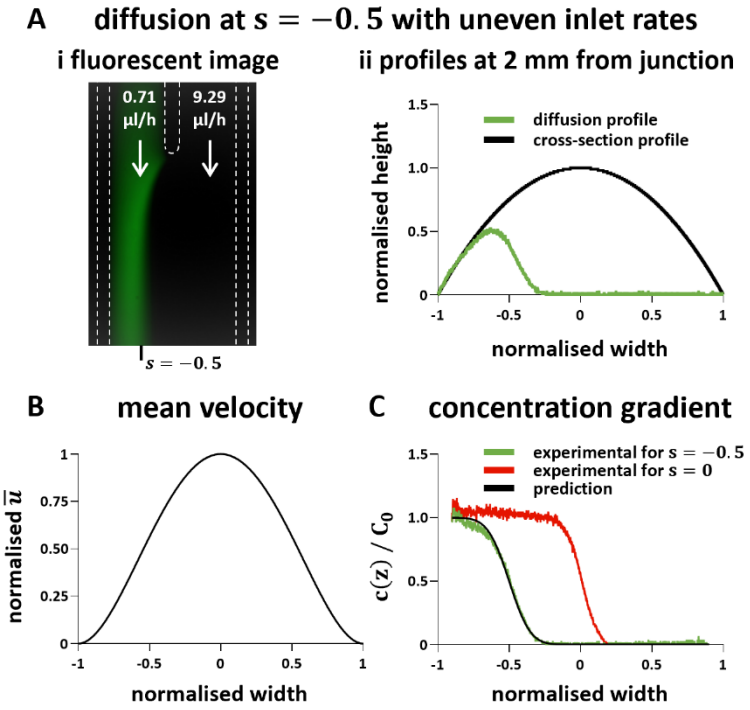

Figure 5. Diffusion of fluorescein between laminar streams with different flow rates.

(A) Diffusion profile for uneven streams with contact line shifted to $s = -0.5$. Conditions to achieve this shift – with $\frac{q_A}{q_B} \sim 10^{-1}$ and $Q = q_A + q_B = 10\ \mu l/h$ – are determined using Figure 2Biii. (**i**) Representative fluorescent image. (**ii**) Experimental diffusion profile (converted from intensity) 2 mm from the junction compared to the theoretical one (from Eq. (1)).

(B) Normalised plot of mean velocity 2 mm from the junction. Unlike rectangular conduits, the velocity profile across the width of the conduit is not parabolic.

(C) Diffusion/concentration profiles (green) measured 2 mm from the junction – derived as in Figure 4Bi – compared to predictions from Eq. (7) (black line). The red curve is reproduced from Figure 4Bi.

Diffusion gradients across three parallel streams

Finally, results from theory and experiment are compared using an extra inlet to give three laminar streams in the central conduit – with two fluorescein streams flanking a central PBS one (Fig. 6A). We position contact plane $s_1 = -0.5$ (as Fig. 5), and $s_2 = 0.5$, by setting $\frac{q_A}{q_C+q_B} = 0.0763$, $\frac{q_A+q_C}{q_B} = 13.09$, and $Q = q_A + q_C + q_B = 10\ \mu l/h$. The normalised equivalent-height profile now has a (green) peak at each edge (compare Fig. 6Bi with Fig. 5Aii,), and the (green) concentration-gradient profile is both symmetrically placed around $z = 0$ and overlaps the predicted one (Fig. 6Bii). We also equalise flow rates using $\frac{q_A}{q_C+q_B} = 0.5$, $\frac{q_A+q_C}{q_B} = 2$, and $Q = q_A + q_C + q_B = 20\ \mu l/h$ (Fig. 6C). This sets $s_1 = -0.15$ and $s_2 = 0.15$ and so should narrow the central stream; it does (Fig. 6Ci), and there is again symmetry plus good correspondence between theory and experiment ((Fig. 6Cii).

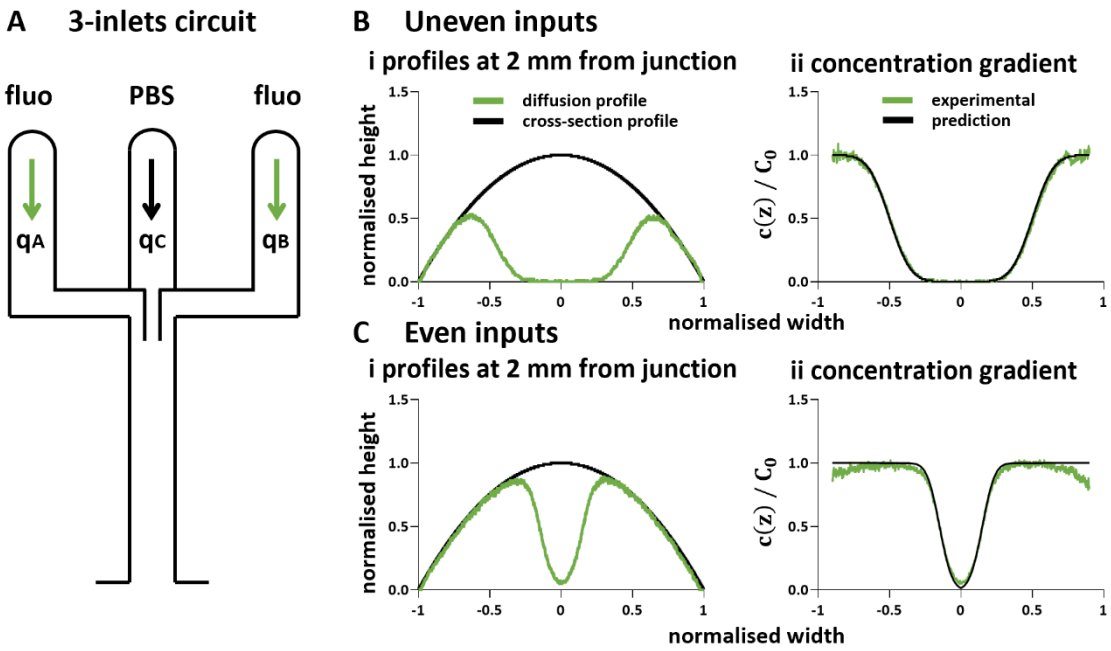

Figure 6. Diffusion of fluorescein between three laminar streams with varying flow rates.
(A) Schematic of the circuit – a trident with three inlets. Fluorescein and PBS alone are inputted as shown.
(B) Diffusion gradients with uneven inputs. $(q_A = q_B = 6.67\ \mu l/h,\ q_C = 8.58\ \mu l/h,\ Q = 10\ \mu l/h)$. Contact planes between streams fall at $s_1 = -0.5$, and $s_2 = 0.5$ $\left(using\ \frac{q_A}{q_C+q_B} \sim 10^{-1},\ \frac{q_A+q_C}{q_B} \sim 10^{1},\ and\ Q = q_A + q_C + q_B = 10\ \mu l/h\right)$. (**i**) Diffusion profile 2 mm from the junction. (**ii**) Concentration profiles (green) measured 2 mm from the junction (derived as in Fig. 4Bi) compared to predictions from Eq. (7)

(black line; the solution across the contact plane in the $0 < s_2 < 1$ range is that for s_1 mirrored around $s = 0$).
(C) Diffusion gradients with even inputs. $(q_A = q_C = q_B = 6.67\ \mu l/h, Q = 20\ \mu l/h)$. Contact planes between streams fall at $s_1 = -0.15$, and $s_2 = 0.15$ $\left(using\ \frac{q_A}{q_C+q_B} = 0.5,\ \frac{q_A+q_C}{q_B} = 2,\ and\ q_A + q_C + q_B = 20\ \mu l/h\right)$. (**i**) Diffusion profile 2 mm from the junction. (**ii**) Concentration profiles (green) measured 2 mm from the junction (derived as in Fig. 4Ai) compared to predictions from Eq. (7) (black line, mirrored as above).

Discussion

The fluid nature of walls in our micro-circuits (Fig. 1) ensures that conduit cross-sections are circular segments (Fig. 2Aii) that morph above unchanging footprints as pressures change (Fig. 2Aiii). This is unlike the unchanging cross-sections found in most conventional circuits with solid walls. Deroy et al. [18] showed such behaviours, proving the cross-sectional area to diminish from inlet to outlet as pressure reduces (Supplementary Fig. 1). The same authors derived a simple equation that predicts pressure-driven morphing of fluid walls in straight conduits with constant flow rate at steady state (Eq. S1). Our aim here is to develop new theory to explain such flows, and validate this theory experimentally.

We begin with a Y-shaped circuit, infuse inputs into the two lateral arms, and monitor laminar flows in the central conduit (Fig. 2Ai). In each straight section, the model proposed by Deroy et al. can be applied, so flow and fluid wall dynamics are fully described by Eq. (1), (2), and (3). When a solute (fluorescein-dextran of 9 kDa) dissolved in PBS is steadily infused into the left-hand arm, and PBS into the right-hand one, the solute diffuses between laminar streams. As the total flow rate is the sum of all inputs ($Q = \sum q_{inlet}$), input ratio defines the stable contact plane between streams (Eq. (4)).

As in previous studies [17,20,21], solute transfer between streams is now modelled assuming one-dimensional diffusion between infinitely large reservoirs (Eq. (7)). However, since cross-sectional areas down the conduit vary, flow velocities on the contact plane also do so; this is a unique characteristic of our system. Moreover, before flow begins, all parts of a circuit share the same negligible internal pressure, and fluid walls lie relatively flat over the footprint. However, once flows begin, pressures increase, and walls morph to reach the shape described

by Eq. (1). Therefore, all measurements are made at least 3 h after flow begins to establish the steady-state that persists for at least 10 h (Supplementary Fig. 3).

Diffusion of our solute between laminar streams is monitored by fluorescence microscopy, and intensities seen in images are converted to concentrations using a linear calibration curve that applies to all conditions used – provided that conduit heights lie within the depth of field of our microscope (Fig. 3). After inputting equal flows into each inlet ($q_A = q_B$), and after varying total flows into the circuit (Q=5,10,or 20 µl/h), diffusion profiles determined experimentally match those predicted using Eq. (7) down the length of the conduit (Fig. 4). Use of a diffusion coefficient for fluorescein-dextran 9 kDa ($D_{exp} = 1.1 \times 10^{-10}\ m^2/s$) provides the best fit with experimental data (Supplementary Fig. 2); this is in reasonable agreement with the theoretical value computed with the Stokes-Einstein equation ($D_{th} = \frac{k_B\,T}{6\pi\mu R} = 1.07 \times 10^{-10}\ m^2/s$), where k_B is the Boltzmann constant, T is room temperature (298.15 K), μ is the dynamic viscosity of the solution assumed to be that of water (0.89 cP), and R is the radius of the diffusing molecule (23 Å) [26]. As flow is laminar, once it reaches steady state diffusion gradients are stable and unchanging over time (Supplementary Fig. 3). The time required to reach stability mostly depends on the geometry of the inlet branches and on inlet flow rates, but it is not deeply analysed in this work. In our circuit geometry and with the slowest flow rate tested ($q_A = q_B = 2.5\ \mu\mathrm{l/h}$, so $Q = 5\ \mu\mathrm{l/h}$), stability of diffusion gradients is achieved after two hours from the beginning of the flow (Supplementary Fig. 3).

Theory is also validated in two additional ways. In one, inputs are infused into the two arms of the Y-shaped circuit at different rates – ones that are predicted to shift the contact plane between laminar streams away from the centre line to a new specified position. Although such a shift changes the mean velocity profile, experiment showed it occurs as expected to yield the appropriate concentration gradient (Fig. 5). The second way involved a trident-shaped circuit with three inlet arms (Fig. 6A). After inputting fluorescein into flanking inlets and PBS into the middle one, three laminar streams now flow side-by-side to yield 2 contact planes; again, predicted and experimentally-determined gradients overlap (Fig. 6B,C).

Finally, our model assumes diffusion across contact planes occurs between infinitely large reservoirs; in other words, we assume flow is significantly faster down the conduit compared to lateral diffusion so that diffused molecules do not affect bulk concentrations in a neighbouring stream. The Fourier (Fo) number (Eq. (8)) is the ratio of diffusion and flow times. When $Fo \ll 1$, our assumption holds and Eq. (7) can be applied. However, if $Fo \geq 1$, it no longer applies. For all experiments with two inlet streams and even input flow rates (Fig. 4, Supplementary Fig. 2), Fo is $\sim 10^{-2}$ for all flow rates tested; then, the model correctly predicts diffusion gradients. However, once the contact plane shifts away from the centre line, our model fits experimental data only at $x = 2$ mm, and becomes progressively less accurate at greater distances from the junction (Fig. 5). For example (Supplementary Fig. 4A), where the fluorescent stream is narrow and the contact plane is close to the left edge of the conduit ($s = -0.5$), its velocity lowers (Fig. 5B) to become comparable to velocity of diffusion; therefore, the initial bulk concentration of fluorescein falls below C_0 and Eq. (7) no longer holds. In this configuration, when $Q = 10$ µl/h, $Fo \sim 0.25$ and theoretical results diverge from experimental ones. Similarly, when $Q = 20$ µl/h, $Fo \sim 0.15$ and our model accurately predicts the gradient up to 5 mm from the junction, but not further away (Supplementary Fig. 4A). Moreover, when contact planes in the trident are close to the centre of the conduit and the central stream of PBS is narrow (Supplementary Fig. 4B), the predictive model again performs poorly (as solute from both sides alters the concentration in the PBS).

Nevertheless, we believe the experimentally-validated theory in this work represents a useful tool to design innovative fluid-walled microfluidic platforms for in-vitro studies on cell chemotaxis [15,17]. In particular, we envision the 3-input circuit will allow studies of the decisions cells make when they sense different chemoattractants; cells plated in the centre of the conduit are exposed to equal concentration gradients of different drugs from either side, and this allows them to ‘choose’ the preferred migrating direction. Such assays, combined with the ability to easily retrieve any cells that have migrated through the fluid walls [16], provide a unique experimental platform for chemotactic studies.

Authors contribution

F.N. and C.D. conceived the project and designed experiments. F.N. performed experiments and analysed all experimental data. P.R.C and E.W. supervised the study. F.N. prepared the manuscript. All authors reviewed the manuscript and approved its submission.

Conflicts of interest

Both P.R.C and E.J.W hold equity in and have received frees from iotaSciences Ltd; the same company provides financial support to F.N

Acknowledgements

This work was supported by iotaSciences Ltd and the Engineering and Physical Sciences Research Council through EP/R513295/1

References

[1] Nau GJ, L Richmond JF, Schlesinger A, Jennings EG, Lander ES, Young RA. Human macrophage activation programs induced by bacterial pathogens. Proceeding of the National Academy of Sciences 2002;99:1503–8.

[2] Ahmed E. Microbial Endocrinology: Interaction of the Microbial Hormones with the Host. Biomed J Sci Tech Res 2020;24.

[3] Lowenhaupt RW, Glueck HI, Miller MA, Kline DL. Factors which influence blood platelet migration. J Lab Clin Med 1977;90:37—45.

[4] Menter DG, Kopetz S, Hawk E, Sood AK, Loree JM, Gresele P, et al. Platelet “first responders” in wound response, cancer, and metastasis. Cancer and Metastasis Reviews 2017;36:199–213.

[5] Stephen Boyden B. The chemotactic effect of mixtures of antibody and antigen on polymorphonuclear leucocytes. The Journal of experimental medicine 1962;115:453-466

[6] Oner A, Kobold S. Transwell migration assay to interrogate human CAR-T cell chemotaxis. STAR Protoc 2022;3.

[7] Grigolato F, Egholm C, Impellizzieri D, Arosio P, Boyman O. Establishment of a scalable microfluidic assay for characterization of population-based neutrophil chemotaxis. Allergy: European Journal of Allergy and Clinical Immunology 2020;75:1382–93.

[8] Sackmann EK, Fulton AL, Beebe DJ. The present and future role of microfluidics in biomedical research. Nature 2014;507:181–9.

[9] Berthier E, Young EWK, Beebe D. Engineers are from PDMS-land, biologists are from polystyrenia. Lab Chip 2012;12:1224–37.

[10] Yu J, Berthier E, Craig A, de Groot TE, Sparks S, Ingram PN, et al. Reconfigurable open microfluidics for studying the spatiotemporal dynamics of paracrine signalling. Nature Biomedical Engineering 2019 3:10 2019;3:830–41.

[11] Deroy C, Nebuloni F, Cook PR, Walsh EJ. Microfluidics on Standard Petri Dishes for Bioscientists. Small Methods 2021;5.

[12] Walsh EJ, Feuerborn A, Wheeler JHR, Tan AN, Durham WM, Foster KR, et al. Microfluidics with fluid walls. Nat Commun 2017;8.

[13] Soitu C, Feuerborn A, Deroy C, Castrejón-Pita AA, Cook PR, Walsh EJ. Raising fluid walls around living cells. Sci Adv 2019;5:8002–7.

[14] Soitu C, Stovall-Kurtz N, Deroy C, Castrejón-Pita AA, Cook PR, Walsh EJ. Jet-Printing Microfluidic Devices on Demand. Advanced Science 2020;7:2001854.

[15] Oliveira NM, Wheeler JHR, Deroy C, Booth SC, Walsh EJ, Durham WM, et al. Suicidal chemotaxis in bacteria. Nat Commun 2022;13.

[16] Deroy C, Wheeler JHR, Rumianek AN, Cook PR, Durham WM, Foster KR, et al. Reconfigurable Microfluidic Circuits for Isolating and Retrieving Cells of Interest. ACS Appl Mater Interfaces 2022;14:25209–19.

[17] Deroy C, Rumianek AN, Wheeler JHR, Nebuloni F, Cook PR, Greaves DR, et al. Assaying Macrophage Chemotaxis Using Fluid-Walled Microfluidics. Adv Mater Technol 2022;7:2200279.

[18] Deroy C, Stovall-Kurtz N, Nebuloni F, Soitu C, Cook PR, Walsh EJ. Predicting flows through microfluidic circuits with fluid walls. Microsystems & Nanoengineering 2021 7:1 2021;7:1–9.

[19] Kamholz AE, Weigl BH, Finlayson BA, Yager P. Quantitative analysis of molecular interaction in a microfluidic channel: The T-sensor. Anal Chem 1999;71:5340–7.

[20] Kamholz AE, Yager P. Theoretical Analysis of Molecular Diffusion in Pressure-Driven Laminar Flow in Microfluidic Channels. Biophys J 2001;80:155–60.

[21] Häusler E, Domagalski P, Ottens M, Bardow A. Microfluidic diffusion measurements: The optimal H-cell. Chem Eng Sci 2012;72:45–50.

[22] Soitu C, Feuerborn A, Tan AN, Walker H, Walsh PA, Castrejón-Pita AA, et al. Microfluidic chambers using fluid walls for cell biology. Proc Natl Acad Sci U S A 2018;115:E5926–33.

[23] Galambos PC, Forster FK. Two-phase dispersion in micro-channels. University of Washington 1998.

[24] Stiles PJ, Fletcher DF. Hydrodynamic control of the interface between two liquids flowing through a horizontal or vertical microchannel. Lab Chip 2004;4:121–4.

[25] Heeren A, Luo CP, Roth G, Ganser A, Brock R, Wiesmueller KH, et al. Diffusion along microfluidic channels. Microelectron Eng 2006;83:1669–72.

[26] Sigma-Aldrich. FLUORESCEIN ISOTHIOCYANATE-DEXTRAN - Product information 1997.

Supplementary Information

Semi-analytical solution for $h_0(x)$

As liquid interfaces are flexible and can expand or retract, the fluid walls/ceilings in our circuits can inflate or deflate over the fixed footprint as inner pressures change. Variation in the shape of the walls changes conduit cross-section, and modifies flow velocities. Recently, Deroy et al. [18] derived a simple power law that describes changes of the central height (h_0) of a straight fluid-walled conduit along its length (L) when a fluid with constant viscosity (μ) flows at constant rate (Q) through it:

$$h_0(x) = \left(\frac{26.08\mu a Q(L-x)}{\gamma} + h_{out}^4\right)^{0.25} \quad \text{(S1)}$$

Here, a represents the half width of the conduit, γ the interfacial tension at the medium-FC40 interface, while h_{out} is the central height of the conduit outlet. These authors also proved this equation to be valid only for conduits with high aspect ratios ($a \gg h_0$).

We build on this work and use Eq. S1 to describe h_0 along conduit length for all flow rates tested, and in Eq. (1), (2), and (3). From calibration intensity profiles that outline shapes of conduit cross sections, we derive the central intensity (at the highest point of the cross section) as the average of all intensity in the centre of the section ($-0.1 < \mathrm{z} < 0.1$). We convert intensity into equivalent heights $h_0(x)$ using the linear relationship described in Figure 3, and find good agreement between experiment and theory for heights less than the depth of field of the microscope (Supplementary Fig. 1).

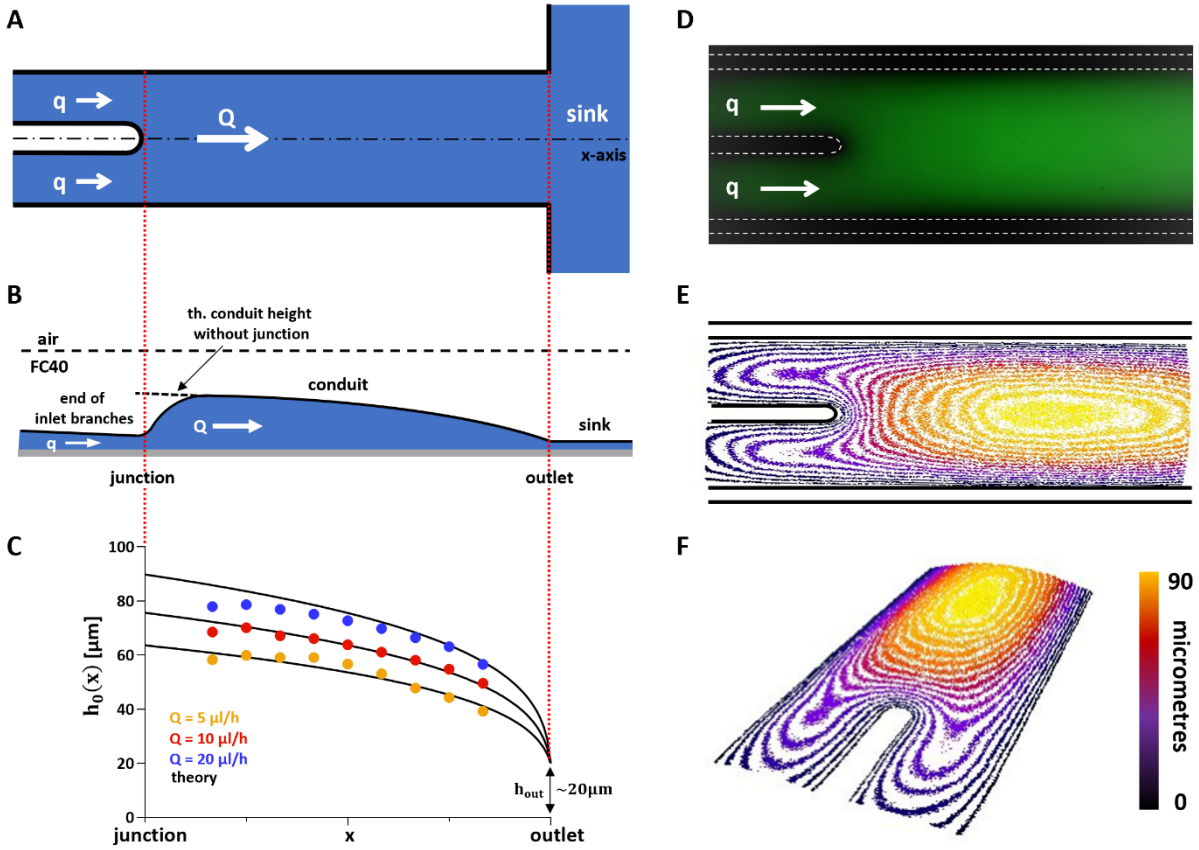

Supplementary Figure 1. Central height profile of the conduit - $h_0(x)$.

(A) Top-view schematic of the circuit.

(B) Side-view schematic of the circuit. At the junction, a sudden change in geometry (inlet branches merge into single conduit with doubled width) induces fluid walls/ceiling to raise. Such variation is not immediate but occurs over 1-2 mm. At around 2 mm from the junction fluid walls/ceiling reach the height predicted by Eq. (S1) and shape described by Eq. (1).

(C) Experimental data compared to the analytical prediction of the central height profile of the conduit. Experimental data (circles) are values of $h_0(x)$ determined from central intensities of cross-section profiles between 2 and 10 mm from the junction for the flow rates indicated, while black lines are the respective theoretical predictions calculated using Eq. (S1).

(D) Representative fluorescent image with both input rates of 10 $\mu l/h$ (same as in Fig. 3A).

(E) Intensity isoline chart of fluorescent image in (D) processed using ImageJ. It shows fluorescent intensity to gradually increase after the junction reflecting variations in fluid walls/ceilings.

(F) 3D isoline chart with intensity converted into equivalent heights. Chart obtained using ImageJ.

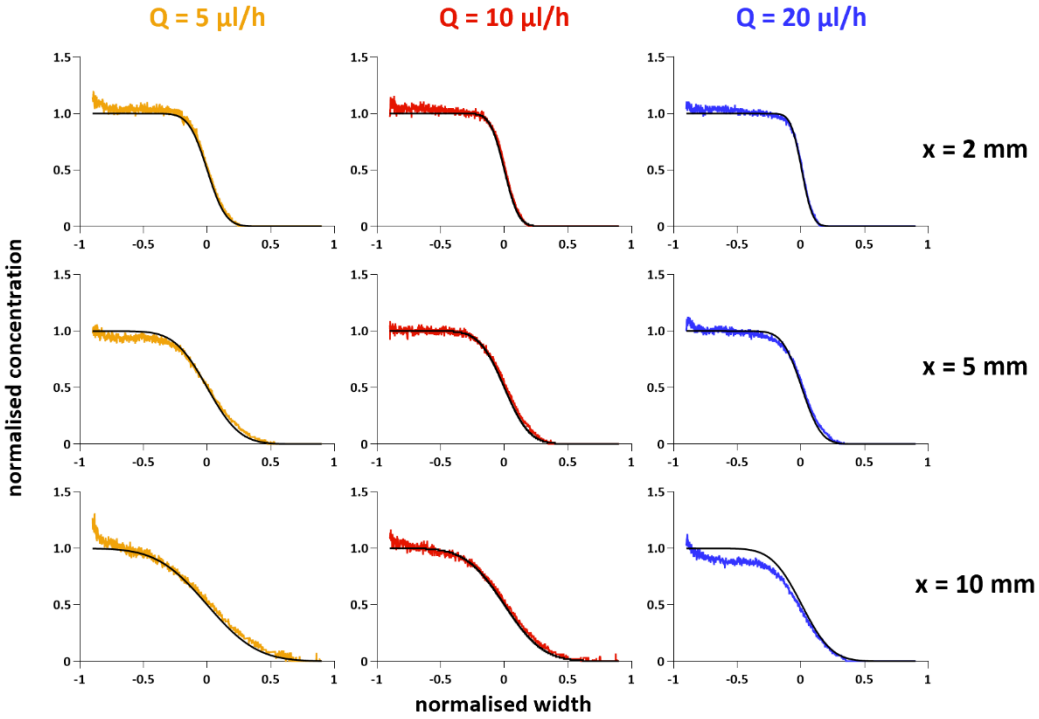

Supplementary Figure 2. Diffusion gradients down the central conduit for all flow rates tested (Y-shaped circuit, conditions as Fig. 4).

As input rates are equal, the contact plane between streams is centred in the conduit and diffusion is symmetric across its width. As expected, gradient steepness decreases towards the outlet ($x_{out} = 12$ mm), but increases at higher rates. Values for $Q = 10$ µl/h are reproduced from Figure 4B.

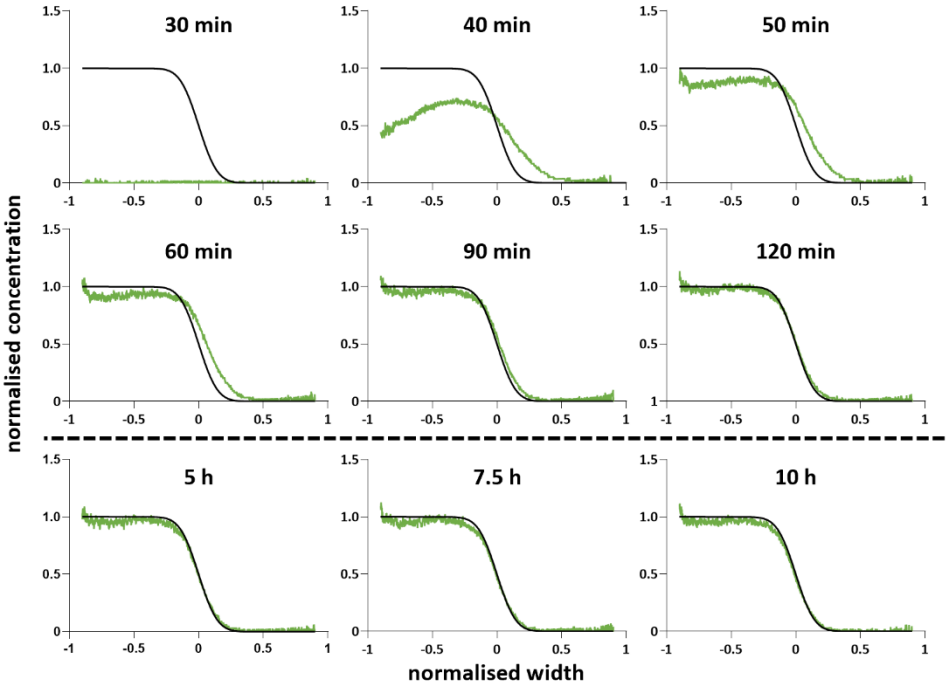

Supplementary Figure 3. Start-up time and stability of diffusion gradients. Conditions are as described in Figure 4B except that *Q* = 5 µl/h with $q_A = q_B$). Graphs show a time-lapse sequence describing the evolution of the concentration gradient across conduit cross-section at 2 mm from the junction. Infusing needles are inserted in the respective input arms and flow started. Time is counted from the moment both samples start releasing from infusing needles, measurements are recorded every 10 min, and concentration gradients determined (as in Fig. 4B). At 40 minutes, the fluorescent solution reaches the imaging area ($x = 2\ mm$) and therefore an intensity profile becomes visible. The shape of the diffusion gradient is significantly different from the predicted one as the flow is not yet fully developed and fluid walls are still morphing to reach their final configuration. When fluid walls stop morphing, concentration values between $-1 \leq z < 0$ equal 1 as the equivalent height profile has equalled the theoretical cross section profile described by Eq.(1). After 40 minutes, the diffusion gradient starts forming across streams. After 2 hours, the gradient reaches its final configuration, in perfect agreement with theoretical predictions (indicated by black lines). After this time, the diffusion gradient remains stable and unchanged. Flow is then stopped after 10 hours. We note that the time taken to reach steady state depends mainly on the geometry of inlet branches and input flow rates, however these dependencies were not explored further in this study.

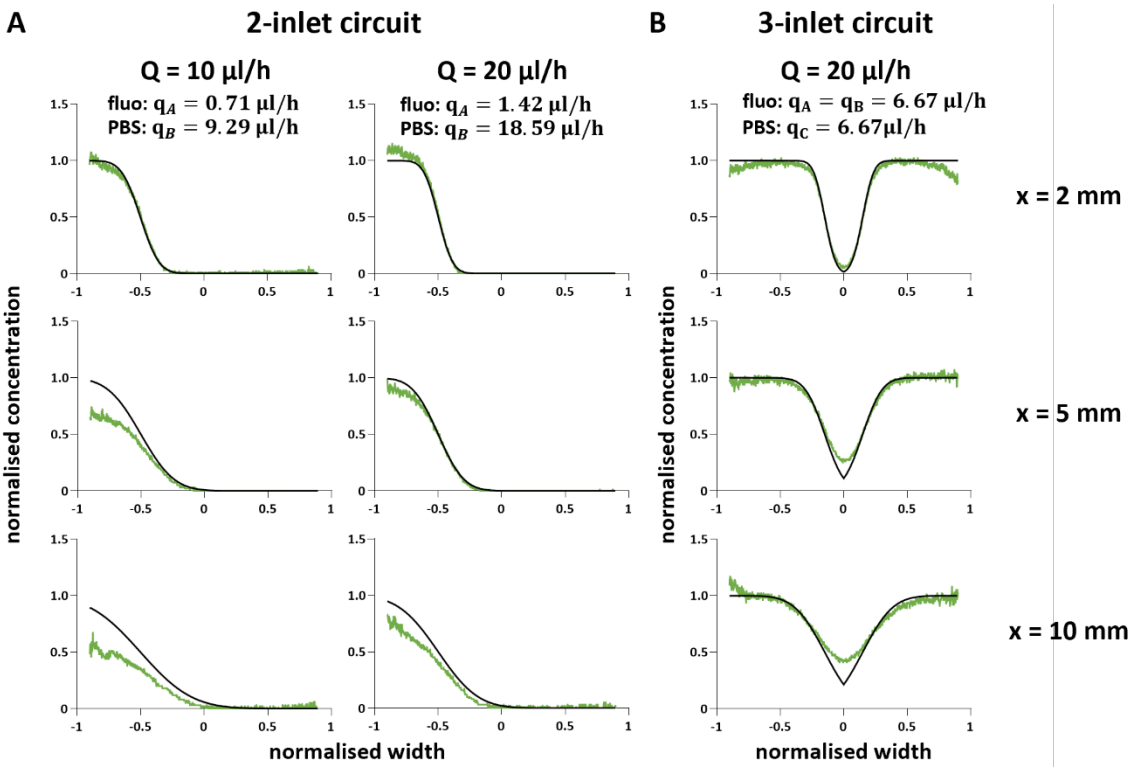

Supplementary Figure 4. Diffusion gradients resulting from off-centre contact planes.

(A) Y-shaped circuits with $q_A < q_B$. Conditions and presentation as in Figure 5, with the differences indicated. Eq. 7 (black line) predicts the diffusion gradient seen experimentally (green) when x = 2 mm, but performs progressively less well with distance from the junction. As $s_1 = -0.5$, velocity of the contact plane lowers (Fig. 5B) and it becomes comparable to diffusion velocity ($Fo \sim 1$); therefore, the fluorescein stream concentration falls below C_0 (and so it can no longer be considered to be diffusing from an infinitely large reservoir). Consequently, the green trace lies below the black line.

(B) Trident. Conditions and presentation as in Figure 6 where fluorescein streams flow on either side of a central PBS stream. Eq. 7 (black line) again predicts the diffusion gradient seen experimentally (green) when x = 2 mm, but performs progressively less well with distance from the junction. Since the contact planes are close to the centre of the conduit ($s_1 = -0.15, s_2 = 0.15$), the volume of PBS in the centre is small, and so the concentration of fluorescein in the PBS stream can no longer be considered as zero. Consequently, the green trace now lies above the black line at position 0.

Statement of Authorship for joint/multi-authored papers for PGR thesis

To appear at the end of each thesis chapter submitted as an article/paper

The statement shall describe the candidate's and co-authors' independent research contributions in the thesis publications. For each publication there should exist a complete statement that is to be filled out and signed by the candidate and supervisor **(only required where there isn't already a statement of contribution within the paper itself).**

Title of Paper	**Stable diffusion gradients in microfluidic conduits bounded by fluid walls**
Publication Status	□Published □ Accepted for Publication **x** Submitted for Publication □Unpublished and unsubmitted
Publication Details	Federico Nebuloni, Cyril Deroy, Peter R. Cook, and Edmond J. Walsh

Student Confirmation

Student Name:	Federico Nebuloni		
Contribution to the Paper	Lead author. Designed experiments in discussion with co-authors and performed all experiments, collected and analysed data, and prepared first draft of the manuscript after discussion with co-authors on layout. Prepared final version and implemented proposed changes prior to submission.		
Signature	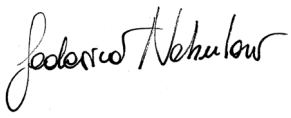	Date	10/10/2023

Supervisor Confirmation

By signing the Statement of Authorship, you are certifying that the candidate made a substantial contribution to the publication, and that the description described above is accurate.

Supervisor name and title: Prof. Edmond J. Walsh		
Supervisor comments Federico designed experiments in discussion with co-authors and performed all experiments, collected and analysed data, and prepared first draft of the manuscript after discussion with co-authors on layout. Prepared final version and implemented proposed changes prior to submission.		
Signature 	Date	12/10/2023

This completed form should be included in the thesis, at the end of the relevant chapter.

Chapter 5: Flow in fluid-walled conduits driven by Laplace pressure

Published on Journal of Fluid Mechanics, vol. 969, p. A28 (July 7, 2023)

Authors: Federico Nebuloni, Peter R. Cook, and Edmond J. Walsh

Abstract

In conventional microfluidic devices, fluids are often confined behind solid plastic walls that restrict access and trap gas bubbles; in open microfluidics, some solid walls are replaced by fluid ones (i.e., interfaces with immiscible fluids). In both cases, flows are usually driven by external pumps or gravity. An innovative open technology has been developed in which 2D patterns of cell-culture medium in standard Petri dishes are confined by fluid walls made of an immiscible and bio-inert fluorocarbon (FC40). To provide refreshing media flows to cells in such circuits, an established pumping system that exploits differences in Laplace pressure across open interfaces has been applied to drive flow without using external pumps: a source drop autonomously empties through a straight conduit into the rest of the dish (the sink). Whereas conduits with solid walls have unchanging boundaries and flows within them are well understood, the challenge is to predict flows in circuits where fluid walls morph as pressures change. Numerical and semi-analytical equations enabling prediction of changing flows are developed, and predictions validated experimentally.

Introduction

Many microfluidics devices had been developed to miniaturize cell culture and better mimic in vivo environments [1]. Conventional devices are often made of solid plastics and standard equations for solid conduits can be applied to describe flow within them [2,3]. When cells are cultured behind solid walls, gas bubbles often cause failures; additionally, solid boundaries prevent direct access to cell cultures which is often a fundamental request of bio-scientists. Consequently, an increasing number of open microfluidic technologies are being developed where some solid boundaries are replaced by liquid interfaces [4,5]. When the Bond number is much less than 1, typically with volumes of one microliter or smaller, fluid behaviour is governed by interfacial forces as the effects of gravity and inertial forces become negligible. Then, an interface between two immiscible fluids can act as a confining wall just as an air/water interface confines rain drops on a windowpane, hence we use the term fluid-wall as a synonym for liquid-liquid interfaces. Microfluidic circuits bounded by such interfaces can be manually/directly accessed simply by piercing through the self-healing liquid walls [6], and they will never fail due to trapped air bubbles (as they spontaneously rise to the surface). Moreover, circuits can be fabricated in standard Petri dishes thus using materials well-known to biologists [7]. However, flows can no longer be predicted using equations derived for conduits with solid and rigid walls [8–12] as the fluid interfaces morph according to pressure.

Recently, an innovative open technology known as ‘fluid-walled microfluidics’ has been developed that is proving especially useful for bio-scientists [13,14]. Cell environments are created in conventional Petri dishes by reshaping a thin layer of cell-culture medium overlaid by an immiscible liquid (often the biocompatible fluorocarbon, FC40). Reshaping is achieved by jetting more FC40 through a nozzle held by a three-way traverse that moves over the dish as it ’draws’ the desired pattern (Fig. 1A) [15]. The FC40 jet sweeps medium away from the substrate, and leaves the overlay tightly pinned to the dish. These pinned walls confine the resulting aqueous circuit, isolating it from its surroundings (Fig. 1B). Such circuits have been used to perfuse cultured cells [15] and to perform chemotactic assays [16]; however, flows

were maintained using complex experimental set-ups and external pumps. Therefore, there is the need to develop automatic ('passive') pumping systems that do not rely on external active pumps. Walker & Beebe [17] proposed a passive pumping system that exploits Laplace pressure to drive flow from a source drop to a sink through a plastic rectangular conduit. A water drop was simply pipetted over an inlet, and the surface tension between water and the surrounding air generated a pressure across the interface (Laplace pressure) that pushed the aqueous phase through the conduit. Here, we use a similar pumping system that relies on Laplace pressure generated across the interface between the patterned medium and the immiscible overlay. Additionally, we propose a closed semi-analytical solution able to predict the flow rate over time while a source drop empties its volume through a fluid-walled conduit of known footprint geometry only (as liquid interfaces above it morph), and we validate the quality of the predictive solutions via experiments.

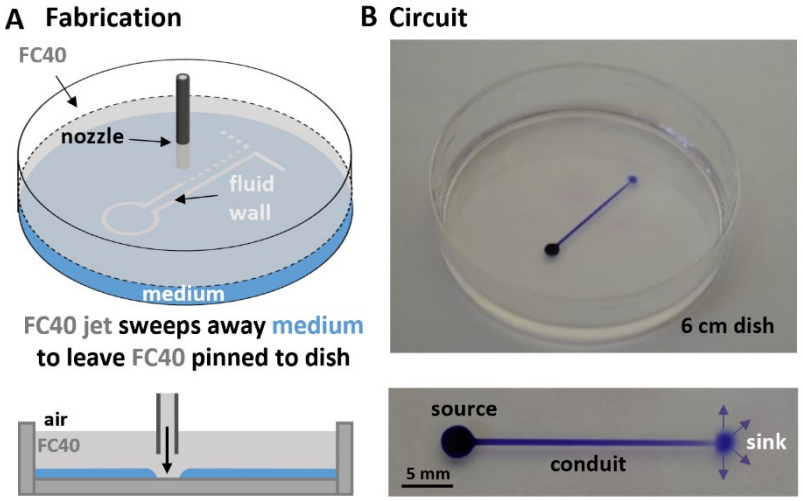

Figure 1: Circuit fabrication.

(A) 3D and side view schematic of the fabrication process.

(B) Example circuit printed in a Petri dish overlaid by clear FC40; close-up top view of the circuit.

Problem formulation

We will consider a simple circuit (Fig. 2Ai,ii) that exploits Laplace pressure to drive flow from the drop (the source), through a straight conduit into the rest of the dish (which acts as a sink). The aqueous phase throughout the circuit is bounded by the polystyrene substrate and

fluid walls (i.e., an interface between two immiscible liquids). Flows driven by Laplace pressure through conduits entirely bounded by solid walls have been widely studied [17–19]. Major determinants of flow include the pressure of the source drop and conduit geometry, with flows declining as the source drop empties. Whilst these determinants apply to our case, the fluid nature of walls introduces additional complexities. For example, conduit cross-section inevitably morphs as pressure falls from inlet to outlet (Fig. 2Aiii). Recently, a simple power law has been proposed to describe height variation of a straight fluid-walled conduit when a constant flow rate is actively perfused through it [20]; it relates cross-sectional conduit height to the decrease in pressure down the length of the conduit. However, in our case, inlet pressure constantly varies as the source drop empties. Calver *et al.* [21] presented an asymptotic analysis of this problem approximated using thin-film equations, but their solution lacks experimental validation and our approach simplifies the solution significantly. Considering the micrometric scale of our system, we assume interfacial forces dominate and pressure differences at all points in the system are exclusively defined by the Young-Laplace equation, $\Delta P = \gamma(1/R_1 + 1/R_2)$, where ΔP is the pressure difference across the interface, γ is the interfacial tension of the pair of fluids, and R_1 and R_2 are two orthogonal radii that describe the curvature of the interfacial surface. In our case, we assume a negligible pressure difference across the sink-FC40 interface as its curvature is extremely small (Fig. 2B) – an approximation that holds as long as the sink is infinitely larger than the source drop. As pressure decreases from source to sink, h_C (central height of the conduit) decreases from a maximum at h_{in} to a minimum at h_{out} (Fig. 2Ai,ii). When pressures in source, conduit and sink are equal, there is no flow through the circuit (Fig. 2Bi). However, filling the source drop increases its curvature, and so source pressure; then, the pressure difference between source (P_{source}) and sink (P_{sink}) drives flow (Fig. 2Bii) which decreases as the source empties (Fig. 2Biii). In contrast to previous works [17–19], conduit cross-section morphs as the source-sink pressure difference varies (Fig. 2Biv). Our challenge is to predict the flow rate ($Q(t)$) through the morphing conduit as pressures change over time.

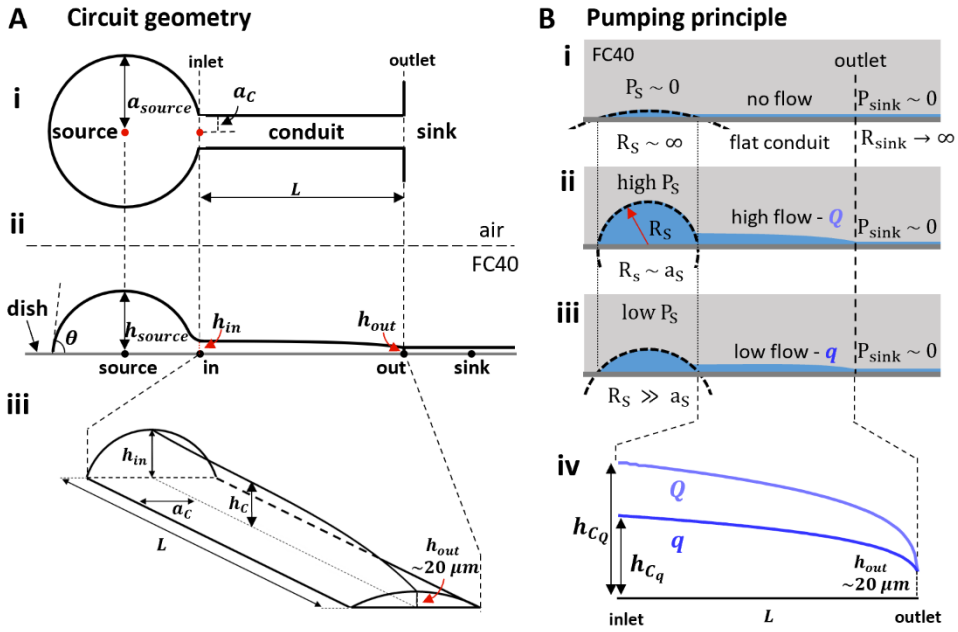

Figure 2: Circuit geometry and pumping principle.

(A) Circuit geometry. (i) Top view. (ii) Side view. (iii) 3D view of the fluid-walled straight conduit.

(B) Flow is driven by changes in Laplace pressure. (i) At equilibrium, all pressures are equal, so there is no flow. (ii) Adding medium to the source, the radius of curvature (R_S) decreases, and Laplace pressure increases. (iii) As the source empties, its Laplace pressure gradually decreases until equilibrium is reached. (iv) As fluid walls are free to morph while pressure diminish, conduit height progressively falls. h_{out} remains unchanged, as it equals the constant pressure of the sink and hence is used as a boundary condition.

Governing equation

Deroy *et al*. [20] derived a differential equation describing h_C variation for fluid-walled conduits with known half width (a_C) along its length (x) when flowing a having constant viscosity (μ) at constant rate (Q):

$$\frac{dh_C}{dx} = \frac{6.55\mu a_C Q}{\gamma h_C^3} \tag{1}$$

which when integrated gives the semi-analytical solution

$$h_C = \left(\frac{26.08\mu a_C Q}{\gamma} x + h_{out}^4\right)^{0.25} \tag{2}$$

where h_{out} is the integrating constant and represents the central height of the liquid interface at the conduit outlet (x = 0, Fig. 2Aii,iii). The authors also demonstrated that the contribution of h_{out} is small and can be neglected away from the outlet (typically $x/a > 5$) for most practical

applications. So for long enough conduits, as those considered in this paper, the second term on the right hand side is neglected. In our model, the flow rate is not constant and flow cannot be at steady-state. However, we assume that morphing liquid interfaces rapidly accommodate pressure changes (i.e., relaxation time is negligible compared to drainage time) so that Eq.2 can model the flow as if at steady-state at each time. In particular, the flow at the inlet of a conduit of length (L) is:

$$Q = \frac{0.038\gamma}{\mu a_C L} h_{in}^4 \tag{3}$$

where h_{in} represents the central height of the conduit cross-section at the inlet and it describes the local pressure (P_{in}). Such pressure can be expressed as $P_{in} = (2\gamma h_{in})/(a_C^2)$ if $h_{in} \ll a_C$. Therefore, Eq.3 becomes:

$$Q = \frac{0.0024 a_C^7}{\mu \gamma^3 L} P_{in}^4 \tag{4}$$

In our case, the flow through the conduit is driven by the pressure of the source drop which is described by considering the geometry of a spherical cap in conjunction with the Young-Laplace equation to give:

$$P_{source} = \frac{4\gamma h_{source}}{a_{source}^2 + h_{source}^2} \tag{5}$$

where a_{source} and h_{source} are the footprint radius and maximum height of the source drop respectively. The equation describing the temporal variation of volumetric flow rate can be derived assuming pressure at the conduit inlet equals the pressure in the source drop. With this assumption, Eq. 4 becomes:

$$Q(t) = 0.613 \frac{\gamma a_C^7}{\mu L} \frac{h_{source}^4(t)}{\left(a_{source}^2 + h_{source}^2(t)\right)^4} = \frac{dV_{source}}{dt} \tag{6}$$

The volume of a spherical cap can be expressed as:

$$V = \frac{\pi}{2} a^2 h + \frac{\pi}{6} h^3 \tag{7}$$

Equation Eq. 7 can be differentiated and substituted into Eq. 6 to obtain the governing differential equation:

$$\frac{dh_{source}}{dt} = -\frac{1.227}{\pi}\frac{\gamma a_C^7}{\mu L}\frac{h_{source}^4(t)}{\left(a_{source}^2 + h_{source}^2(t)\right)^5} \tag{8}$$

This describes the rate of change of the height of the source drop while the drop empties; consequently, the volumetric flow rate through the conduit over time can be found. However, analytical integration of Eq. 8 yields a complex solution, so a Forward-Euler scheme has been employed to numerically solve it. Nevertheless, considering comparatively flat source drops, where $h_{source} \ll a_{source}$, both pressure Eq. 5 and volume Eq. 7 equations can be linearized. This approximation simplifies Eq. 8 to:

$$\frac{dh_{source}}{dt} = -\frac{1.227}{\pi}\frac{\gamma a_C^7}{\mu L}\frac{h_{source}^4(t)}{a_{source}^{10}} \tag{9}$$

to give height of source drop as:

$$h_{source}(t) = \left(\frac{3.681}{\pi}\frac{\gamma}{\mu L}\frac{a_C^7}{a_{source}^{10}}t + \frac{1}{h_0^3}\right)^{-\frac{1}{3}} \tag{10}$$

where h_0 is the height of the source drop at $t = 0$. Then, the variation of drop volume over time is:

$$V_{source}(t) = \left(\frac{29.45}{\pi^4}\frac{\gamma}{\mu L}\frac{a_C^7}{a_{source}^{16}}t + \frac{1}{V_0^3}\right)^{-\frac{1}{3}} \tag{11}$$

where V_0 represents source starting-volume. Eq. 11 represents a semi-analytical solution that predicts the volume decrease of a drop self-emptying into a constant-pressure sink through a fluid-walled conduit whose cross section can morph according to pressure.

Comparison with the numerical solution

Eq. 8 represents the behaviour of flows driven by Laplace pressure in fluid-walled circuits but its solution is non-trivial and can only be achieved through numerical approximations. Linearization of Laplace pressure and sessile drop volume equations allows derivation of a simplified differential equation Eq. 9 that holds when $h_{source} \ll a_{source}$. Figure 3A shows normalized trends of Laplace pressure Eq. 5 and sessile drop volume Eq. 7, in comparison of the respective linearized trend. Both approximations are good predictors for small height-to-radius ratios; for instance, at $h_{source}/a_{source} = 0.3$, the contact angle ($\theta$) equals 33.4° and associated predictive errors of both pressure and volume are below 10% ($\sim$ 9% for pressure and $\sim$ 2.9% for volume). However, both pressure and volume equations diverge from linear approximations as θ approaches 90° ($h_{source}/a_{source} \to 1$). Therefore, if initially $h_0/a_{source} = 0.3$, the analytical solution shows good agreement with the numerical one (Fig. 3Bi, arrows). Conversely, if h_0/a_{source} is ~ 1 (Fig. 3Bii, arrow heads), the two solutions initially diverge as source pressure and volume are poorly described by the linearized approximations. Nevertheless, as the drop empties, pressure and volume linearize, and solutions converge. In conclusion, we showed the derived solution to be an excellent analytical predictor of Laplace-driven flows if initial contact angle of the source drop is small (an arbitrary threshold has been chosen at $h_0/a_{source} = 0.35$ corresponding to $\theta \sim 40°$, and $V_0/(a_{source}^3) = 0.55$). For greater contact angles and volumes, prediction is initially poor but quickly improves as θ falls below the chosen threshold.

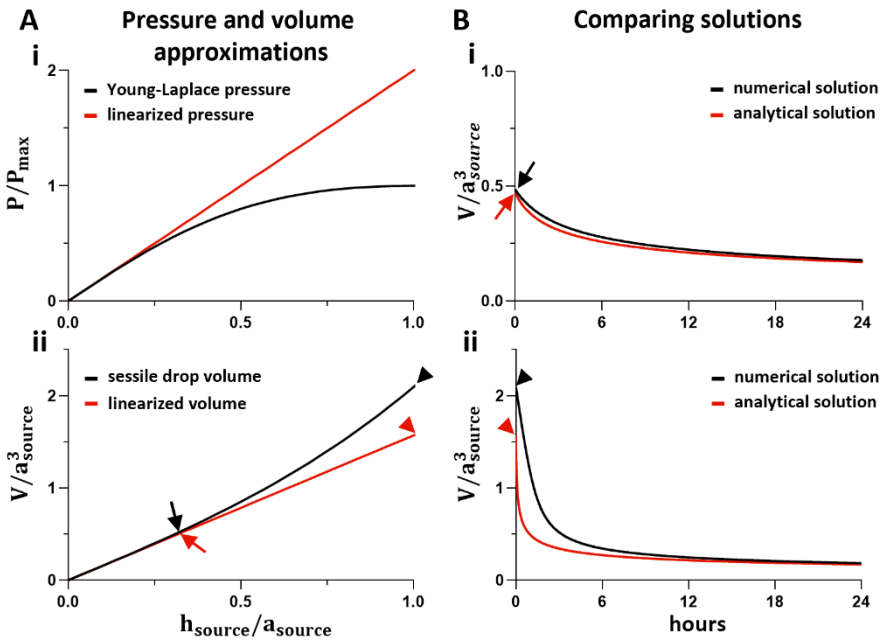

Figure 3. Comparing analytical and numerical solutions.

(A) Pressure and volume approximations (red) are compared to real trends (black). (i) Young-Laplace equation (P_{max}: drop pressure if $\theta = 90°$ and $h_{source}/a_{source} = 1$), (ii) Sessile drop volume.

(B) Analytical and numerical solutions are compared for different initial volumes. (i) For small initial volumes (arrows, $h_{source}/a_{source} = 0.3$). (ii) For large starting volumes (arrow heads, $h_{source}/a_{source} = 1$).

Drainage time

The time needed by a hydraulic system to empty its reservoir is usually known as the drainage time. In our case, it is the time taken for the source drop to empty through the fluid-walled conduit. From the semi-analytical solution Eq. 11, the drainage time is:

$$t_{drain} = \frac{\pi^4 \mu L a_{source}^{16}}{29.45 \gamma a_C^7} \frac{1 - D^3}{D^3 V_0^3} \tag{12}$$

where D is the fraction of the initial volume left in the source drop ($0 < D < 1$) after a time $t = t_{drain}$. Although for high initial contact angle the error is large, as the contact angle reduces, the analytical solution approaches the numerical solution. This is a result of most of the emptying time being spent at low h_{source}/a_{source} values (Fig. 4B). Therefore, Eq. 12 can be applied for all values of D only in the range $0 < V_0/(a_{source}^3) \leq 0.55$. Outside of this range, as the analytical solution initially diverges from the numerical one, drainage times are

computed within a 10% error only if $D < 0.1$. In particular, for a drop with a 90° contact angle ($h_0/a_{source} = 1, V_0/a_{source}^3 = 2.09$), the associated error in predicting the time needed to empty 50% of the initial volume ($D = 0.5$) is above 92%, while to empty 95% of the initial volume ($D = 0.05$) the numerical and analytical solution converge to give errors of $\sim 7\%$.

Experimental setup

All circuits are created on standard clean polystyrene Petri dishes (Thermo Scientific™ Nunc™ Rectangular Dishes single well; for Fig. 1, 6 cm Corning TCT dishes are used). First, the dish is filled with 5 ml cell medium (Dulbecco's Modified Eagle Medium [DMEM] + 10% fetal bovine serum [FBS] both from Gibco) to wet its surface, the same volume is then carefully removed in order to leave just a thin layer wetting the surface. This layer is then quickly overlaid with ~10 ml silicon oil (Si oil; 5 cSt), tetradecane, or FC40 to prevent evaporation. The dish is placed on the platform of a 3D traverse (Hylewicz CNC-Technik). The tip of a blunt needle (70 μm inner diameter, iotaSciences Ltd) held by the traverse is lowered into the overlaying silicone oil or tetradecane until ~0.3 mm above the bottom of the dish, and FC40 is jetted out of the needle at 480 μl/min using a syringe pump (PhD Ultra, Harvard Apparatus) equipped with a 2.5 ml glass syringe (Hamilton). The jet sweeps the DMEM layer off the substrate while the needle is dragged ~0.3 mm above the dish by the traverse. Commands controlling the path followed by the traverse are written using G code. Finally, FC40 used for jetting (immiscible with media, tetradecane, and silicone oil) which accumulates in blobs in the silicone oil or tetradecane is gently removed manually using a 1 ml lab pipette (when FC40 is used as overlay there is no need for this). Images of circuits (Fig. 1) were collected using an Olympus D7100 camera. In Figure 1, blue dye (resazurin sodium salt at 4 mg/ml in distilled water) was added solely to improve visibility. In order to perform flow tests, a syringe pump (PhD Ultra, Harvard Apparatus) is equipped with a 50 μl glass syringe (Hamilton) connected to a blunt metal needle (33G blunt NanoFil™ needle, World Precision Instruments) through a Teflon tube. Next, the needle (held by a 3D-printed holder) is gently lowered manually until the tip just pierces the overlay-medium interface in the middle of the source drop. Additional

medium (DMEM + 10% FBS) is now infused to fill the source drop with the desired initial volume, and then the needle is withdrawn. Images of the source drop are recorded using a camera (First Ten Angstrom) (Fig. 4A), and drop heights (h_{source}) determined using FTA32 software (First Ten Angstrom). The outer diameter of the needle (210 μm) is used as a reference length scale. The heights of source drops are measured on each image collected at a different time; then, flow rates are calculated using Eq. 6, and volumes using Eq. 7.

Results

Source drops with contact angles smaller than 40°

To validate the proposed semi-analytical models, heights of source drops emptying through conduits of known geometry ($a_C = 0.29$ mm) were recorded every 15 min (Fig. 4A,B); then, volumes are computed using spherical-cap geometry, and compared with ones calculated using Eq. 11 (Fig. 4Ci) – using $\gamma_{DMEM_{+10\%FBS}:Sioil} = 11\ \mathrm{mN/m}$ (a value obtained by pendant-drop tensiometry). Silicon oil was chosen as the overlay because its density ($\rho_{Sioil} = 913\ \mathrm{kg/m^3}$) almost matches that of medium (assumed to be that of water). Consequently, contributions from any hydrostatic forces (not included in Eq. 11) will be minimal. Source drops were also initially filled with small volume (V_0 = 1.57 μl and $a_{source} = 1.44$ mm) to ensure $V_0/a_{source}^3 < 0.55$ so $\theta_0 < 40°$. The analytical solution yields volumes and flow rates that match experimentally-determined ones (Fig. 4Ci,ii). Once again, comparison with the numerical solution reveals the capability of the analytical solution to predict the fluid flow. In addition, we find the assumptions used to develop the model to be appropriate given the agreement between the numerical model and the experimental data.

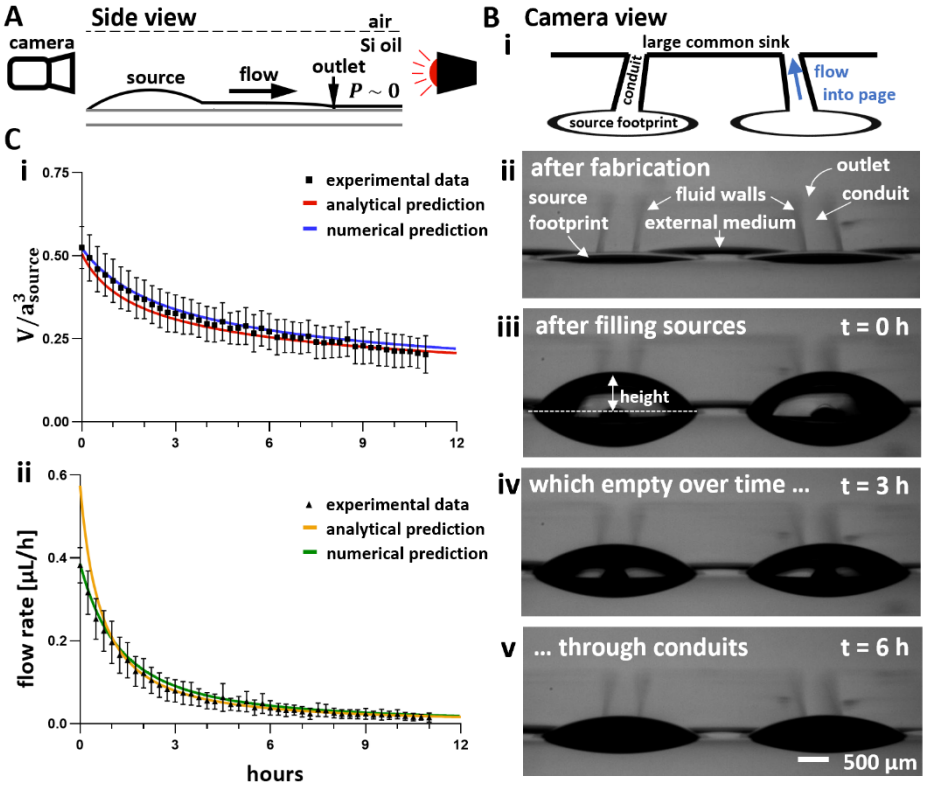

Figure 4. Experimental validation of derived solutions.

(A) Cartoon illustrating experimental set-up from the side.

(B) Experimental images of two parallel circuits. (i) Schematic of the camera view. (ii) The initial state with no flow. (iii-v) After filling source drops, drop heights decrease as medium is pumped out of the sources.

(C) Changes in volume (i) and flow rate (ii) determined experimentally match predicted ones. Error bars indicate standard deviation (n=3).

Source drops with contact angles greater than 40°

Analogous experiments were performed to validate the numerical solution for any initial volume of source drop. As here there is no requirement that $V_0/a^3_{source} < 0.55$, a value $V_0/a^3_{source} \sim 1$ ($\theta_0 \sim 65°$) was used with V_0 = 3.3 µl. Now, numerical curves match the shape of experimental ones, but with a consistent offset (Fig. 5A). In accord with common practice when dealing with microliter volumes, we have assumed thus far that the effects of gravity are negligible. To investigate whether gravitational effects contribute to the offset, we used tetradecane (Fig. 5B) and FC40 (Fig. 5C) as overlays as they have densities significantly lower and higher than the aqueous phase respectively ($\rho_{tetradecane}$ = 762 $\mathrm{kg/m^3}$, ρ_{FC40} =

1850 $\mathrm{kg/m^3}$, with V_0 = 4.1 µl). Whilst the trends seen experimentally are consistent with expectations, results are nevertheless complex. Thus, the emptying rate falls as overlay density increases (Fig. 5D); the hydrostatic head of dense FC40 slows source emptying more than that of lighter tetradecane (with silicone oil being in the middle). However, the shapes of all experimental curves overlap predicted curves poorly – which suggests that other complicating factors may play additional roles. It is worth noting there is an error within 2.5% and 4.5% between the volume infused by the pump and the one calculated using sessile drop geometry from experimental measurements. Such errors can be explained by the presence of small amounts of medium (between 50 and 100 nl) left in the circuit after printing. All predictions are computed using the volume calculated from geometry not the 'programmed' one infused by the pump.

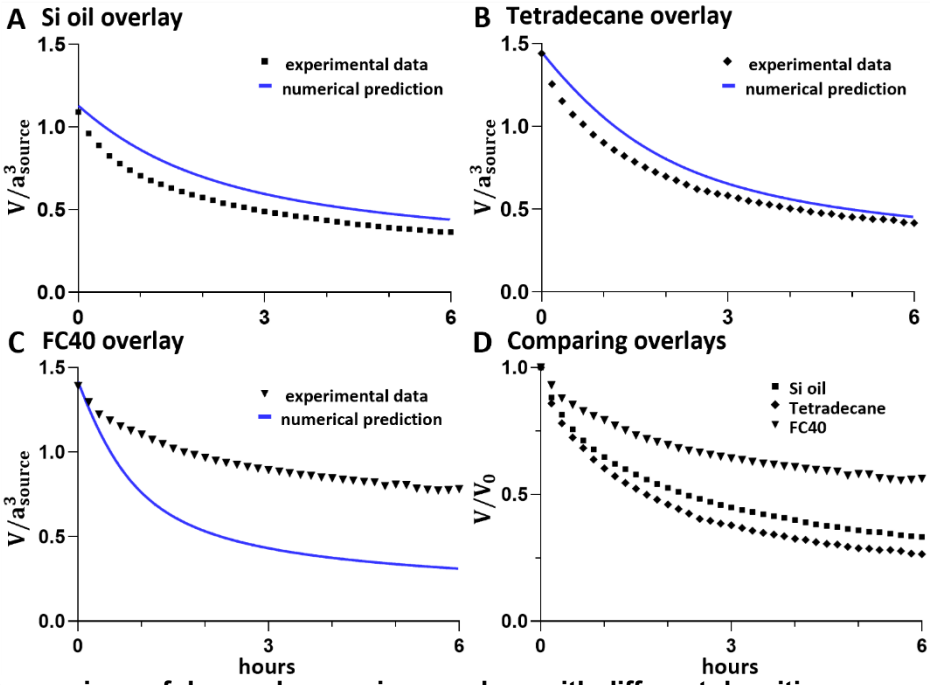

Figure 5. Comparison of drop volume using overlays with different densities.

(A) Silicone oil ($\theta_0 = 65.9°$, $h_0/a_{source} = 0.6$, $\gamma_{DMEM_{+10\%FBS}:Sioil} = 11$ mN / m).

(B) Tetradecane ($\theta_0 = 75.1°$ $h_0/a_{source} = 0.77$, $\gamma_{DMEM_{+10\%FBS}:Tetradecane} = 12.3$ mN / m).

(C) FC40 ($\theta_0 = 74.3°$, $h_0/a_{source} = 0.75$, $\gamma_{DMEM_{+10\%FBS}:FC40} = 22.8$ mN / m).

(D) Comparison of experimental results with different overlays. Data are normalized over initial volume (V_0) to enhance differences in emptying rates. Experimental data represent average value of 3 replicates.

Discussion

Our circuit consists of a drop, intrinsically pressurized according to the Young-Laplace equation, connected to a sink through a fluid-walled conduit (Fig. 2A). The aim is to predict flow rate as function of time as the source drop empties its volume through the conduit with morphing fluid walls (Fig. 2B). Flows driven by Laplace pressure through micro-conduits with solid walls that have unchanging boundary conditions have been studied extensively [17–19]. Here, we build on a power law that describes height changes of cross-sections of a fluid-walled conduit [20], develop a semi-analytical solution to predict how the height Eq. 10, and volume Eq. 11 of the source drop decrease over time, and validate predictions experimentally (Fig. 4Ci). Eq. 11 enables prediction of volumes, pressures, and flow rates at any time. Additionally, it allows quick estimation of drainage time Eq. 12 within 10% error. This solution assumes liquid interface bounding the circuit to morph rapidly in response to pressures changes. Such an assumption enables an approximate calculation of the flow with time; flow rate is constant at all cross-sections of the conduit at any time. This assumption is confirmed by the time scale analysis proposed by Calver *et al.* [21]. Using thin-film asymptotics analysis, they showed that the ratio of the relaxation to drainage time was three orders of magnitude and thereby supporting the quasi steady-state approach taken here. Therefore, we can consider the central height of the liquid interface along the conduit to be fully described by Eq. 2. As flow rate decreases over time Eq. 6, so does conduit height but we assume zero time is needed to accommodate the change. The derived model requires knowledge of the footprints of the source and conduit, the initial height of the source drop, the viscosity of the flowing liquid, and the interfacial tension. The initial height of the source drop sets the starting pressure and can be easily calculated knowing the volume infused into the source. However, this solution only applies to shallow drops (where $h_{source} \ll a_{source}$), so we also develop a numerical solution enabling prediction of the variation in the volume of the source irrespective of starting volume. Experiments performed under silicon oil show that this numerical solution predicts the reduction in drop volume reasonably well, but with an offset of ~13% (Fig. 5A). Despite our

use of microliter volumes, we hypothesized that the increasing discrepancy between experimental and theoretical results might be due to increasing density differences between the two fluids and the resultant hydrostatic head. For example, overlaying dense FC40 (ρ_{FC40} = 1850 $\mathrm{kg/m^3}$) instead of silicone oil (ρ_{Sioil} = 913 $\mathrm{kg/m^3}$) should double the emptying rate as the measured tension of the medium-FC40 interface is double compared to the medium-SiOil one ($\gamma_{DMEM_{+10\%FBS}:FC40} = 22.8\ \mathrm{mN/m}$ and $\gamma_{DMEM_{+10\%FBS}:Sioil} = 11\ \mathrm{mN/m}$). However, the emptying rate decreases significantly (Fig. 5D) probably due to the 10-fold difference between the hydrostatic head of FC40 and SiOil. As FC40 is denser than medium, pressure in the underlaying aqueous phase is eased by buoyancy forces. Conversely, lighter tetradecane burdens source drops with extra pressure and so emptying rate increases (Fig. 5D). Figure 5 shows increasing divergence between experimental and numerical predictions as the hydrostatic-head component increases in importance (~5% for silicone oil, ~15% for tetradecane, and ~30% for FC40 when $\theta_0 = 70°$). Nevertheless, experimental and numerical predictions will always converge in long experiments when the no-flow conditions is reached. Finally, we also assume a constant value of interfacial tension. However, the culture medium we use is supplemented with fetal bovine serum, and so contains a complex mixture of proteins and surfactants. When using pendant-drop tensiometry to measure the interfacial tension of medium in FC40, we observe a decline in interfacial tension over time. This is caused by the adsorption of suspended proteins on to the interface [22, 23] and introduces a time-dependent variable not currently included in our semi-analytical or numerical solutions. All overlaying fluids tested show a 40% reduction in interfacial tension towards a constant equilibrium value (that is used in our model). While most changes in interfacial tension will occur immediately after printing the circuit and before beginning the experiment, we cannot *a priori* exclude a small contribution due to such a change during the operation of the circuit. Nevertheless, we assume such changes in interfacial tension to be small relative to the larger effects due to density differences. Despite these shortcomings, the use of fluid-walled systems for feeding cells should prove useful to bio-scientists. For example, existing passive-pumping

systems driven by Laplace pressure generate flows for minutes [17, 18], but their micrometric drops were directly exposed to air and so soon evaporate or require a detailed setup that prevents this from happening. Conversely, our immiscible overlays reduce evaporation so that flows driven by Laplace pressure can be performed for hours; for example, flows have been sustained for 24 h (not shown). As reducing conduit width by 10% doubles emptying time, much longer times are possible. Additionally, immiscible overlays pin the aqueous phase to the substrate, so drastically increasing the difference between advancing and receding contact angles [13]. These characteristics, together with all benefits introduced by fluid-walled microfluidics [6], make our system particularly suitable to be widely employed by bio-scientists to automatically perfuse their cultures.

Significance and conclusions

We describe a microfluidic technology where liquid interfaces confine an aqueous phase sitting on standard Petri dishes. In applications for bio-scientists, it uses culture media overlaid with a bio-inert fluorocarbon (FC40). Interfaces between two liquids – FC40 and the medium – firmly pin the microfluidic circuit to the dish, and allow users to directly access every point in it from above at any time. The FC40 overlay prevents evaporation of the underneath micrometric aqueous phase which will otherwise dry out in minutes, and it increases the amount of volume each circuit can contain as it significantly broadens the difference between receding and advancing contact angle. Here, we derive a simple power law that describes Laplace-pressure-driven automatic flows of cell culture media through conduits bounded by upper fluid interfaces, and validate this law experimentally. We believe this semi-analytical solution will help many bio-scientists design their microfluidic circuits bounded by liquid interfaces of any kind.

Funding. This work was supported by ‘iotaSciences Ltd’ and ‘Engineering and Physical Sciences Research Council’ - EP/R513295/1 (who both provide financial support to F.N.)

Declaration of interests. Both P.R.C and E.J.W hold equity in and have received frees from iotaSciences Ltd; the same company provides financial support to F.N.

References

[1] Huh D, Matthews BD, Mammoto A, Montoya-Zavala M, Yuan Hsin H, Ingber DE. Reconstituting organ-level lung functions on a chip. Science (1979) 2010;328:1662–8.

[2] Stone HA, Stroock AD, Ajdari A. Engineering Flows in Small Devices: Microfluidics Toward a Lab-on-a-Chip.

[3] Zhou J, Papautsky I. Fundamentals of inertial focusing in microchannels. Lab Chip 2013;13:1121–32.

[4] Feng S, Mao S, Dou J, Li W, Li H, Lin JM. An open-space microfluidic chip with fluid walls for online detection of VEGF: Via rolling circle amplification. Chem Sci 2019;10:8571–6.

[5] Dunne P, Adachi T, Dev AA, Sorrenti A, Giacchetti L, Bonnin A, et al. Liquid flow and control without solid walls. Nature 2020;581:58–62.

[6] Soitu C, Feuerborn A, Deroy C, Castrejón-Pita AA, Cook PR, Walsh EJ. Raising fluid walls around living cells. Sci Adv 2019;5:8002–7.

[7] Berthier E, Young EWK, Beebe D. Engineers are from PDMS-land, biologists are from polystyrenia. Lab Chip 2012;12:1224–37.

[8] Towell GD, Rothfeld LB. Hydrodynamics of rivulet flow. AIChE Journal 1966;12.

[9] Qian S, Joo SW, Jiang Y, Cheney MA. Free-surface problems in electrokinetic micro- and nanofluidics. Mech Res Commun 2009;36:82–91.

[10] Raj A, Suthanthiraraj PPA, Sen AK. Pressure-driven flow through PDMS-based flexible microchannels and their applications in microfluidics. Microfluid Nanofluidics 2018;22:1–25.

[11] Christov IC, Cognet V, Shidhore TC, Stone HA. Flow rate-pressure drop relation for deformable shallow microfluidic channels. J Fluid Mech 2018;841:267–86.

[12] Martínez-Calvo A, Sevilla A, Peng GG, Stone HA. Start-up flow in shallow deformable microchannels. J Fluid Mech 2019;885.

[13] Walsh EJ, Feuerborn A, Wheeler JHR, Tan AN, Durham WM, Foster KR, et al. Microfluidics with fluid walls. Nat Commun 2017;8.

[14] Vallone VF, Telugu NS, Fischer I, Miller D, Schommer S, Diecke S, et al. Methods for Automated Single Cell Isolation and Sub-Cloning of Human Pluripotent Stem Cells. Curr Protoc Stem Cell Biol 2020;55.

[15] Soitu C, Stovall-Kurtz N, Deroy C, Castrejón-Pita AA, Cook PR, Walsh EJ. Jet-Printing Microfluidic Devices on Demand. Advanced Science 2020;7:2001854.

[16] Deroy C, Rumianek AN, Wheeler JHR, Nebuloni F, Cook PR, Greaves DR, et al. Assaying Macrophage Chemotaxis Using Fluid-Walled Microfluidics. Adv Mater Technol 2022;7:2200279.

[17] Walker GM, Beebe DJ. A passive pumping method for microfluidic devices. Lab Chip 2002;2:131–4.

[18] Berthier E, Beebe DJ. Flow rate analysis of a surface tension driven passive micropump. Lab Chip 2007;7:1475–8.

[19] Chen IJ, Eckstein EC, Lindner E. Computation of transient flow rates in passive pumping micro-fluidic systems. Lab Chip 2009;9:107–14.

[20] Deroy C, Stovall-Kurtz N, Nebuloni F, Soitu C, Cook PR, Walsh EJ. Predicting flows through microfluidic circuits with fluid walls. Microsystems & Nanoengineering 2021 7:1 2021;7:1–9.

[21] Calver SN, Gaffney EA, Walsh EJ, Durham WM, Oliver JM. On the thin-film asymptotics of surface tension driven microfluidics. J Fluid Mech 2020;901.

[22] Saad SMI, Policova Z, Neumann AW. Design and accuracy of pendant drop methods for surface tension measurement. Colloids Surf A Physicochem Eng Asp 2011;384:442–52.

[23] Bagnall RD. Adsorption of plasma proteins on hydrophobic surfaces. I. Albumin and γ-globulin. J Biomed Mater Res 1977;11:947–78.

[24] Beverung CJ, Radke CJ, Blanch HW. Protein adsorption at the oil/water interface: characterization of adsorption kinetics by dynamic interfacial tension measurements. vol. 81. 1999.

Statement of Authorship for joint/multi-authored papers for PGR thesis

To appear at the end of each thesis chapter submitted as an article/paper

The statement shall describe the candidate's and co-authors' independent research contributions in the thesis publications. For each publication there should exist a complete statement that is to be filled out and signed by the candidate and supervisor **(only required where there isn't already a statement of contribution within the paper itself).**

Title of Paper	**Flow in fluid-walled conduits driven by Laplace pressure**
Publication Status	**x** Published □ Accepted for Publication □ Submitted for Publication □Unpublished and unsubmitted
Publication Details	Federico Nebuloni, Peter R. Cook, and Edmond J. Walsh Published on Journal of Fluid Mechanics, vol. 969, p. A28 (July 7, 2023)

Student Confirmation

Student Name:	Federico Nebuloni		
Contribution to the Paper	Lead author. Designed experiments in discussion with co-authors and performed all experiments, collected and analysed data, and prepared first draft of the manuscript after discussion with co-authors on layout. Prepared final version and implemented proposed changes prior to submission.		
Signature	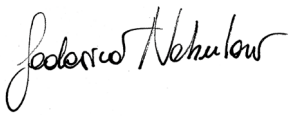	Date	10/10/2023

Supervisor Confirmation

By signing the Statement of Authorship, you are certifying that the candidate made a substantial contribution to the publication, and that the description described above is accurate.

Supervisor name and title: Prof. Edmond J. Walsh		
Supervisor comments Federico designed experiments in discussion with co-authors and performed all experiments, collected, and analysed data, and prepared first draft of the manuscript after discussion with co-authors on layout. Prepared final version and implemented proposed changes prior to submission.		
Signature 	Date	12/10/2023

This completed form should be included in the thesis, at the end of the relevant chapter.

Chapter 6: A fluid-walled microfluidic platform for human neuron microcircuits and directed axotomy

Submitted to Lab on a Chip on February 1st, 2024

Authors: Federico Nebuloni, Quyen Do, Richard Wade-Martins, Peter R. Cook, and Edmond J. Walsh

Abstract

In our brains, different neurons make appropriate connections; however, there remain few *in-vitro* models of such circuits. We use an open microfluidic approach to build and study neuronal circuits *in vitro* in ways that fit easily into existing bio-medical workflows. Dumbbell-shaped circuits are built in minutes in standard Petri dishes; the aqueous phase is confined by fluid walls – interfaces between cell-growth medium and an immiscible fluorocarbon, FC40. Conditions are established that ensure post-mitotic neurons (derived from human iPSCs) plated in one chamber of a dumbbell remain where deposited. After seeding cortical neurons on one side, axons grow through the connecting conduit to ramify amongst striatal neurons on the other – an arrangement mimicking unidirectional cortico-striatal connectivity. We also develop a moderate-throughput non-contact axotomy assay. Cortical axons in conduits are severed by a media jet; then, brain-derived neurotrophic factor and striatal neurons in distal chambers promote axon regeneration. As additional conduits and chambers are easily added, this opens up the possibility of mimicking complex neuronal networks, and screening drugs for their effects on connectivity.

Introduction

Various in-vitro methods have demonstrated the requirement for complex culture systems to support neuronal maturation and the manifestation of associated disease [1–3]. Microfluidic approaches have yielded particularly promising results, as they enable isolation of different cellular compartments (e.g., somas, dendrites, axons) [4,5]. Compared to conventional in-vitro cultures, they also permit precise control of cellular environments, and have proven useful in studies on neurotoxicity [6] and electrical connectivity [7,8]. Nevertheless, conventional microfluidic devices have limitations that are often attributed to the materials used for fabrication [9]; they are usually made of a plastic elastomer (polydimethylsiloxane, PDMS) firmly bonded to a glass substrate, and cells are buried in chambers bounded by solid walls that prevent insertion of the standard experimental tools used by neurobiologists (e.g., cell scrapers, patch-clamping pipettes). Consequently, neurobiologists must employ alternative protocols to use them that are different from their familiar ones.

Recently, Walsh et al. (2017) introduced ‘fluid-walled microfluidics’; this overcomes some of these limitations by removing most solid boundaries [10]. It is a form of open microfluidics [11] that exploits properties of fluids at the microscale to confine aqueous environments using interfaces (i.e., fluid walls) between immiscible liquids (in this case, cell growth medium and a bio-inert fluorocarbon, FC40). Circuits can be built in minutes in standard Petri dishes, and – unlike solid walls that cannot be pierced by pipets – fluid walls allow direct access to cells everywhere in circuits. These walls re-heal automatically when pipets are withdrawn, they can be destroyed and/or reshaped without damaging cells within them [12,13], and are so transparent that cell morphology can be monitored using standard microscopes [14]. These features motivate the use of this technology here.

The cortex and striatum, together with the basal ganglia and thalamus, play an important role in regulating voluntary movement, learning, executive function, and emotion [15]. Cortical neurons (CNs) project axons toward the striatum where medium spiny neurons (MSNs) constitute up to 95% of striatal subtypes. Connectivity between CNs and MSNs is directional

and monosynaptic, whilst MSNs communicate with CNs indirectly via downstream circuits, particularly the basal ganglia [16]. This oriented arrangement of cortico-striatal projections is critical for their functioning but is often oversimplified by in-vitro co-cultures.

Studies of axonal outgrowth, axotomy, and subsequent regeneration have been facilitated by the use of compartmentalised chambers that allow separation of cell bodies from their axons [17,18]; such platforms can also allow pharmacological screening of factors acting specifically on distal axons [17,19]. In this study, we exploit the advantages of fluid walls to establish a proof-of-concept model that recreates appropriate arrangements of human CNs and MSNs. We then go on to develop a method for targeted and localised axotomy of CNs, and compare the effects of pro-regenerative conditions on axonal regrowth [19–21]; brain-derived neurotrophic factor (BDNF) and postsynaptic MSNs both have positive effects. In combination, these approaches provide a method for screening drugs promoting developmental outgrowth of axons and regeneration of damaged ones.

Results

Jet-printing of fluid-walled micro-circuits shaped like dumbbells

The fluid-walled environment is created in standard polystyrene Petri dishes (6 cm) by 'jet-printing' [22]. A thin layer of cell-culture medium is overlaid by an immiscible, bio-inert, and clear fluorocarbon, FC40 (Figure 1Ai). Next, a submerged jet of FC40 (Figure 1Aii) sweeps medium off the plastic substrate to leave FC40 locally pinned to the dish (Figure 1Aiii). The jetting nozzle (held by a 3-way traverse) now moves laterally above the substrate to draw the outline of the desired pattern which is held to the dish by interfacial forces acting between the two immiscible phases and the substrate. Here, we fabricate a 7x3 array of dumbbell-shaped circuits in each dish; each dumbbell comprises two square chambers (3 mm) connected by a thin conduit (~0.2 mm wide, 1 mm long, <10 μm high; Figure 1B).

Compared to conduits in conventional devices with solid walls – where access is limited to inputs and outputs (Figure 1Ci) – all parts of dumbbells are accessible through fluid ceilings (Figure Cii). Media and/or cells are added to, and removed from, chambers by lowering a

dispensing needle (also held by the traverse and connected to a syringe pump) through the FC40 until its tip is near the surface of the medium (i.e., 200 µm above the bottom of the dish). Existing walls/ceilings can also be destroyed and rebuilt (Figure 1Ciii), so circuits can be reconfigured during experiments [12]. Additionally, fluid walls are freely permeable to vital gases, so cells in these circuits are grown in conventional CO2 incubators. Finally, the refractive index of FC40 (1.29) almost matches that of water (1.33), and this permits undistorted imaging with standard microscopes [14].

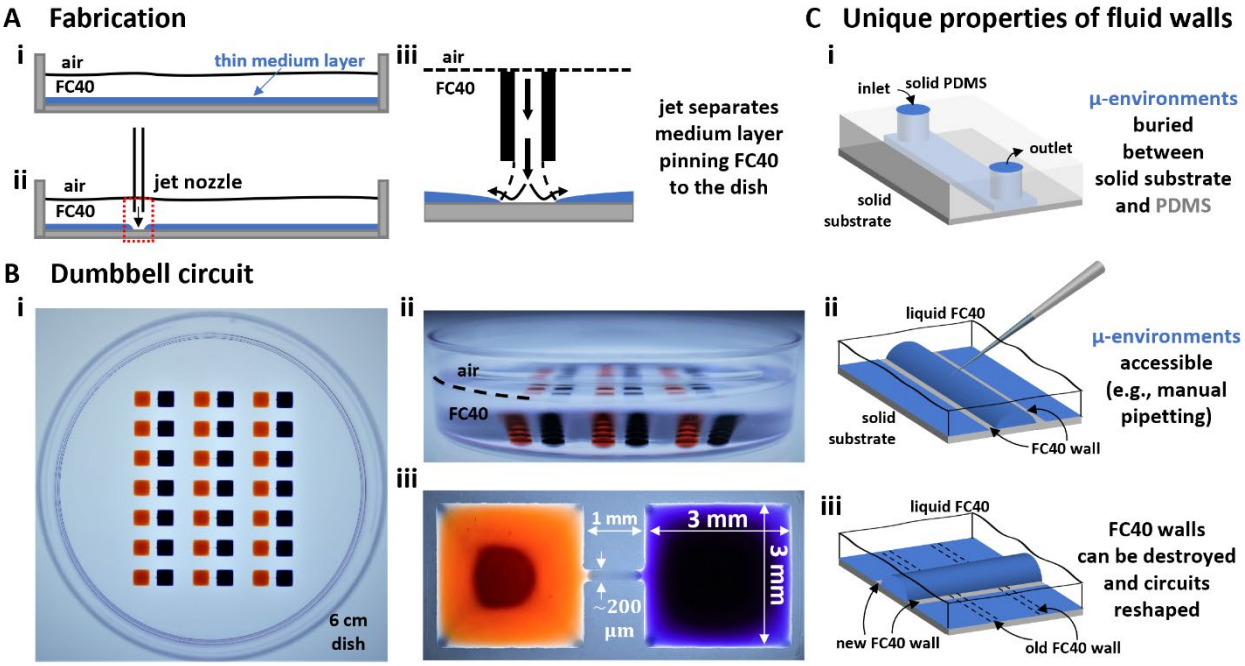

Figure 1. Fabrication and operation of fluid-walled circuits.

(A) Fabrication. (i) In a standard polystyrene Petri dish, a thin layer of cell-culture medium is overlaid by an immiscible, transparent, and bio-inert fluorocarbon (FC40). (ii) Additional FC40 is jetted (480 µl/min) through a nozzle mounted on a 3D-traverse. (iii) The submerged jet sweeps away medium, to leave fluid walls of FC40 pinned to the dish along the path of the traverse.

(B) Array of dumbbells after filling each with red and blue dyes. (i,ii) Top and side views of dish. (iii) Zoomed-in image of one dumbbell (conduit length = 1 mm).

(C) Comparing properties of solid PDMS walls used in conventional devices, with fluid ones.(i) Access to a conventional device is only through inlet and outlet ports. (ii) Medium can be pipetted into or out of any point in a fluid-walled circuit as liquid-liquid interfaces are easily pierced to re-heal automatically on withdrawal. (iii) Fluid walls can be destroyed at any time, and different ones recreated on demand

Local pressures in dumbbells

In all experiments, when cells are deposited in chambers, we require they remain there. This is impossible to achieve by rapid deposition into a newly-fabricated dumbbell, as this induces flow that carries them into the conduit (and perhaps into the other chamber). Therefore, we begin by describing how local pressures within dumbbells can be manipulated simply to ensure cells remain where plated.

First consider a 1 µl drop sitting in a dish filled with FC40; the drop is shaped like the cap of a sphere, as interfacial forces minimise the contact area of medium with the immiscible fluorocarbon. Then, the pressure (P) at the base of the drop is defined by the Laplace pressure across the medium:FC40 interface, plus the hydrostatic head of overlying medium and FC40. The Young-Laplace equation gives Laplace pressure, $LP = \gamma\left({}^{1}/_{R_1} + {}^{1}/_{R_2}\right)$, where γ is the interfacial tension, and R_1 and R_2 are two orthogonal radii describing the curvature of the liquid wall/ceiling. Assuming our chambers have circular footprints like the drop (so $R_1 = R_2 = R = {}^{a^2 + h^2}/_{2h}$, with a being the radius of the chamber footprint),

$$LP = \frac{4\gamma h}{a^2 + h^2} \tag{13}$$

The combined pressure, *P*, at the base of a chamber then includes the two hydrostatic heads, so

$$P = \frac{4\gamma h}{a^2 + h^2} + \rho_{med} g h + \rho_{FC40} g h_{FC40} \tag{14}$$

where ρ_{med} and ρ_{FC40} indicate density of medium and FC40 respectively, g is gravitational acceleration, h is drop height, and h_{FC40} the height of the overlay. However, when analysing the pressure difference between our two chambers (ΔP), the contribution of h_{FC40} can be expressed as the height difference of the two chambers. Therefore:

$$\Delta P = 4\gamma\left(\frac{h_R}{a^2 + h_R^2} - \frac{h_L}{a^2 + h_L^2}\right) - (\rho_{FC40} - \rho_{med}) g (h_R - h_L) \tag{15}$$

where h_R and h_L indicate right and left chamber height, respectively. h_R and h_L represent the only variables in Eq. (15) as they depend on the volume (V) infused into each chamber, and

$$V = \frac{\pi h}{6}(3a^2 + h^2) \tag{16}$$

This means the pressure difference can be controlled simply by controlling chamber volume.

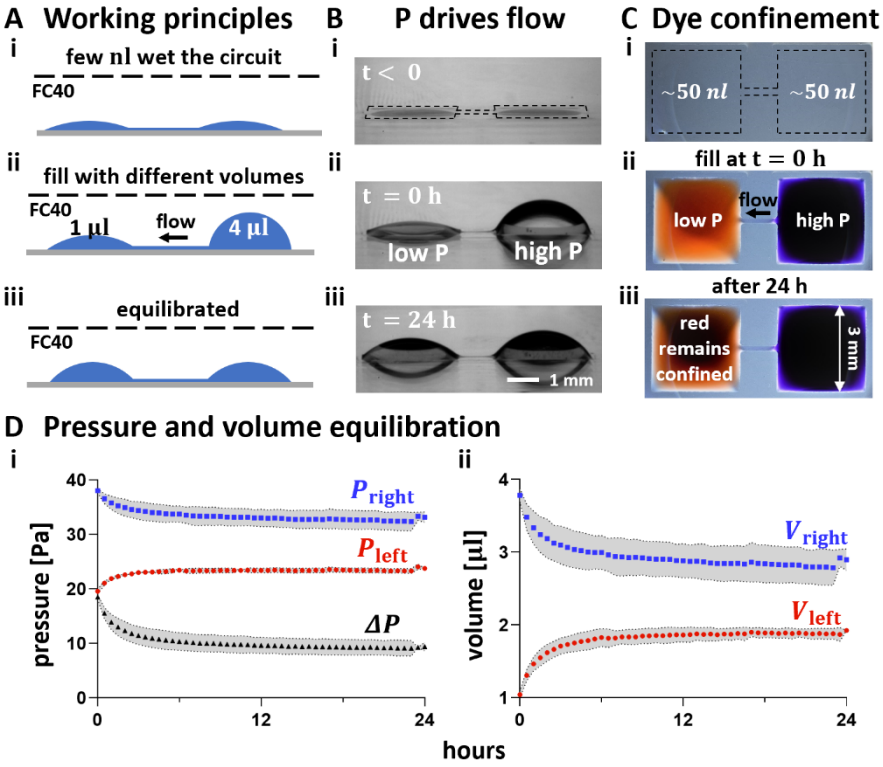

Figure 2. Ensuring liquid pipetted into the left of a dumbbell remains there. P = pressure.

(A) Principles. (i) A dumbbell is flow-free after fabrication. (ii) Medium (4 µl) is added to the right-hand chamber; this generates a high local Laplace pressure. When 1 µl is immediately added to the left-hand chamber (creating a lower local Laplace pressure), resulting left-ward flow through the conduit prevents any of the 1 µl from moving to the right. (iii) Eventually the system equilibrates, and flow ceases.

(B) Pressure difference drives flow. (i) Before filling. (ii) Immediately after filling with different volumes. (iii) After 24 h, chamber volumes have almost equalised due to leftward flow.

(C) After adding 4 µl blue dye to the right and 1 µl red dye to the left, no red dye flows rightward (top views). (i) Before adding dyes (dotted line marks dumbbell footprint). (ii) Immediately after adding dyes. (iii) After 24 h, red dye remains confined in its chamber (which now also contains blue dye).

(D) Changes in pressure (i) and volume (ii) of right- (blue) and left-hand (red) chambers determined after measuring chamber heights and calculating values using Eq. 1 (P_{right} and P_{left}) and Eq. 3, respectively. Black curve: pressure difference between chambers. Each dot represents the mean value of 3 technical replicates, and grey areas the associated standard deviations.

Ensuring cells remain where deposited

After fabrication, chamber volumes are minimal, walls/ceilings are almost flat (so Laplace pressures are almost negligible), local pressures throughout a dumbbell are roughly equal, and the system is in equilibrium (Figure 2Ai, 2Bi). Adding 4 µl into the right-hand chamber followed by 1 µl into the left-hand one generates a pressure difference that induces leftward flow through the conduit (Figure 2Aii, 2Bii). As time passes, the system equilibrates and volumes equalise (Figure 2Aiii, 2Biii). Similarly, after adding 4 µl blue dye into a right-hand chamber and 1 µl red dye into the left-hand one (Figure 2Ci,ii), red dye is confined to the left-hand-side for at least 24 h (Figure 2Ciii; note the conduit is filled with blue dye, and the left-hand chamber contains both dyes). Quantification of chamber pressures and volumes over time confirm that both converge towards equilibrium values, and that blue pressure is always greater than red pressure over 24 h (Figure 2D). This confirms that if the right-hand chamber is pre-filled with 4 µl before adding 1 µl to the left-hand one, there cannot ever be flow rightward. We use this approach to ensure that when cells are seeded in a selected chamber, they remain there.

When both chambers have equal volumes, their internal pressures are also equal – and so there is no flow in either direction. As a result, mass transport between chambers can only occur by diffusion to generate a concentration gradient in the conduit, with the steepness and duration of the gradient depending on dumbbell geometry and diffusion constant (see Supplementary Information). Supplementary Figure 1 and Supplementary Table 1 show how such a gradient of BDNF changes over time.

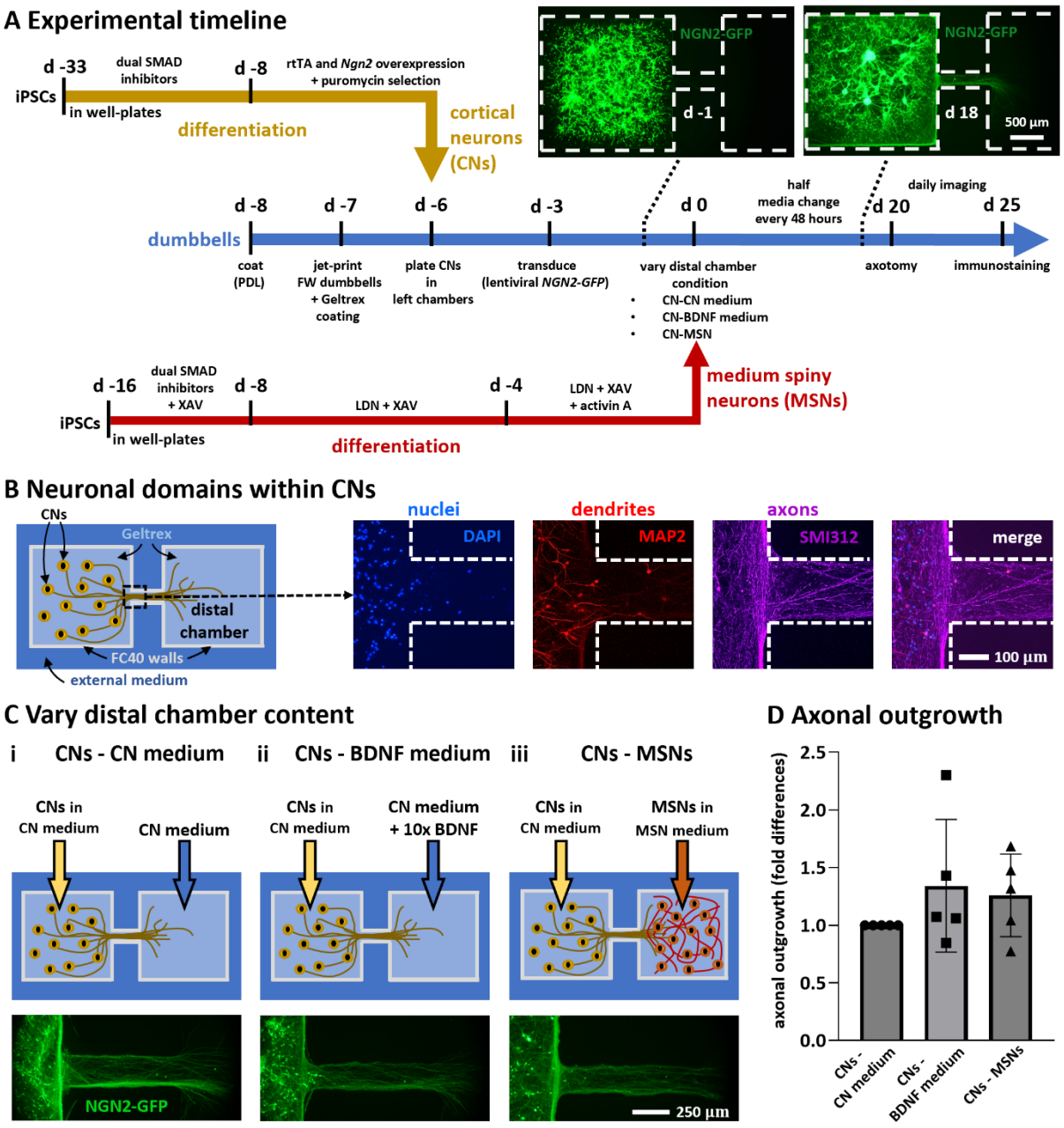

Figure 3. Timelines and culture conditions used to model and study unidirectional outgrowth of cortical neurons.

(A) Timelines. Yellow and red lines show protocols for generating CNs and striatal MSNs from iPSCs using standard methods; blue line describes those involved in making and operating fluid-walled dumbbells. Insets: after plating transduced CNs in left-hand chambers, live-cell images (collected on d -1 and 18) show NGN2-GFP fluorescence in parts of dumbbells (dotted white lines show circuit edges).

(B) Immunostaining shows compartmentalisation of neuronal domains in CNs (d 25). Cartoon: CNs in left-hand chamber, CN medium (but no MSNs) in distal one. Nuclei (DAPI) and MAP2-positive dendrites are confined within the chamber, while only SMI312-positive axons grow into the conduit (dotted white lines show circuit edges).

(C) Effects of varying distal-chamber content on axonal outgrowth. In all cases, CNs expressing NGN2-GFP are plated in CN medium in left-hand chambers. Top: cartoons indicating chamber contents.

Bottom: live-cell epifluorescence images of left end of conduit (d 20); axons extend into conduits in all three cases. (i) Monoculture control. (ii) Positive control with regenerative medium in distal chamber (CN medium + 10-fold higher concentration of 100 ng/ml BDNF. (iii) MSNs + MSN medium in distal chamber (this condition attempts to promote connectivity between cortex and striatum seen *in vivo*).
(D) Quantitative analysis of axonal outgrowth seen in (C). Outgrowth (fold difference) is difference in area covered by GFP-expressing neurites in conduits between d 0 and d 20, normalised for GFP-positive conduit area on d 0 as a function of the number of cells, and expressed relative to their control. Each dot represents a healthy control-derived line from one differentiation. N = 2 iPSC lines, n = 2-3 differentiations/line. One-way ANOVA with Bonferroni correction; $p > 0.05$.

Axons outgrow from CNs through the conduit to the distal chamber

Axon pathfinding is led by a variety of molecular cues, both intrinsic [23] and target-derived [24]. While roles of intrinsic factors have been investigated using dissociated cultures of neurons in vitro [21,25], less is known about target-derived signals due to difficulties in recreating the required micro-environments around neurons. Here, we develop a microfluidic model that recreates such an environment; we exploit the intrinsic physics of fluid-walled dumbbells (Figure 2), and establish a workflow (Supplementary Figure 2) that confines CNs in the left-hand chamber as axons grow through the conduit to the right-hand (distal) one.

Figure 3A provides an overview of the 3 major workflows that are now used. In one (yellow arrow), human iPSCs (induced pluripotent stem cells) are induced to differentiate into (post-mitotic) CNs using proven methods in standard well plates [26]. In a second (red arrow), human iPSCs are similarly induced to develop into post-mitotic MSNs, again using conventional methods [27,28]. In a third (blue arrow), fluid-walled dumbbells are jet-printed in 6 cm polystyrene Petri dishes, then CNs and MSNs plated into dumbbells.

In all experiments that will be described, CNs are deposited into left-hand chambers of dumbbells (using conditions established in Figure 2), and transduced 3 days later with lentiviruses encoding (tetracyclin-inducible) neurogenin-2-GFP (NGN2-GFP) to allow live-cell visualisation of transduced CNs. During subsequent culture (with CN medium in the right-hand chamber but no cells), axons (now expressing NGN2-GFP) grow through the conduit into the distal chamber (Figure 3A, insets; compare live-cell images on days -1 and 18). In some

cases, different media and/or MSNs are deposited on d 0 in the right-hand (distal) chamber. To ensure that deposited MSNs remain where deposited, we again exploit the approach described in Figure 2, except that now it is the left-hand chamber that is pre-filled with 4 µl before 1 µl of cell suspension is plated in the distal one.

As we wish to replicate the spatial organisation of CNs and MSNs in vivo, we require that CN somas remain confined to the left-hand chamber, and that only axons grow into the conduit. We confirm successful compartmentalisation by immunostaining (d 25) using domain-specific markers: DAPI-labelled nuclei and MAP2-positive dendrites are confined to the left-hand chamber, while the conduit is populated with SMI312-positive axons (Figure 3B).

We have seen that after plating in the left-hand chamber, post-mitotic CNs – with standard CN (maturation) medium in both chambers – start projecting axons into the conduit between d -6 to d 0. We now vary contents of the distal chamber at d 0 to see what effects concentration gradients of diffusing molecules along the conduit have on axonal outgrowth. This is tested in three different conditions. First, a control where CNs project axons towards distal CN medium – so there is no chemical gradient in the conduit (CNs-CN medium condition). A second condition where the distal chamber is filled with CN medium supplemented with 10x concentration (100 ng/ml) of BDNF (CNs-BDNF medium condition). Third, a more physiological condition where CNs extend their projections towards a population of MSNs (CNs-MSNs condition).

Axonal outgrowth in each of the 3 conditions is quantified as the difference of areas covered by GFP-expressing neurites in conduits measured at d 0 and d 20 ($\Delta A = A_{d20} - A_{d0}$). As ΔA may vary depending on the number of cells in each chamber making comparison between dumbbells biased, we divide it by A_{d0} to normalise results decoupling them from the effective count of CNs seeded. Additionally, to compare results from different batches of iPSCs differentiation, axonal outgrowths in the CNs-BDNF medium and CNs-MSNs conditions are expressed as the fold-difference of the CNs-CN medium control of the respective batch. Perhaps surprisingly, neither condition significantly increases axons outgrowth (Figure 3D; p

> 0.05, one-way ANOVA with Bonferroni correction) suggesting it occurs independently of BDNF exogenously supplied or MSN-derived molecules.

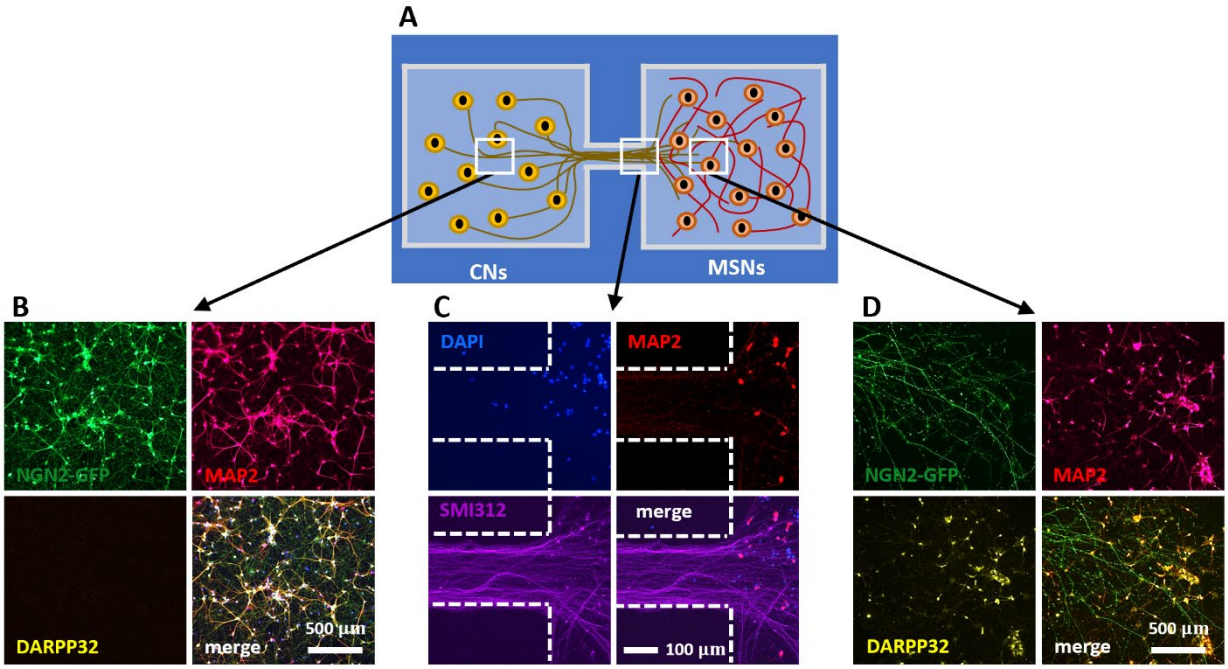

Figure 4. Modelling of unidirectional pathway between cortex and striatum.
Cortical axons marked with NGN2-GFP grow from the left chamber through the conduit into the distal chamber containing MSNs. (DAPI – blue – nuclei, MAP2 – red – dendrites, SMI312 – purple – axons, NGN2-GFP – green – transduced CNs, DARPP32 – yellow – MSN marker; merges indicated).
(A) Top-view schematic of the cortex-striatum circuit in a fluid-walled dumbbell. CNs are seeded in the left chamber and cultured for 6 days, then MSNs are plated in the distal (right) chamber. White boxes indicate areas imaged below using various markers.
(B) MAP2-positive dendrites and NGN2-GFP are found throughout the CN chamber (but not DARPP32-expressing MSNs).
(C) MSNs nuclei remain where seeded and develop MAP2-positive dendrites; they are joined by SMI312-positive CN axons from the left-hand chamber.
(D) Axons containing NGN2-GFP from transduced CNs are intertwined amongst MAP2- and DARPP32-positive neurons in the striatal chamber

A unidirectional circuit between cortex and striatum

The CNs – MSNs condition described above provides an *in-vitro* model for possible connectivity between cortex and striatum. This prompted a more detailed immunolabelling analysis on d 25 (Figure 4). Note here that NGN2-GFP (now detected using an anti-GFP

antibody) is a CN-specific marker, and DARPP32 is a MSN-specific one; MAP2 and SMI312 mark respectively dendrites and axons in both cell types. As expected, CNs the left-hand chamber express NGN2-GFP plus MAP2, but no (striatal-specific) DARPP32 (Figure 4A,B). The right-hand end of the conduit contains no nuclei stained with DAPI (confirming somas remain where plated), but does contain many SMI312-positive axons that appear to invade the distal chamber with its MAP2-positive dendrites (Figure 4C). The distal chamber is populated by many (CN-derived) NGN2-GFP-positive axons that ramify amongst MSNs expressing (striatal-specific) DARPP32 plus MAP2. These results are consistent with no spill-over of somas from either chamber, and unidirectional growth of CN axons into the distal chamber where they ramify amongst MSNs.

Axotomy using a micro-jet

We next use a micro-jet to sever axons projecting from CNs through a conduit into an empty distal chamber. The process involves three steps. First, fluid walls are destroyed by removing (manually by pipet) the FC40 overlay, and adding ~5 ml medium to the dish; CNs and axons remain attached to the substrate (Figure 5Ai). Second, a submerged jet of medium (emitted from the same nozzle used for FC40 jet-printing) is moved perpendicularly by the traverse across the axons to sever them (Figure 5Aii). Third, new fluid walls are built just outside the original ones to recreate a slightly larger dumbbell (Figure 5Aiii). To do so, most medium is gently removed to leave a thin layer, fresh FC40 is overlaid, and a new dumbbell jet-printed around the original one so that the FC40 stream does not impinge on existing attached cells or axons (Supplementary Figure 2C). This technique allows targeted axotomy of a chosen segment within an axon (Figure 5Aiv). Moderate-throughput axotomy in each of the 21 original dumbbells in one dish is achieved in <90 sec (Figure 5Av). Comparison of live-cell images of cortical axons expressing NGN2-GFP taken before and after axotomy reveal how local damage is, with the jet clearing the axotomized area of most cellular material (Figure 5Bi,ii).

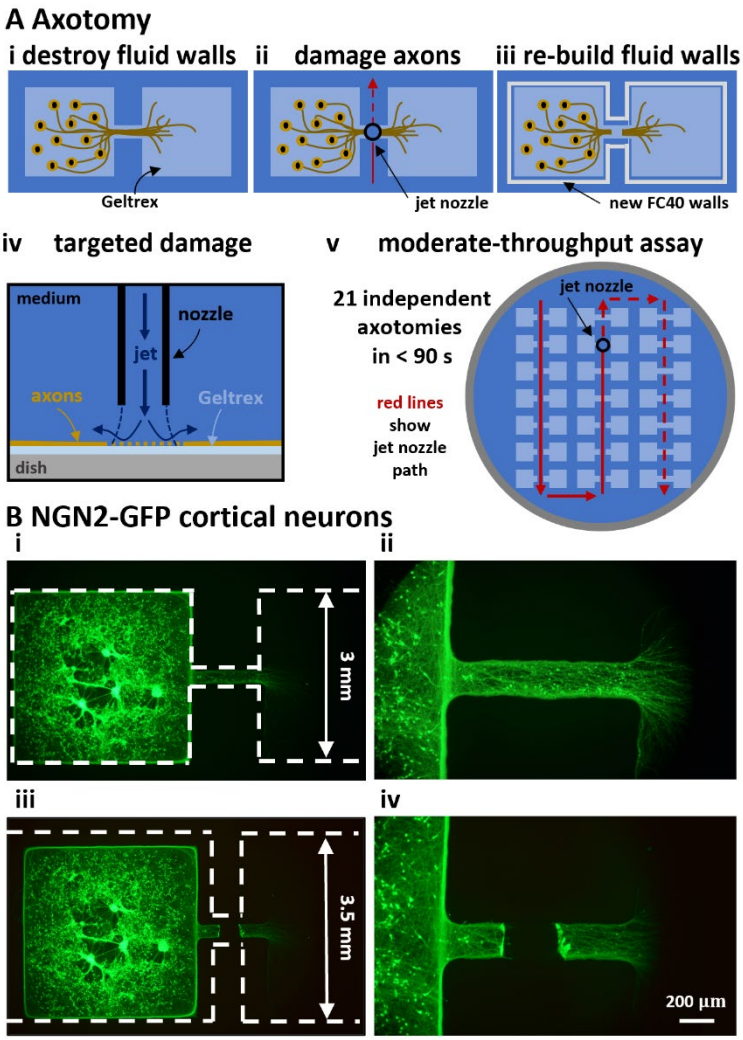

Figure 5. Axotomy assay on fluid-walled microfluidics

(A) Schematics illustrating localized axotomy. (i) Fluid walls are destroyed; cells remain attached to Geltrex within the dumbbell footprint. (ii) The traverse moves a nozzle that jets medium onto axons and cuts them. (iii) New fluid walls are jet-printed (using an FC40 jet) to form a new dumbbell slightly larger than the original ones; after filling the new dumbbell, axons regrow. (iv) Higher-magnification schematic of the submerged media jet in action targeting axons to generate localised damage. (v) Overview. Red lines illustrate the path followed by the medium jet nozzle while damaging 21 dumbbells (7x3 array) in a single 6 cm Petri dish in less than 90 seconds. Solid lines indicate the path already covered; dashed lines show future nozzle positions.

(B) Representative live-cell fluorescent images of CNs expressing NGN2-GFP pre- and post-axotomy. (i,ii) Dashed lines mark edges of dumbbell footprints before and after axotomy. (iii, iv) Higher magnification images taken before and after axotomy.

Regeneration after axotomy

After printing the new dumbbells around damaged cultures, the three conditions are re-established with equal volumes of the correct media in each respective chambers (Figure 6Ai), and then regeneration of axons is monitored for 5 more days (till d 25). Representative immunostaining on d 25 shows the axotomized area of the conduit refills with axons only expressing NGN2-GFP and SMI312, but not the dendrite-specific MAP2 (Supplementary Figure 3). As regrowth after axonal damage may involve target-derived signalling [29,30], we now compare effects of our three conditions on this regeneration (Figure 6Ai).

As for outgrowth, regeneration is quantified as the area covered by GFP-expressing neurites growing into a rectangular zone within the cleared area (Figure 6Aii; axon tracts that are incompletely severed or fully cleared are excluded from this analysis). This zone abuts the proximal damage line and has the same width of the original conduit (i.e., 200 µm) while extending 300 µm into the cleared area. Results are normalised against values seen prior to axotomy on d 20 to account for differences in axonal numbers and transduction efficiency. Results obtained with our two different iPSC lines from healthy donors (again with 2-3 differentiations per line) show that both BDNF and MSNs enhance regeneration to roughly the same degree compared to the control (Figure 6B). These results show that severed CN axons can regenerate, and that BDNF and MSNs enhance this.

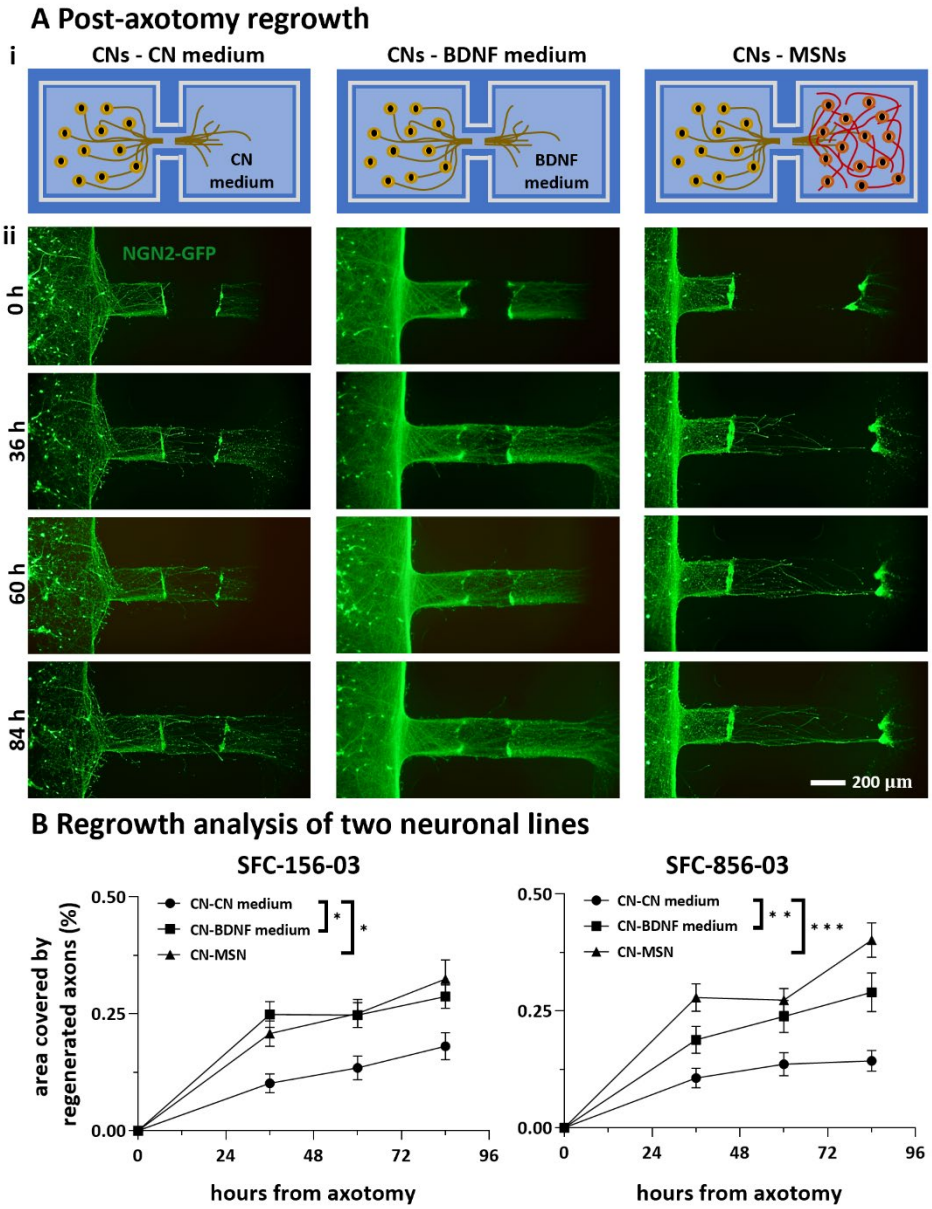

Figure 6: Effects of distant target-derived factors on regrowth of cortical axons after damage.

(A) Schematic and representative live-cell fluorescent images of CNs expressing NGN2-GFP taken 0-84 h after axotomy.

(B) Fraction of axotomized area re-covered by axons derived from two different healthy control iPSC lines (SFC-156-003, SFC- 856-03). N =2-3 differentiations per iPSC line, * $p < 0.05$, ** $p < 0.01$, *** $p < 0.001$, two-way ANOVA with Bonferroni correction test. (SFC156-03: CN-CN medium versus CN-BDNF medium, $p > 0.05$ at 36 and 60 hours, $p < 0.01$ at 84 hours; CN-CN medium versus CN-MSN, $p < 0.0001$ at 36 hours, $p < 0.001$ at 60 and 84 hours; SFC856-03: CN-CN medium versus CN-BDNF medium, $p < 0.001$ at 36 hours, $p < 0.05$ at 60 and 84 hours; CN-CN medium versus CN-MSN, $p < 0.01$ at 36 and 84 hours, $p < 0.05$ at 60 hours; two-way ANOVA with Bonferroni correction test). Furthermore, BDNF and MSNs exert comparable positive effect on cortical axonal regeneration (for both iPSC lines, CN-BDNF medium versus CN-MSN $p > 0.05$, two-way ANOVA with Bonferroni correction test).

Discussion

Our strategic goal is to develop microfluidic methods facilitating the production of, and experimentation on, neuronal circuits of any type in vitro; critically, we require that these methods should fit easily into bio-medical workflows. We describe proof-of-principle experiments illustrating individual steps towards this end. We begin by fabricating in minutes dumbbell-shaped micro-circuits in standard Petri dishes (6 cm; Figure 1), and develop conditions ensuring that cells plated in one or other chamber remain where deposited (Figure 2). Next, post-mitotic CNs derived from human iPSCs are now seeded in left-hand chambers of the dumbbell, so axons grow through connecting conduits of 1 mm to distal chambers (Figure 3A,B). Outgrowth of cortical axons is compared against three different targets in the distal chamber (Figure 3C,D); results show such outgrowth is not enhanced by BDNF. This result aligns with previous studies on mouse primary neurons [31] where high levels of BDNF did not boost normal distal growth. As the BDNF signalling pathway is usually conserved across species [32], we expected to see a similar response here. However, as far as we are aware, this is the first report on the influence of external diffusible factors on axonal outgrowth of human CNs in vitro, hence, modulation by BDNF as well as other neurotrophins will require further investigation. Interestingly, as also MSNs show no effect on normal healthy outgrowth, we hypothesise axonal outgrowth of post-mitotic iPSC-derived CNs to be independent of endogenous postsynaptic targets.

We then develop a circuit in which axons project from CNs in the left-hand chamber, through the conduit, and on to ramify amongst MSNs in the distal one (Figure 4). We anticipate such circuits will prove especially useful for studying cortical-striatal connectivity because they are so accessible to biologists. For example, an obvious next step is to examine electrical connectivity using patch clamping [33] and/or super-resolution calcium imaging [34]; our circuits can be built on glass surfaces and incorporated into both workflows without modification.

Similar to previous works [31,35], we also develop a moderate-throughput axotomy assay in which axons growing through conduits are severed by a fluid jet (Figure 5). In contrast to existing methods that use mechanical stresses [36,37], vacuum aspiration [19,38,39], toxins [40] for axotomy – all procedures that might be expected to yield poor reproducibility [41], we hope our (arguably non-contact) method will yield more consistent results. However, in our assay, the quality of the axotomy depends on cells density and age as these parameters affect the thickness of the axonal bundle; 'cut' parameters like jet flow rate, nozzle height above the dish, and traverse speed are finely tuned to achieve the desired result. Using this assay, we show that BDNF or MSNs in distal chambers promote axon regrowth (Figure 6). Here, the heightened demand for BDNF following axon injury [42] might explain the observed positive effect on axonal regeneration despite the neutral effect shown on axonal outgrowth.

In conclusion, we have recreated a basic micro-circuit containing human neurons that mimics the unidirectional connectivity seen between cortex and striatum in vivo, as well as developing a moderate-throughput axotomy assay. Our approaches benefit from the intrinsic advantages provided by fluid walls that include ease of circuit fabrication and operation, plus compatibility with existing bio-medical workflows. As additional conduits and chambers can be easily added, we anticipate these approaches will expand the experimental toolkit available for the study of human neuronal networks in health and disease.

Materials and methods

Fluorocarbon 40 (FC40)

FC40 was purchased from 3M. FC40^{STAR} (iotaSciences Ltd, Oxfordshire, UK) is a compound treated with a proprietary method to improve formation of fluid walls. Throughout the article, the term 'FC40' is used to refer to FC40^{STAR}.

The fluid printer

The printer (iotaSciences Ltd, Oxfordshire, UK) consists of 3D traverse with two printing heads (two blunt needles of different internal diameters) plus a built-in software. Each needle is connected to a syringe pump through Teflon tubes. One needle (70 μm internal diameter) is attached to a syringe containing FC40 and it is used for jet-printing; this is the jetting needle. The other needle (255 μm internal diameter) is attached to a syringe normally with ethanol to guarantee sterility as this needle is used to handle samples; this is the dispensing needle. Needles can be moved above the surface of a Petri dish as pumps infuse liquids.

In our design, 21 dumbbells are printed in each dish by the jetting needle on d -7. Thereafter, every volume infusion/removal from chamber is operated by the dispensing needle. Every operation on one chamber of dumbbells (either left or right), is repeated to all dumbbells in the dish before starting any task on the opposite chamber.

Generation of iPSC-derived post-mitotic cortical neurons

This is the yellow pathway in Figure 3. Generation of CNs from two iPSC control lines from healthy human patients (EBiSC409 Cat# STBCi101-A, RRID:CVCL_RD71), and SFC856-03-04 (RRID:CVCL_RC81) is adapted from an established protocol [26]. In brief, neuronal development is induced with dual SMAD inhibitors 10 μM SB431542 (Tocris) and 118 nM LDN (Sigma) for 25 days (d -33 to d -8). These progenitors (d -8) are now transduced with lentiviruses that encode a doxycylin-inducible tetO promoter driving constitutive expression of rtTA and mouse neurogenin-2 (Ngn2) [43]. A puromycin resistance gene is also co-expressed to select for cells expressing Ngn2. (See Data Availability for more information about this differentiation protocol).

Generation of iPSC-derived post-mitotic medium spiny neurons

This is the red pathway in Figure 3. Two iPSC control lines (SFC156-03-01 and SFC856-03-04) are differentiated into MSNs using conditions modified from established protocols [27,28].

In brief, neural induction of sub-pallial identity is initiated by dual SMAD inhibitors – 10 μM SB431542 (Tocris) and 118 nM LDN (Sigma) – and inhibition of WNT signalling – 4 μM XAV (Tocris) – from d -16 to d -8. From d -8 to d 0, SB431542 is removed and neurogenesis in the culture is mediated by LDN and XAV. Activin A (25 μg/ml; SKU# SRP3003), the key regulator of TGF-β signalling, is added from d -4 to d 0. (see Data Availability for more information about this differentiation protocol).

Fabrication of dumbbells

This is the blue pathway in Figure 3 from d -8 to d -6. On d -8, 6 cm Petri dishes are pre-coated with 7 ml of poly-D-lysine (0.01 mg/ml) overnight. On d -7, dishes are washed twice with PBS and subsequently loaded with Neurobasal medium (1 ml; ThermoFisher) supplemented with 1x B27 (ThermoFisher). After at least 5 minutes, medium is manually removed to leave a thin layer (~50 μl) attached to the bottom of the dish, and FC40 (~2 ml) gently pipetted on to this thin layer. An array of 7x3 dumbbells is now jet-printed using a fluid printer (iotaSciences Ltd.) (Soitu et al., 2020). When used with cells, dumbbell chambers are each loaded with 2 μl Geltrex™ (0.46 mg/ml; ThermoFisher) and incubated at 37ºC overnight (to d -6).

Maturation media used for culturing in dumbbells

Cortical maturation medium (CN medium) used from d -6 to d 25 and beyond: Neurobasal, 1X B27 with vitamin A, 1X Glutamax, penicillin/streptomycin (50 U or mg per ml) (1:200), 1 mg/ml doxycycline (1:1000), 10 ng/ml BDNF, 10 ng/ml NT-3 (1:1000), 200 ng/ml laminin (1:5000), 200 mM ascorbic acid (1:1000). This corresponds to Ngn2 base medium from protocol dx.doi.org/10.17504/protocols.io.bp2l69qr5lqe/v1.

Cortical maturation medium + 10x BDNF (BDNF medium) used from d 0 to d 25 and beyond: CN medium with 100 ng/ml BDNF.

Striatal maturation medium (MSN medium) used from d 0 to d 8: DMEM/F12 basal medium, 1% MEM Non-Essential Amino Acids (NEAA), 1% L-glutamine, 1x B27 without vitamin A, 1%

penicillin/streptomycin (P/S), 0.05% β-mercaptoethanol. This corresponds to striatal maturation medium 1 from protocol dx.doi.org/10.17504/protocols.io.eq2ly79prlx9/v1.

Striatal maturation medium (MSN medium) used from d 8 to d 25: 50% DMEM/F12 basal medium, 50% Neurobasal, 1% MEM Non-Essential Amino Acids (NEAA), 1% L-glutamine, 1x B27 plus vitamin A, 1% penicillin/streptomycin (P/S), 0.05% β-mercaptoethanol. This corresponds to striatal maturation medium 2 from protocol dx.doi.org/10.17504/protocols.io.eq2ly79prlx9/v1.

Plating CNs in left-hand chambers and transduction.

This is the blue pathway from d -6 to d 0. On day -6, 2 µl is removed from each chamber, 4 µl cortical-maturation media deposited in the right-hand chamber (to create a positive pressure gradient toward the left chamber), and post-mitotic CNs plated (1 µl containing 13,000 cells in cortical maturation medium) in each left-hand chamber. On day -3, CNs are transduced by adding 2 µl lentivirus encoded *NGN2-GFP* in cortical maturation medium (50 µl of viral stock/2 µl) to the left-hand chamber, and 1 µl fresh medium without lentiviruses to the right-hand one (to give ~4 µl/chamber). On d -2, 4 µl is removed from each chamber and 4 µl fresh medium added back (to wash away free lentivirus).

Varying conditions on d 0

On d 0, both chambers initially contain ~4 µl cortical maturation medium, with CNs in the left-hand one. Now, contents of the distal chamber are varied to give the 3 conditions (CNs-CN medium, CNs-BDNF medium, and CNs-MSNs). For all conditions, 4 µl is removed from both chambers, and 4 µl CN medium added to the left-hand chamber. Next, 1 µl of either CN medium, or CN medium plus 100 ng/ml BDNF, or a MSNs suspension (13,000 cells in MSN medium). As before, a pressure difference confines MSNs and BDNF to right-hand chambers.

Culturing CNs in dumbbells without MSNs after d 0

This is the blue pathway from d 0 to d 25 and beyond for the CNs-CN medium and CNs-BDNF medium conditions. On d 2, both chambers were completely emptied (removing ~4 µl from each chamber). Then, 4 µl CN medium is added to the CN chamber and 4 µl of either CN or BDNF medium to the distal one (to give 4 µl/chamber). Every 48 h thereafter, half the specified medium present in a chamber is replenished by removing 2 µl spent medium and then adding back 2 µl fresh medium of the same kind.

Culturing CNs in dumbbells with MSNs after d 0

This is the blue pathway from d 0 to d 25 and beyond for the CNs-MSNs condition. On d 2, both chambers are completely emptied (removing ~4 µl from each chamber). Then, 4 µl of fresh CN medium is added to CN chamber and 4 µl of MSN medium containing 200 nM cytosine arabinoside (araC) to arrest proliferation of any non-neuronal cells in the population to the distal one (to give 4 µl/chamber). Every 48 h thereafter, half the medium in each chamber is changed by withdrawing 2 µl and adding an equal volume of fresh medium; this gradually dilutes araC over MSNs. On d 8, a full medium change is done to switch MSNs to a new MSN medium (see Maturation media used for culturing in dumbbells).

Axotomy

Fluid walls are destroyed by gently pouring all FC40 out of the dish followed by two washes with cortical maturation medium (care is taken to prevent cell/axon peeling). Directed axotomy is performed automatically using the fluid printer by modifying an existing procedure [44]. A 1 ml glass syringe (Hamilton) filled with Neurobasal medium (Thermofisher) is connected via Teflon tubes to the jetting nozzle. Then, a medium jet is ejected (480 µl/min) from the nozzle (70 µm inner diameter) held 0.3 mm above the dish as the traverse moves (960 mm/min) the nozzle in a straight line perpendicular to the axons' main direction of outgrowth (Figure 4B). Following axotomy, dishes were re-filled with fresh FC40, and new fluid walls jet-printed

around the original footprint. The new dumbbells have larger footprints (chamber area = 3.5x3.5 mm^2, conduit length = 0.5 mm, width ~400 µm) to avoid damaging attached cells/axons. 4 µl fresh cell medium is deposited into each chamber.

Figure 6 summarises data obtained from 2-3 differentiations per cell line, and measurements from 100-150 dumbbells/differentiation. Another ~30% dumbbells are discarded due to incomplete severing or clearing of axons in the axotomised area of the conduit, and/or incomplete rebuilding of new dumbbells (which results in media leakage). [Fluid walls are almost always built successfully on virgin Petri dishes, but success rates are lower when building on dishes that have been covered with a thin skim of medium overlaid with FC40 from d -7 to d 20.]

Imaging

All fluorescent live-cell images of dumbbells are taken with a digital single-lens reflex camera (Nikon D7100 DSLR) connected to an epifluorescence microscope (Olympus IX53). Images are analysed using Cell Profiler 3.8 (RRID: SCR_007358) to describe and quantify axon outgrowth and regrowth.

Immunostaining

All FC40 is discarded from the dish, cultures washed twice with PBS, fixed (2% paraformaldehyde, 20 mins at room temperature, RT), and washed three times with PBS. Fixed samples are now incubated (80ºC, 5 min) in citrate buffer pH 6.0 (ThermoFisher), and left for 10 mins at RT. Permeabilization and blocking are performed concurrently in PBS, 10% donkey serum, and 0.01% Triton X-100 for 10 mins. Following incubation with primary antibody in PBS and 10% donkey serum overnight at 4°C, samples are washed with PBS, and incubated in species-appropriate Alexa Fluor© secondary antibody in PBS with 10% donkey serum for 1 hour at RT. Supplementary Table 1 list antibodies used. Images are acquired on

an Invitrogen EVOS ™ FL Auto (ThermoFisher) cell-imaging system, and processed using ImageJ (RRID:SCR_003070) [45].

Measuring pressures and volumes in chambers

Dumbbells are printed in wide rectangular plates (Thermo Scientific™ Nunc™ Rectangular Dishes single well) to improve imaging from the side, as the curved plastic walls of 6 cm dishes distort views. Chambers are jet-printed as before after filling a dish with ~5 ml DMEM + 10% FBS, removing all but a thin film, and overlaying ~10 ml FC40. Using a fluid printer modified to host rectangular dishes (Hylewicz CNC-Technik). The same medium is infused into chambers by a syringe pump (PhD Ultra, Harvard Apparatus) equipped with a 50 µl glass syringe (Hamilton) connected to a blunt metal needle (33G blunt NanoFil™ needle, World Precision Instruments) through a Teflon tube (Zeus Company Inc.) to generate the desired initial volume/pressure difference. Volumes are dispensed following the same sequence used during experiments with neurons. Thus, 4 µl are initially infused in the right-hand chamber, followed by 1 µl into the left-hand one. Images of the two chambers equilibrating are recorded from the side every 30 min for 24 h using a camera (First Ten Angstrom) placed perpendicular to the connecting conduit (Figure 2B). Chambers heights are measured using FTA32 software (First Ten Angstrom) and the outer diameter of the dispensing needle (210 µm) as a scale reference. Heights are converted into pressures and volumes (Figure 2D) using equation 1 and equation 2, respectively.

Statistical analysis

All data are presented as mean ± standard error of the mean (SEM) unless otherwise stated. Raw data are tested for normality and statistical comparison of the means is performed using one- or two-way ANOVA with Bonferroni post-hoc test; a difference is considered significant if $p < 0.05$. All statistical analyses are performed on GraphPad Prism 6.0 (GraphPad Software, RRID:SCR_002798).

Data Availability. The data that support the findings of this study are deposited on Zenodo (DOI doi.org/10.5281/zenodo.7924431). All details of the antibodies, cell lines, and software used in this work are available on Zenodo (DOI doi.org/10.5281/zenodo.7924431). Protocols associated with this work can be found on protocols.io (DOI dx.doi.org/10.17504/protocols.io.36wgqjwwxvk5/v1). The custom G-Code scripts used in this study to jet-print the microfluid-walled dumbbells are available at https://github.com/craggASAP/microfluid_axotomy.git.

Author Contributions. F.N. and Q.D. conceived the project. F.N. and Q.D. designed, performed, and analysed all experimental data. P.R.C, E.W., and R.W.M supervised the study. F.N. and Q.D. prepared the first draft of the manuscript. All authors reviewed the manuscript and approved its submission.

Acknowledgements. This work was supported by iotaSciences Ltd and the Engineering and Physical Sciences Research Council through EP/R513295/1 (who both provide financial support to F.N.). Q.D. was supported by a National Science Scholarship from Agency for Science, Technology and Research in Singapore. This research was funded in part by Aligning Science Across Parkinson's [ASAP-020370] through the Michael J. Fox Foundation for Parkinson's Research (MJFF) and in part by the Monument Trust Discovery Award from Parkinson's UK (J-1403). The work was supported by a National Institute for Health Research-Medical Research Council Dementias Platform UK Equipment Award (MR/M024962/1) to R.W.M. For the purpose of open access, the author has applied a CC BY public copyright license to all Author Accepted Manuscripts arising from this submission. We thank Ajantha Abbey for his generous donation of cortical neuron media.

Competing interests. P.R.C and E.J.W. co-founded, and hold equity in, IotaSciences Ltd. The same company provides financial support to F.N

References

[1] Iannielli A, Ugolini GS, Cordiglieri C, Bido S, Rubio A, Colasante G, et al. Reconstitution of the Human Nigro-striatal Pathway on-a-Chip Reveals OPA1-Dependent Mitochondrial Defects and Loss of Dopaminergic Synapses. Cell Rep 2019;29:4646-4656.e4.

[2] Virlogeux A, Moutaux E, Christaller W, Genoux A, Bruyere J, Fino E, et al. Reconstituting Corticostriatal Network on-a-Chip Reveals the Contribution of the Presynaptic Compartment to Huntington's Disease. Cell Rep 2018;22:110–22.

[3] Miura Y, Li M-Y, Birey F, Ikeda K, Revah O, Thete MV, et al. Generation of human striatal organoids and cortico-striatal assembloids from human pluripotent stem cells. Nat Biotechnol 2020;38:1421–30.

[4] Taylor AM, Dieterich DC, Ito HT, Kim SA, Schuman EM. Microfluidic Local Perfusion Chambers for the Visualization and Manipulation of Synapses. Neuron 2010;66:57–68.

[5] Luo X, Chen J-Y, Ataei M, Lee A. Microfluidic Compartmentalization Platforms for Single Cell Analysis. Biosensors (Basel) 2022;12.

[6] Liu S, Li Y, Shang L, Yin J, Qian Z, Chen C, et al. Size-dependent neurotoxicity of micro- and nanoplastics in flowing condition based on an in vitro microfluidic study. Chemosphere 2022;303:135280.

[7] Ionescu-Zanetti C, Shaw RM, Seo J, Jan Y-N, Jan LY, Lee LP. Mammalian electrophysiology on a microfluidic platform. Proc Natl Acad Sci U S A 2005;102:9112–7.

[8] Peyrin J-M, Deleglise B, Saias L, Vignes M, Gougis P, Magnifico S, et al. Axon diodes for the reconstruction of oriented neuronal networks in microfluidic chambers. Lab Chip 2011;11:3663–73.

[9] Berthier E, Young EWK, Beebe D. Engineers are from PDMS-land, Biologists are from Polystyrenia. Lab Chip 2012;12:1224–37.

[10] Walsh EJ, Feuerborn A, Wheeler JHR, Tan AN, Durham WM, Foster KR, et al. Microfluidics with fluid walls. Nat Commun 2017;8:816.

[11] Zhang Q, Feng S, Lin L, Mao S, Lin JM. Emerging open microfluidics for cell manipulation. Chemical Society Reviews 2021;50:5333-5348

[12] Soitu C, Feuerborn A, Deroy C, Castrejón-Pita AA, Cook PR, Walsh EJ. Raising fluid walls around living cells. Sci Adv 2019;5:eaav8002.

[13] Deroy C, Rumianek AN, Wheeler JHR, Nebuloni F, Cook PR, Greaves DR, et al. Assaying Macrophage Chemotaxis Using Fluid-Walled Microfluidics. Adv Mater Technol 2022;7:2200279.

[14] Soitu C, Deroy C, Castrejón-Pita AA, Cook PR, Walsh EJ. Using Fluid Walls for Single-Cell Cloning Provides Assurance in Monoclonality. SLAS Technol 2020;25:267–75.

[15] Pennartz CMA, Berke JD, Graybiel AM, Ito R, Lansink CS, van der Meer M, et al. Corticostriatal Interactions during Learning, Memory Processing, and Decision Making. J Neurosci 2009;29:12831–8.

[16] Shepherd GMG. Corticostriatal connectivity and its role in disease. Nat Rev Neurosci 2013;14:278–91.

[17] Bengoa-Vergniory N, Faggiani E, Ramos-Gonzalez P, Kirkiz E, Connor-Robson N, Brown L V, et al.

CLR01 protects dopaminergic neurons in vitro and in mouse models of Parkinson's disease. Nat Commun 2020;11:4885.

[18] Neto E, Leitão L, Sousa DM, Alves CJ, Alencastre IS, Aguiar P, et al. Compartmentalized Microfluidic Platforms: The Unrivaled Breakthrough of In Vitro Tools for Neurobiological Research. J Neurosci 2016;36:11573–84.

[19] Taylor A, Blurton-Jones M, Rhee S, DH Cribbs D. A microfluidic culture platform for CNS axonal injury, regeneration and transport. Nat Methods 2005;2:599–605.

[20] Hofmann M, Biller L, Michel U, Bähr M, Koch JC. Cytoskeletal assembly in axonal outgrowth and regeneration analyzed on the nanoscale. Sci Rep 2022;12:14387.

[21] Melamed Z, López-Erauskin J, Baughn MW, Zhang O, Drenner K, Sun Y, et al. Premature polyadenylation-mediated loss of stathmin-2 is a hallmark of TDP-43-dependent neurodegeneration. Nat Neurosci 2019;22:180–90.

[22] Soitu C, Stovall-Kurtz N, Deroy C, Castrejón-Pita AA, Cook PR, Walsh EJ. Jet-Printing Microfluidic Devices on Demand. Advanced Science 2020;7:2001854.

[23] Yu TW, Bargmann CI. Dynamic regulation of axon guidance. Nat Neurosci 2001;4 Suppl:1169–76.

[24] Davis GW. The making of a synapse: target-derived signals and presynaptic differentiation. Neuron 2000;26:551–4.

[25] Klim JR, Williams LA, Limone F, Guerra San Juan I, Davis-Dusenbery BN, Mordes DA, et al. ALS-implicated protein TDP-43 sustains levels of STMN2, a mediator of motor neuron growth and repair. Nat Neurosci 2019;22:167–79.

[26] Hedegaard A, Monzón-Sandoval J, Newey SE, Whiteley ES, Webber C, Akerman CJ. Pro-maturational Effects of Human iPSC-Derived Cortical Astrocytes upon iPSC-Derived Cortical Neurons. Stem Cell Reports 2020;15:38–51.

[27] Arber C, Precious S V, Cambray S, Risner-Janiczek JR, Kelly C, Noakes Z, et al. Activin A directs striatal projection neuron differentiation of human pluripotent stem cells. Development 2015;142:1375–86.

[28] Telezhkin V, Schnell C, Yarova P, Yung S, Cope E, Hughes A, et al. Forced cell cycle exit and modulation of GABAA, CREB, and GSK3beta signaling promote functional maturation of induced pluripotent stem cell-derived neurons. Am J Physiol Cell Physiol 2016;310:C520-41.

[29] Fawcett JW. The Struggle to Make CNS Axons Regenerate: Why Has It Been so Difficult? Neurochem Res 2020;45:144–58.

[30] Mahar M, Cavalli V. Intrinsic mechanisms of neuronal axon regeneration. Nat Rev Neurosci 2018;19:323–37.

[31] Kimpinski K, Campenot RB, Mearow K. Effects of the neurotrophins nerve growth factor, neurotrophin-3, and brain-derived neurotrophic factor (BDNF) on neurite growth from adult sensory neurons in. J Neurobiol 1997;33:395–410.

[32] Mahar M, Cavalli V. Intrinsic mechanisms of neuronal axon regeneration. Nat Rev Neurosci 2018;19:323–37.

[33] Do QB, Ng B, Marquez Gomez R, Beccano-Kelly D, Ibarra-5 Aizpura N, Caiazza M-C, et al. Early striatal hyperexcitability in an in vitro human striatal microcircuit model carrying the Parkinson's GBA-N370S mutation. bioRxiv 2023-03

[34] Buetfering C, Zhang Z, Pitsiani M, Smallridge J. Behaviorally relevant decision coding in primary somatosensory cortex neurons. Nat Neurosci 2022;25:1225–36.

[35] Bertrand J, Winton MJ, Rodriguez-Hernandez N, Campenot RB, Mckerracher L. Application of Rho antagonist to neuronal cell bodies promotes neurite growth in compartmented cultures and regeneration of retinal ganglion cell axons in the optic. Journal of Neuroscience 2005;25:1113–21.

[36] Fournier AJ, Rajbhandari L, Shrestha S, Venkatesan A, Ramesh KT. In vitro and in situ visualization of cytoskeletal deformation under load: traumatic axonal injury. The FASEB Journal 2014;28:5277–87.

[37] Yap Y, Dickson T, King A, MC Breadmore M. Microfluidic culture platform for studying neuronal response to mild to very mild axonal stretch injury. Biomicrofluidics 2014;8.

[38] Jocher G, Mannschatz SH, Offterdinger M, Schweigreiter R. Microfluidics of small-population neurons allows for a precise quantification of the peripheral axonal growth state. Front Cell Neurosci 2018;12:166.

[39] Nagendran T, Taylor AM. Unique Axon-to-Soma Signaling Pathways Mediate Dendritic Spine Loss and Hyper-Excitability Post-axotomy. Front Cell Neurosci 2019;13:431.

[40] Li L, Ren L, Liu W, Wang JC, Wang Y, Tu Q, et al. Spatiotemporally controlled and multifactor involved assay of neuronal compartment regeneration after chemical injury in an integrated microfluidics. Anal Chem 2012;84:6444–53.

[41] Varier P, Raju G, Madhusudanan P, Jerard C, Shankarappa SA. A Brief Review of In Vitro Models for Injury and Regeneration in the Peripheral Nervous System. Int J Mol Sci 2022;23.

[42] Funakoshi H, Frisén J, Barbany G, Timmusk T, Zachrisson O, Verge VM, et al. Differential expression of mRNAs for neurotrophins and their receptors after axotomy of the sciatic nerve. J Cell Biol 1993;123:455–65.

[43] Zhang Y, Pak C, Han Y, Ahlenius H, Zhang Z, Chanda S, et al. Rapid single-step induction of functional neurons from human pluripotent stem cells. Neuron 2013;78:785–98.

[44] Soitu C, Panea M, Castrejón-Pita AA, Cook PR, Walsh EJ. Creating wounds in cell monolayers using micro-jets. Biomicrofluidics 2021;15:14108.

[45] Schindelin J, Arganda-Carreras I, Frise E, Kaynig V, Longair M, Pietzsch T, et al. Fiji: an open-source platform for biological-image analysis. Nat Methods 2012;9:676–82.

[46] Crank J. The Mathematics of Diffusion. Clarendon Press; 1979.

[47] Stroh M, Zipfel WR, Williams RM, Webb WW, Saltzman WM. Diffusion of nerve growth factor in rat striatum as determined by multiphoton microscopy. Biophys J 2003;85:581–8.

Supplementary Information

Determination of concentration gradients in dumbbells

Consider the dumbbell in Supplementary Figure 1, where chambers are filled with equal volumes, and transport of molecules through the conduit is driven only by diffusion to generate a concentration gradient from right to left. Prediction of those gradients represents a crucial step in understanding the roles of target-derived signals like BDNF or other MSN-derived factors. Using Fick's 2nd law, concentration (c(x,t)) in the conduit can be approximated by the solution to the one-dimensional diffusion equation for a semi-infinite medium with constant concentration at the boundary [46].

$$c(x,t) = C_0 erfc\left(\frac{x}{2\sqrt{Dt}}\right) \quad \text{(S1)}$$

with C_0 being the initial concentration in the right-hand chamber, D the diffusion coefficient, and x and t being space and time respectively. Equation S1 allows estimation of the time necessary for the gradient to reach steady state (t_{steady}), arbitrarily quantified as the time required for 30% of C_0 to reach the other end of the conduit ($x = L$), $t_{steady} = \frac{1}{D}\left(\frac{L}{2\, erfc^{-1}(0.3)}\right)^2$. The value of 30% is chosen so that the maximum error between the gradient profile (Eq. S1) and the linearized approximation is smaller than 10%. Once steady state is reached, the concentration gradient can be considered linear and remain stable for a time $t = t_{linear}$. Deriving from Fick's 1st law and defining it as the time needed for the concentration in the left chamber to increase by 5% of C_0, one gets:

$$t_{linear} = 1.05\frac{Lm_{mol}}{DA_cC_0} \quad \text{(S2)}$$

where m_{mol} is the mass of molecules transferred between chambers and A_c is the cross-sectional area of the connecting conduit. Unlike conduits with solid walls that have fixed cross sections, ones with fluid walls morph as pressures change. If conduit widths ($2a_c$) remain unchanged (as fluid walls are firmly pinned to the plastic substrate), heights (h_c) vary

depending on pressures applied. In particular, for a cross section like in Supplementary Figure 1B and assuming h_c << a_c at all times, one can prove:

$$A_c = \left(\frac{a_C}{2h_c}\right)\left[\left(\frac{a_C^3}{2h_c}\right) sin^{-1}\left(\frac{2h_c}{a_C}\right) - a^2{}_c + 2h^2{}_c\right] \quad \text{(S3)}$$

where h_c cannot be considered constant. However, when both chambers enclose the same volume, the dumbbell is in equilibrium and pressure is equal everywhere (Eq. (13)). Such equivalence allows derivation of a relationship between chamber and conduit heights:

$$h_C = \frac{(2a^2{}_c\, h_{chamber})}{(a^2{}_{chamber} + h^2{}_{chamber})} - \Delta\rho g a^2{}_c h_{chamber} \quad \text{(S4)}$$

With Equation 2, this directly relates chamber volumes and areas of conduit cross sections. Equation S4 has been derived assuming no hydrostatic head of pressure acts in the conduit. In Table S1, conduit heights and areas are computed for a dumbbell containing 4 µl in each chamber and diffusion parameters are calculated for transport of BDNF ($D = 12.6 \times 10^{-7}\ cm^2/s$) [47]. Values are computed for dumbbell geometries used ($m_{mol} = 0.02\ ng$; growth: $h_{chamber} = 1.07\ mm,\ a_{chamber} = 1.42\ mm$; regrowth: $h_{chamber} = 0.85\ mm, a_{chamber} = 1.67\ mm$) pre-axotomy to compare cortical axonal growth, and post-axotomy to analyse regrowth. Supplementary Figure 1C illustrates the linear concentration gradient of BDNF at $t = t_{linear}$, so that its concentration in the right chamber equals C0=0.1 ng/µl and the one in the left chamber is 0.015 ng/µl (0.01 ng/µl initially present in the chamber plus 0.005 ng/µl transferred over t_{linear},).

Supplementary Table 1. Geometrical parameters of dumbbells with different sizes and respective diffusion times of BDNF

Bioassay	Conduit geometry				Diffusion parameters	
	length [mm]	**width [µm]**	**height [µm]**	**area [µm²]**	**t_{steady} [min]**	**t_{linear} [d]**
outgrowth	1	200	5	624	60	30
regrowth	0.5	400	13	3513	15	5

Supplementary table 2: Primary antibodies

Antibody	Target	Host organism	Dilution	Source	Cat #	RRID
Anti-DARPP32, monoclonal	DARPP32	Donkey	1:250	Abcam	ab40801	RRID:AB_731843
Anti-DARPP32, polyclonal	DARPP32	Donkey	1:250	Sigma-Aldrich	HPA048630	RRID:AB_2680468
Anti-MAP2, Polyclonal	Microtubule-associated protein 2	Donkey	1:250	Abcam	ab92434	RRID:AB_2138147
Anti-SMI312, monoclonal	Neurofilament marker (pan axonal, cocktail)	Donkey	1:250	Biolegend	837904	RRID:AB_2566782

Supplementary Table 3: Secondary antibodies

Antibody	Target	Host organism	Dilution	Source	Cat #	RRID
Alexa-Fluor 647	IgG Mouse	Donkey	1:1000	Invitrogen	A31571	RRID:AB_162542
Alexa-Fluor 647	IgG Rabbit	Donkey	1:1000	Invitrogen	A-31570	RRID:AB_2536180
Alexa Fluor 555	IgG Chicken	Donkey	1:1000	LifeTechnology	A78949	RRID:AB_2921071
DAPI (4',6-Diamidino-2-Phenylindole, Dilactate)	DAPI	NA	1:1000	Thermo Fisher Scientific	D1306	RRID:AB_2307445 or RRID:AB_2629482

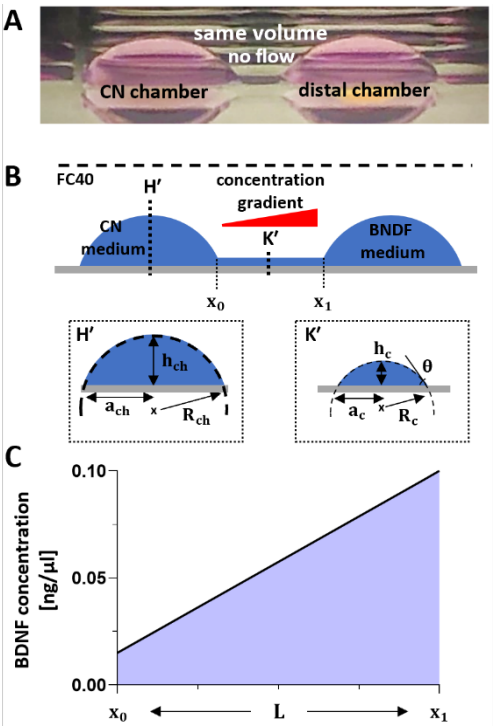

Supplementary Figure 1. Diffusion gradients in fluid-walled dumbbells.

(A) Side view of dumbbell with 4 µl in each chamber. In all examples shown here and elsewhere, the left-hand one hosts cortical neurons.

(B) Schematic of dumbbell with equal volumes. In this case, BDNF molecules diffuse through the conduit, so any axons from CNs will sense a concentration gradient. Lower panels show central cross sections of a chamber and connecting conduit which have shapes of circular segments (as they are bounded by liquid interfaces).

(C) Linear approximation of BDNF concentration gradient inside the conduit at $t = t_{linear}$, when the left chamber ($x < x_0$) contains cortical maturation medium (initially C_{BDNF} = 0.01 ng/µl) and the right one ($x > x_1$) contains cortical maturation medium with 10-fold BDNF concentration.

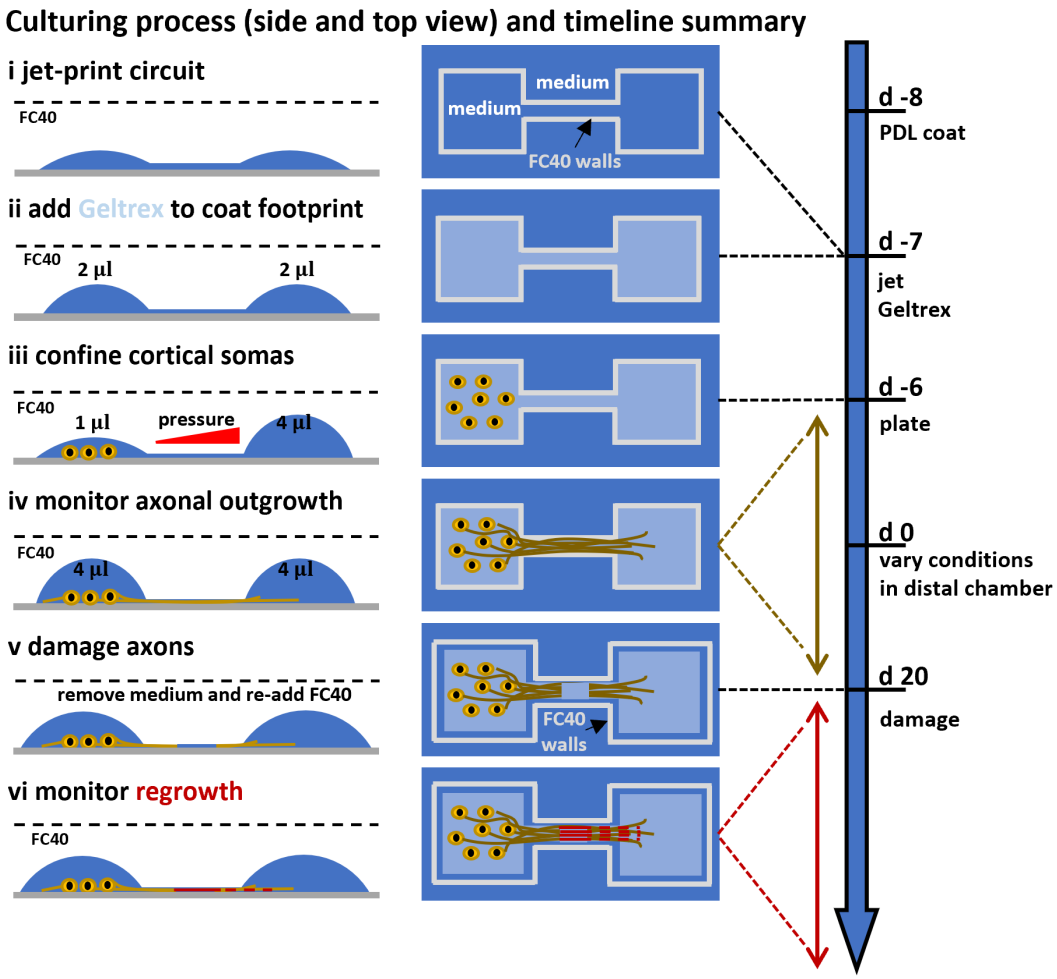

Supplementary Figure 2. Culturing neurons in fluid-walled dumbbells.

Overview of most relevant steps followed to culture CNs and perform axotomy in fluid walled dumbbells (top view, side view, and timeline). The culturing protocol is summarised (from d -8 and d 20) between (i) and (iv). The axotomy assay (from d 20 onwards) is shown in (v) and (vi).

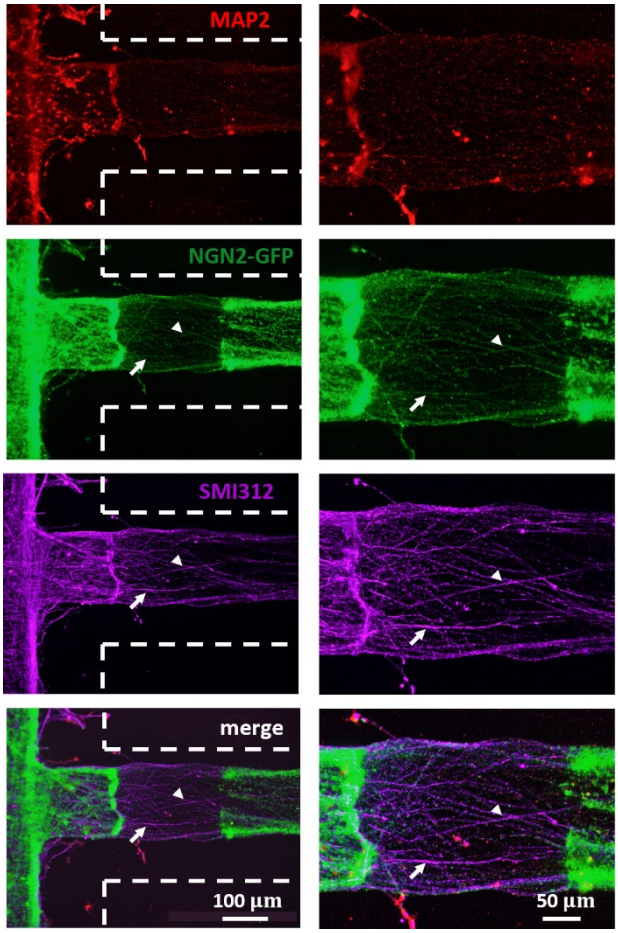

Supplementary Figure 3. Regeneration after axotomy.

NGN2-transfected CNs project axons through the conduit. After 26 days of culture, dumbbells are destroyed, axons damaged and new dumbbells re-built to monitor regrowth of axons. Immunostaining images captured 5 days post axotomy show neuronal-domain markers (MAP2 – red – dendrites, SMI312 – purple – axons) and CN marker NGN2-GFP (green). All regenerated neurites are cortical as they express SMI312 and NGN2-GFP, while dendritic MAP2 is absent (arrow and arrowhead mark two examples). Dashed lines indicate the approximate position of the edges of the newly-built footprint; most regenerated neurites are confined to the footprint of the original dumbbell and the Geltrex coat.

Statement of Authorship for joint/multi-authored papers for PGR thesis

To appear at the end of each thesis chapter submitted as an article/paper

The statement shall describe the candidate's and co-authors' independent research contributions in the thesis publications. For each publication there should exist a complete statement that is to be filled out and signed by the candidate and supervisor **(only required where there isn't already a statement of contribution within the paper itself).**

Title of Paper	**A fluid-walled microfluidic platform for human neuron microcircuits and directed axotomy**
Publication Status	□ Published □ Accepted for Publication **x** Submitted for Publication □Unpublished and unsubmitted
Publication Details	Federico Nebuloni, Quyen Do, Richard Wade-Martins, Peter R. Cook, and Edmond J. Walsh

Student Confirmation

Student Name:	Federico Nebuloni		
Contribution to the Paper	Co-lead author with Quyen Do Designed experiments in discussion with co-authors and performed all parts of experiments in close collaboration with graduate student in biology group (largely Quyen Do provided the biology expertise and I provided the engineering expertise). Data were collected and analysed by both co-lead authors. I led the preparation of the first draft of the manuscript after close discussion with co-lead author on content and layout. I took the responsibility of implementing changes of co-authors and submitting approved documents to journal.		
Signature		Date	10/10/2023

Supervisor Confirmation

By signing the Statement of Authorship, you are certifying that the candidate made a substantial contribution to the publication, and that the description described above is accurate.

Supervisor name and title: Prof. Edmond J. Walsh		
Supervisor comments Federico designed experiments in discussion with co-authors and performed all parts of experiments in close collaboration with graduate student in biology group. Data were collected and analysed by both co-lead authors. Federico led the preparation of the first draft of the manuscript after close discussion with co-lead author on content and layout. He took the responsibility of implementing changes of co-authors and submitting approved documents to journal.		
Signature		Date	12/10/2023

This completed form should be included in the thesis, at the end of the relevant chapter.

Chapter 7: Discussion

This thesis served as a comprehensive analysis of the main characteristics of fluid-walled microenvironments. It proposed to understand properties and fundamental behaviours of liquid interfaces formed between an aqueous phase and a fluorocarbon to expand applications of this technology.

The model derived in **Chapter 4** proposed a model to predict stable concentration gradients generated by diffusion of molecules between parallel laminar streams flowing through a straight fluid-walled conduit. The work highlighted differences and similarities with equivalent studies made in solid PDMS devices (Häusler et al., 2012; Kamholz et al., 1999) and presented the unique characteristics of flows through conduits bounded by fluid walls (Deroy, Stovall-Kurtz, et al., 2021). Such features proved fundamental to derive, and experimentally validate, a mathematical model using a fluorescent tracer of known diffusivity ($D_{th} = 1.07 \times 10^{-10}\ \mathrm{m}^2/\mathrm{s}$) computed using the Einstein-Stokes equations at room temperature. The theoretical predictions provided best fit of experimental gradients when solutions were computed using a diffusion coefficient of $1.1 \times 10^{-10}\ \mathrm{m}^2/\mathrm{s}$ in reasonable agreement with D_{th}. The model has been derived from the advection-diffusion equation assuming steady streams to be infinitely large reservoirs. This assumption simplified the model to a semi-analytical solution that can be applied without need of numerical computations, but it limited the range of flow and geometrical conditions in which such solution can be applied. Results showed great agreement between experimental data and theoretical prediction when Fourier number is of the order of 10^{-2} or smaller. However, those low Fourier numbers usually fit the experimental needs of potential users and similar devices have been already applied to induce chemotactic responses in bacteria (Deroy, Wheeler, et al., 2022; Oliveira et al., 2022) and macrophages (Deroy, Rumianek, et al., 2022). Despite promising results, this system suffered a major shortcoming; flow required usage of external pumps. Such pieces of equipment are not commonly used by biologists and lower the experimental throughput as they require a complex experimental setup – and this may deter

bio-scientists unfamiliar with microfluidic methods. Consequently, there was the need to develop pumping systems that do not rely on external apparatus.

Automatic systems that use differences in intrinsic pressures to drives flows are called ‘passive’. In the last decade, several passive systems have been incorporated into conventional microfluidic devices with solid walls (Goral et al., 2015; Kheiri et al., 2023; Walker & Beebe, 2002). Building on a previous work (Walker & Beebe, 2002), **Chapter 5** introduced a system that exploited the Laplace pressure generated across the fluid walls of a drop (source) to pump its volume through a conduit into a large sink. Here, as the conduit was also confined by fluid walls, its cross-sections morphed as source pressure changes (Deroy, Stovall-Kurtz, et al., 2021), thus previous studies no longer applied (E. Berthier & Beebe, 2007; Chen et al., 2009). This work developed a semi-analytical solution that predicts volumetric flow rates over time as the source drop empties, and validate predictions experimentally. This allowed to estimate the drainage time of the circuit; a key parameter in biological applications (i.e., cells perfusion). However, this solution only applies to shallow source drops (contact angle < ~40°). So, a second (numerical) solution has been proposed to model flow rates regardless of the initial contact angles. Both solutions assumed the fluid walls morph rapidly to accommodate pressure changes. This assumption was confirmed by Calver et al. (2020) who proved the relaxation time of fluid walls is three orders of magnitude smaller than drainage time, thus negligible. Experimental results proved these solutions to be good predictors when hydrostatic components of the pressure are minimised. When the density of the overlay significantly differed from the density of the aqueous phase in the circuit, also theoretical predictions diverged from measured data. Despite these limitations, this work represents a first contribution to allow for more-complex modelling of passive pumping systems in fluid-walled circuits. In general, it proposed a fundamental study to assist design of dynamic (with flow) microfluidic cell cultures inside standard Petri dishes increasing the throughput compared to currently available ones.

An example is represented by **Chapter 6** where a new application of fluid-walled microfluidics into neuroscience was shown. This work proposed to recreate *in vitro* a simplified model of the unidirectional brain circuit between cortex and striatum inside fluid-walled microenvironments

shaped like dumbbells; two chambers connected by a thin conduit in which cells could send projections. Cortical neurons derived from human induced Pluripotent Stem Cells (hiPSCs) are cultured alongside with hiPSCs-derived striatal neurons (Pennartz et al., 2009; Shepherd, 2013). Neuronal populations used in these studies (Ng et al., 2022), have been previously validated in conventional cultures demonstrating expected mature electrophysiological phenotypes (Beccano-Kelly et al., 2023; Hartfield et al., 2014), and correct gene expression (Beevers et al., 2017; Sandor et al., 2017). Additionally, same cells proved to be an excellent model to explore striatal circuitry by using a PDMS microfluidic device where cortical, striatal, and dopaminergic neurons have been co-cultured (Do et al., 2023).

Using fluid walls, the directional connectivity between the two neuronal populations has been achieved plating cortical cells in one chamber, let axons grow and invade the opposite chamber, and then plate striatal cells over cortical axons terminals. As both chambers were always connected and fluid walls prevented use of classical valves to isolate compartments, isolation of neuronal bodies in the desired chamber required alternative methods. Laplace pressure in chamber was controlled by varying the volume in it, and findings of Chapter 5 have been employed to create a pressure gradient against the chamber we wanted to isolate neurons into. Additionally, this chapter introduced a method to sever axons growing in the connecting conduit in a targeted way exploiting the unique ability of fluid walls to be reconfigured/reshaped at need. Fluid walls were destroyed without harming the cultured neurons, axons were damaged around their midpoint by a hydro-jet, and dumbbell circuits rebuilt to quantify regrowth of severed neurites. Results highlighted that the presence of striatal neurons boosted the regrowth of cortical axons inducing a repair like the one showed in presence of the known growth stimulator (BDNF). The damaging method resembled the one proposed by Kimpinsky *et al.* (1997) and Bertrand *et al.* (2005). In contrast to common alternatives that employed vacuum aspiration (Nagendran & Taylor, 2019) or chemicals (L. Li et al., 2012) for severing axons, the one proposed here yielded higher reproducibility and better targeting of the damage site. Although this work represented just a preliminary study, it showed beyond doubt the versatility of fluid-walled environments and it presents the first ‘Organ on Chip’ that uses this technology.

Chapter 8: Conclusions and Future developments

This chapter provides a concise summary of the entire thesis. It highlights the key points from each chapter to address the objectives outlined in Chapter 1. Additionally, it outlines future developments in the chronological order I anticipate they can be accomplished.

Conclusions

The literature review in **Chapter 2** set the context with a detailed overview of the evolution of microfluidics. It started from first observations of fluidic phenomena at the microscale to end with the onset of latest open microfluidic technologies. It described technological advances and limitations that induced such transformation.

Microfluidics with fluid walls has been introduced in **Chapter 3**. This section presented the geometry of main microenvironments used throughout the thesis (sessile drops and conduits). Additionally, it derived equations describing pressure and shape of morphing fluid walls of a conduit during laminar flow.

Chapter 4 replicated the design of a classic microfluidic (T-)H-sensor, though here bounded by fluid walls, able to generate stable diffusion concentration gradients of solutes flowing in parallel laminar streams. Building upon the solution for flow in a conduit with fluid walls, a semi-analytical solution for diffusion has been derived. This differed from more classical solution due to the shape of the conduit and flexibility of fluid boundaries which were accounted for throughout the theoretic analysis. The theory was validated with a wide range of experiments and all data was found to collapse onto a single 2-D equation.

Chapter 5 presented a simple passive system that exploits Laplace pressure to drive flow from a source drop to an infinitely large sink through a fluid-bounded conduit. A semi-analytical solution predicting volumetric variations of the source drop over time has been derived and experimentally validated assuming negligible any gravitational effect. Such solution enabled to estimate the drainage time of the source drop with less than 10% error.

Chapter 6 introduced a novel fluid-walled microenvironment aimed promoting unidirectional connections between different neuronal populations to mimic basic electrical circuits of the

brain. Here, a simple model of the cortex-striatum circuit has been recreated inside dumbbell-shaped environments. Results showed the correct directional growth of hiPSC-derived cortical axons towards hiPSC-derived striatal neurons. Finally, this chapter introduced a method to induce a targeted and localised damage to the connecting axons exploiting properties of fluid walls. Such method has been employed to propose an assay to screen for pro-regenerative drugs post injury.

In general, if interfaces between immiscible liquids are well-known, they have only been recently employed as bounding walls for microfluidics. This thesis has explored properties of such fluid walls to maximise the biological applications. By reducing complex phenomena into simple models, it wishes to democratize microfluidics and make it accessible to most bio-scientists.

Future developments

Laplace pressure in drops with non-circular footprints

The Laplace pressure is the pressure drop between the two sides of a curved liquid interface. It is determined by the Young-Laplace equation that depends on surface tension and the radii of curvature of the interfacial surface (Chapter 3). Such radii depend on the three-dimensional shape of the interface which arrange itself to minimise its energy. In nature, liquid interfaces are always spherical if not deformed by the environments (e.g., a perfect sphere for bubbles, and the cap of a sphere for drops laying on a flat substrate). When drop have non-circular footprints their interfacial surface is distorted and their shape its currently under analysis (Ravazzoli et al., 2016; Wray & Moore, 2023). Fluid-walled microfluidics enables creation of drops with almost any imaginable 2D footprint. As microfluidic devices are usually asked to have a very high throughput, microenvironments need to be tessellated so to exploit the whole substrate surface. It is evident that circular chambers are not ideal to be tessellated as their packing efficiency is very low compared to polygons. Therefore, there is a need to develop a robust theory that enables prediction of the pressure inside a drop with a non-circular footprint.

In the case of drops shaped like spherical caps, Laplace pressure is calculated simply knowing the footprint radius and the volume contained. However, this no longer applies when the interfacial surface is distorted by polygonal footprints. A direct comparison of the relative pressures of circular and non-circular drops becomes possible by connecting the two and letting them reach equilibrium. For instance, the footprints of main polygons can be approximated with their inscribed circumferences, and the method in Figure 10 can provide one way of verifying or discarding analytical solutions.

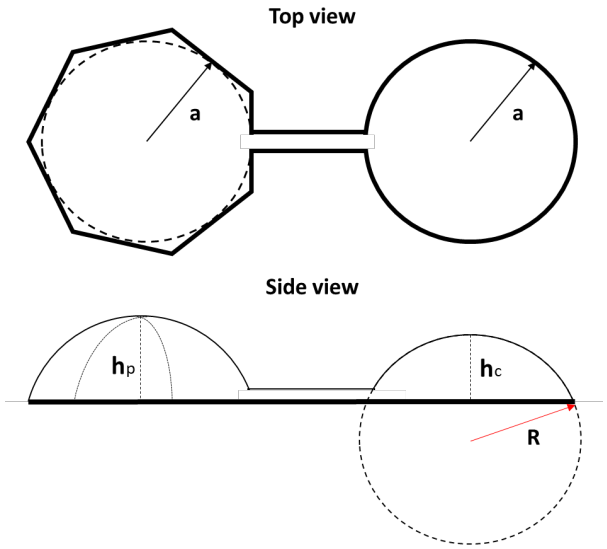

Figure 10. Laplace Pressure in non-circular drops – experimental design.
Top and side view schematics of a circular drop connected to a non-circular one by a small conduit. At equilibrium they experience the same pressure. The left droplet is created over a heptagonal footprint and represents the unknown, while the right one has a circular footprint whose pressure is known through the radius R.

Three-dimensional (3D) cultures within fluid-walled microfluidics

If two-dimensional cultures benefit from low cost and simplicity, they fail to mimic the correct cell-to-cell interactions which are 3D *in vivo* (Mark et al., 1977). Figure 11A illustrates a method for creating drop-shaped hydrogel scaffolds and integrating them into fluid-walled microenvironments. Cell-laden uncross-linked hydrogel drops are deposited in a standard Petri dish. The still-liquid droplets turn into solid hydrogels via polymerization processes that differ according to the hydrogel type. Most used hydrogels are the bovine/rat collagen-based ones

due to their excellent compatibility, as their structure is both chemically and structurally similar the native extracellular matrix. Collagen gels polymerize via thermal treatment at 37°C and this makes them particularly suited for simple cells encapsulation while the matrix is forming. Then, fluid walls can be created as usual. Drop-shaped hydrogel scaffolds are so integrated into accessible environments. Preliminary experiments show hydrogel drop (with fluorescent beads to mimic cells) integrated into fluid-walled chambers of different size and shape (Figure 11B,C).

Due to its fluid nature, this approach restricts hydrogel scaffold to be shaped like drops and it does not easily allow for complex multi-layered structures. Nevertheless, its simplicity has the potential to make it a great candidate for quick preliminary drug screening test on 3D cell cultures (Figure 11B) and co-cultures (Figure 11C).

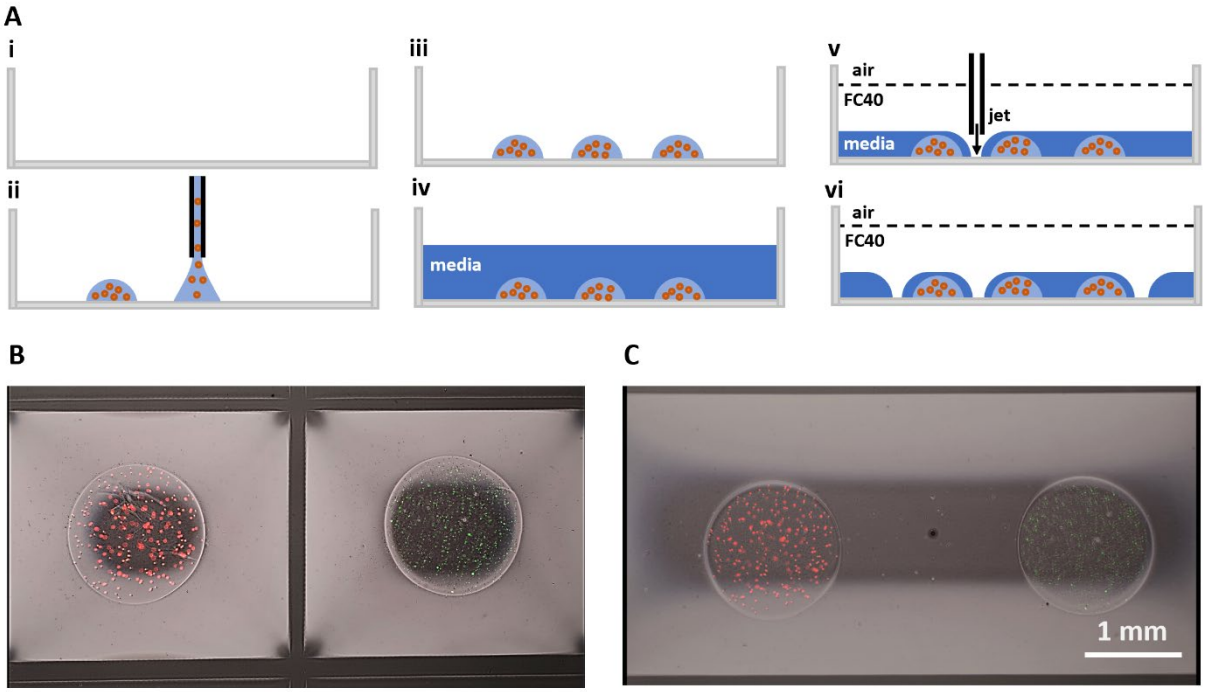

Figure 11. Hydrogel scaffolds.

(A) Hydrogels drop deposition and integration into fluid-walled microfluidics. (i) A virgin Petri dish. (ii) Sub microlitre drops of cell-laden uncross-linked hydrogel are deposited in the dish. (iii) Drops are let crosslink. (iv) Once hydrogel solidifies, drops can be submerged in cell media without dissolving. (v) fluid walls can now be formed as usual. (vi) drop-shaped hydrogel scaffolds are now integrated into microfluidic cultures with fluid walls.

(B) Two drop-shaped Geltrex scaffolds (~500 nl) containing different fluorescent beads are isolated into adjacent fluid-walled square chambers. Image was obtained overlapping three images: phase-contrast, green fluorescence, and a red fluorescence.

(C) Two drop-shaped Geltrex scaffolds (~500 nl) containing different fluorescent beads are ‘co-cultured’ in the same fluid-walled rectangular chamber. Image was obtained overlapping three images: phase-contrast, green fluorescence, and a red fluorescence.

Connecting of neuronal 3D cultures/organoids

This thesis showed the importance of recreating neuronal circuits in vitro, however, the model proposed in Chapter 6 enables connections between 2D cultures. There is, therefore, the need to create connections between 3D cultures of neurons. Neuronal cells can be encapsulated into hydrogel scaffolds formed in standard Petri dishes and submerged in cell-growth medium (Figure 12A). Preliminary experiments with iPSCs-derived Ngn2 neurons show axons to grow outside hydrogel scaffold to form connections with adjacent cells to form a network (Figure 12B). Hydrogel scaffolds can be integrated in fluid-walled circuits to select growth direction and connections (Figure 12C). Here, cell-laden hydrogels are confined in square chambers and axonal projections can only grow in the connecting conduits (Figure 12D). Depending on the design of the microenvironments connections between 3D cultures are allowed or prevented, enabling users to create the neural network desired.

The ultimate aim is to develop a platform where different organoids can be connected into a functional network. The proposed system opens to the futuristic idea of an Organoid Intelligence presented recently (Smirnova et al., 2023).

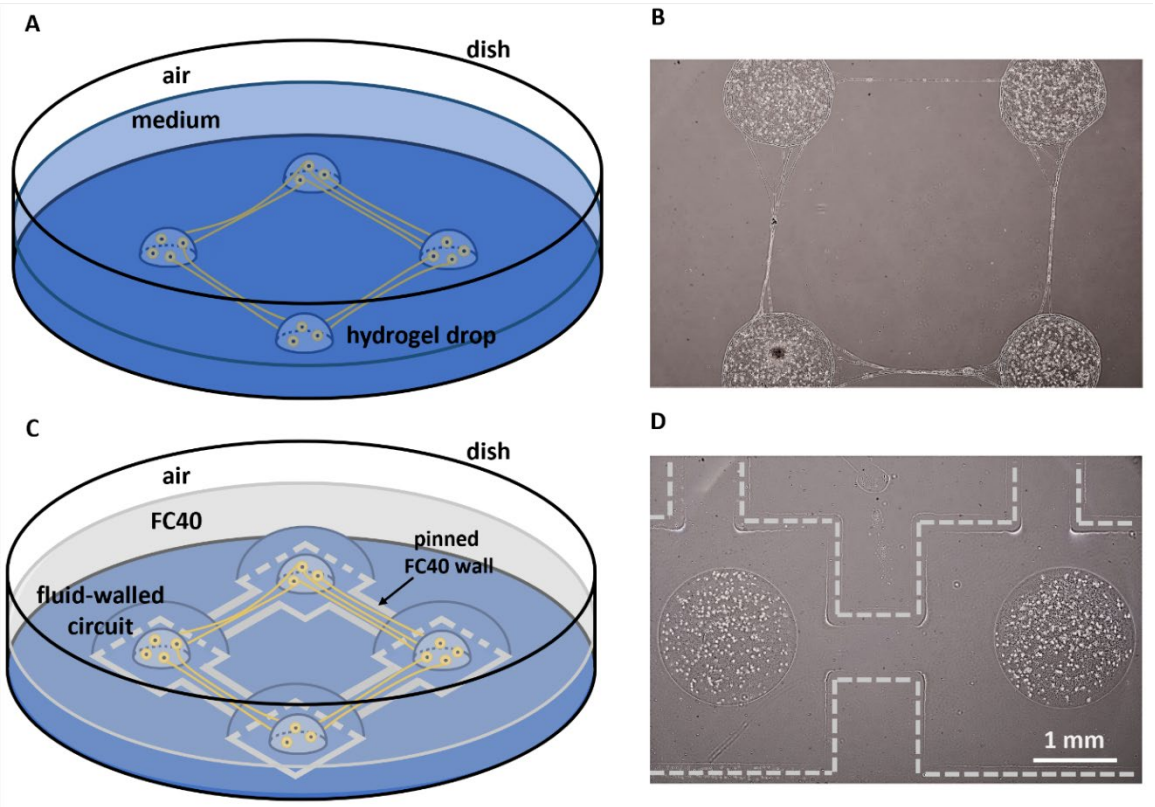

Figure 12. Connecting 3D neuronal cultures.

(A) Schematic of a Petri dish with 3D neuronal cultures. Drop-shaped hydrogels scaffolds containing neuronal cell bodies are submerges in medium. Neurites grow between scaffolds to form connections.

(B) Inverted microscope phase-contrast image of four 500 nl Geltrex drop-shaped scaffolds with iPSCs-derived Ngn2 neurons submerged in cortical maturation medium 18 days after plating. Projections automatically form connections between adjacent scaffold creating a network.

(C) Schematic of a Petri dish with 3D neuronal cultures inside a fluid-walled network. Any microfluidics circuit can be formed around solid cell-laden hydrogels. 3D cultures are contained in square chambers connected by thin conduits. The dish represents the only solid boundary of the system.

(D) Inverted microscope phase-contrast image of two 500 nl Geltrex drop-shaped scaffolds with Ngn2 neurons inside a fluid-walled network. This preliminary image shows cells just after plating, so no connections have been formed yet.

References

Ayuso, J. M., Virumbrales-Muñoz, M., Lang, J. M., & Beebe, D. J. (2022). A role for microfluidic systems in precision medicine. *Nature Communications*, *13*(1), 3086.

Battat, S., Weitz, D., & Whitesides, G. (2022). An outlook on microfluidics: the promise and the challenge. *Lab on a Chip*, *22*(3), 530–536.

Beccano-Kelly, D. A., Cherubini, M., Mousba, Y., Vowles, J., Cowley, S., & Wade-Martins, R. (2023). Calcium dysregulation combined with mitochondrial failure and electrophysiological maturity converge in Parkinson's iPSC-dopamine neurons. *Iscience*, *26*(7).

Beevers, J. E., Lai, M. C., Collins, E., Booth, H. D. E., Zambon, F., Parkkinen, L., Vowles, J., Cowley, S. A., Wade-Martins, R., & Caffrey, T. M. (2017). MAPT genetic variation and neuronal maturity alter isoform expression affecting axonal transport in iPSC-derived dopamine neurons. *Stem Cell Reports*, *9*, 587–599.

Berry, J. D., Neeson, M. J., Dagastine, R. R., Chan, D. Y. C., & Tabor, R. F. (2015). Measurement of surface and interfacial tension using pendant drop tensiometry. In *Journal of Colloid and Interface Science* (Vol. 454, pp. 226–237). Academic Press Inc.

Berthier, E., & **Beebe**, D. (2014). Gradient generation platforms: new directions for an established microfluidic technology. *Lab on a Chip*, *14*(17), 3241–3247.

Berthier, E., & **Beebe**, D. J. (2007). Flow rate analysis of a surface tension driven passive micropump. *Lab on a Chip*, *7*(11), 1475–1478.

Berthier, E., Young, E. W. K., & Beebe, D. (2012). Engineers are from PDMS-land, biologists are from polystyrenia. In *Lab on a Chip* (Vol. 12, Issue 7, pp. 1224–1237). Royal Society of Chemistry.

Berthier, J., **Brakke**, K. A., & **Berthier**, E. (2016). *Open Microfluidics*. Wiley.

Bertrand, J., Winton, M. J., Rodriguez-Hernandez, N., Campenot, R. B., & Mckerracher, L. (2005). Application of Rho antagonist to neuronal cell bodies promotes neurite growth in compartmented cultures and regeneration of retinal ganglion cell axons in the optic. *Journal of Neuroscience*, *25*(5), 1113–1121.

Beverung, C. J., Radke, C. J., & Blanch, H. W. (1999). Protein adsorption at the oil/water interface: characterization of adsorption kinetics by dynamic interfacial tension measurements. *Biophysical Chemistry*, *81*(1), 59–80.

Bhatia, S., & **Ingber**, D. (2014). Microfluidic organs-on-chips. *Nature Biotechnology*, *32*(8), 760–772.

Calver, S. N., Gaffney, E. A., Walsh, E. J., Durham, W. M., & Oliver, J. M. (2020). On the thin-film asymptotics of surface tension driven microfluidics. *Journal of Fluid Mechanics*, *901*.

Carraro, A., Hsu, W. M., Kulig, K. M., Cheung, W. S., Miller, M. L., Weinberg, E. J., Swart, E. F., Kaazempur-Mofrad, M., Borenstein, J. T., Vacanti, J. P., & Neville, C. (2008). In vitro analysis of a hepatic device with intrinsic microvascular-based channels. *Biomedical Microdevices*, *10*(6), 795–805.

Casavant, B. P., Berthier, E., Theberge, A. B., Berthier, J., Montanez-Sauri, S. I., Bischel, L. L., Brakke, K., Hedman, C. J., Bushman, W., Keller, N. P., & Beebe, D. J. (2013). Suspended microfluidics. *Proceedings of the National Academy of Sciences of the United States of America*, *110*(25),

Chen, I. J., Eckstein, E. C., & Lindner, E. (2009). Computation of transient flow rates in passive pumping micro-fluidic systems. *Lab on a Chip*, *9*(1), 107–114.

Deroy, C., **Nebuloni**, F., Cook, P. R., & Walsh, E. J. (2021). Microfluidics on Standard Petri Dishes for Bioscientists. *Small Methods*, *5*(11).

Deroy, C., **Rumianek**, A. N., Wheeler, J. H. R., Nebuloni, F., Cook, P. R., Greaves, D. R., & Walsh, E. J. (2022). Assaying Macrophage Chemotaxis Using Fluid-Walled Microfluidics. *Advanced Materials Technologies*, *7*(9), 2200279.

Deroy, C., **Stovall-Kurtz**, N., Nebuloni, F., Soitu, C., Cook, P. R., & Walsh, E. J. (2021). Predicting flows through microfluidic circuits with fluid walls. *Microsystems & Nanoengineering 2021 7:1*, *7*(1), 1–9.

Deroy, C., Wheeler, J. H. R., Rumianek, A. N., Cook, P. R., Durham, W. M., Foster, K. R., & Walsh, E. J. (2022). Reconfigurable Microfluidic Circuits for Isolating and Retrieving Cells of Interest. *ACS Applied Materials & Interfaces*, *14*(22), 25209–25219.

Do, Q. B., Ng, B., Marquez Gomez, R., Beccano-Kelly, D., Ibarra-Aizpura, N., Caiazza, M.-C., Lang, C., Baleriola, J., Bengoa-Vergniory, N., & Wade-Martins, R. (2023). Early striatal hyperexcitability in an in vitro human striatal microcircuit model carrying the Parkinson's GBA-N370S mutation. *BioRxiv*.

Esch, E., Bahinski, A., & Huh, D. (2015). Organs-on-chips at the frontiers of drug discovery. *Nature Reviews Drug Discovery*, *14*(4), 248–260.

Ferrari, E., & **Rasponi**, M. (2021). Liver–Heart on chip models for drug safety. *APL Bioengineering*, *5*(3).

Ferrari, E., Visone, R., Monti, E., Torretta, E., Moretti, M., Occhetta, P., & Rasponi, M. (2023). LivHeart: A Multi Organ-on-Chip Platform to Study Off-Target Cardiotoxicity of Drugs Upon Liver Metabolism. *Advanced Materials Technologies*, *8*(8), 2201435.

Friedman, A. A., Letai, A., Fisher, D. E., & Flaherty, K. T. (2015). Precision medicine for cancer with next-generation functional diagnostics. *Nature Reviews Cancer*, *15*(12), 747–756.

Goral, V. N., Tran, E., & Yuena, P. K. (2015). A pump-free membrane-controlled perfusion microfluidic platform. *Biomicrofluidics*, *9*(5).

Harris, S. G., & Shuler, M. L. (2003). Growth of endothelial cells on microfabricated silicon nitride membranes for an In Vitro model of the blood-brain barrier. *Biotechnology and Bioprocess Engineering*, *8*(4), 246–251.

Hartfield, E. M., Yamasaki-Mann, M., Ribeiro Fernandes, H. J., Vowles, J., James, W. S., Cowley, S. A., & Wade-Martins, R. (2014). Physiological characterisation of human iPS-derived dopaminergic neurons. *PLoS ONE*, *9*(2).

Häusler, E., Domagalski, P., Ottens, M., & Bardow, A. (2012). Microfluidic diffusion measurements: The optimal H-cell. *Chemical Engineering Science*, *72*, 45–50.

Huh, D., Fujioka, H., Tung, Y. C., Futai, N., Paine, R., Grotberg, J. B., & Takayama, S. (2007). Acoustically detectable cellular-level lung injury induced by fluid mechanical stresses in microfluidic airway systems. *Proceedings of the National Academy of Sciences of the United States of America*, *104*(48), 18886–18891.

Huh, D., Kim, H., Fraser, J., Shea, D., Khan, M., Bahinski, A., Hamilton, G., & Ingber, D. (2013). Microfabrication of human organs-on-chips. *Nature Protocols, 8*(11), 2135–2157.

Huh, D., Matthews, B. D., Mammoto, A., Montoya-Zavala, M., Yuan Hsin, H., & Ingber, D. E. (2010). Reconstituting organ-level lung functions on a chip. *Science*, *328*(5986), 1662–1668.

Jang, K., Sato, K., Igawa, K., Chung, U. Il, & Kitamori, T. (2008). Development of an osteoblast-based 3D continuous-perfusion microfluidic system for drug screening. *Analytical and Bioanalytical Chemistry*, *390*(3), 825–832.

Jang, K., & Suh, K. (2010). A multi-layer microfluidic device for efficient culture and analysis of renal tubular cells. *Lab on a Chip*, *10*, 36–42.

Kamholz, A. E., Weigl, B. H., Finlayson, B. A., & Yager, P. (1999). Quantitative analysis of molecular interaction in a microfluidic channel: The T-sensor. *Analytical Chemistry*, *71*(23), 5340–5347.

Kheiri, S., Chen, Z., Yakavets, I., Rakhshani, F., Young, E. W. K., & Kumacheva, E. (2023). Integrating spheroid-on-a-chip with tubeless rocker platform: A high-throughput biological screening platform. *Biotechnology Journal*.

Kim, J., Taylor, D., Agrawal, N., Wang, H., Kim, H., Han, A., Rege, K., & Jayaraman, A. (2012). A programmable microfluidic cell array for combinatorial drug screening. *Lab on a Chip*, *12*(10), 1813–1822.

Kimpinski, K., Campenot, R. B., & Mearow, K. (1997). Effects of the neurotrophins nerve growth factor, neurotrophin-3, and brain-derived neurotrophic factor (BDNF) on neurite growth from adult sensory neurons in compartmented cultures. *Journal of Neurobiology*, *33*(5), 395–410.

Kimura, H., Yamamoto, T., Sakai, H., Sakai, Y., & Fujii, T. (2008). An integrated microfluidic system for long-term perfusion culture and on-line monitoring of intestinal tissue models. *Lab on a Chip*, *8*(5), 741–746.

Lam, M., Huang, Y., Birla, R., & Takayama, S. (2009). Microfeature guided skeletal muscle tissue engineering for highly organized 3-dimensional free-standing constructs. *Elsevier*, *30*, 1150–1155.

Lee, P., Hung, P., & Lee, L. (2007). An artificial liver sinusoid with a microfluidic endothelial-like barrier for primary hepatocyte culture. *Biotechnology and Bioengineering*, *97*(5), 1340–1346.

Li, C., Hite, Z., Warrick, J. W., Li, J., Geller, S. H., Trantow, V. G., Mcclean, M. N., & Beebe, D. J. (2020). Under oil open-channel microfluidics empowered by exclusive liquid repellency. *Science Advances*, *6*(16), eaay9919.

Li, L., Ren, L., Liu, W., Wang, J. C., Wang, Y., Tu, Q., Xu, J., Liu, R., Zhang, Y., Yuan, M. Sen, Li, T., & Wang, J. (2012). Spatiotemporally controlled and multifactor involved assay of neuronal compartment regeneration after chemical injury in an integrated microfluidics. *Analytical Chemistry*, *84*(15), 6444–6453.

Low, L., Mummery, C., Berridge, B., & Austin, C. (2021). Organs-on-chips: into the next decade. *Nature Reviews Drug Discovery*, *20*(5), 345–361.

Mahler, G., Esch, M., Glahn, R., & Shuler, M. (2009). Characterization of a gastrointestinal tract microscale cell culture analog used to predict drug toxicity. *Biotechnology and Bioengineering*, *104*(1), 193–205.

Mark, K. Von Der, Gauss, V., Mark, H. Von Der, & Müller, P. (1977). Relationship between cell shape and type of collagen synthesised as chondrocytes lose their cartilage phenotype in culture. *Nature*, *267*(5611), 531–532.

Marsano, A., Conficconi, C., Lemme, M., Occhetta, P., Gaudiello, E., Votta, E., Cerino, G., Redaelli, A., & Rasponi, M. (2016). Beating heart on a chip: a novel microfluidic platform to generate functional 3D cardiac microtissues. *Lab on a Chip*, *16*(3), 599–610.

Mastrangeli, M., Millet, S., & Raaij, J. van den E. (2019). *Organ-on-chip in development: Towards a roadmap for organs-on-chip*.

Mata, A., Fleischman, A. J., & Roy, S. (2005). Characterization of Polydimethylsiloxane (PDMS) Properties for Biomedical Micro/Nanosystems. *Biomedical Microdevices*, *7*(4), 281–293.

Mazutis, L., & Griffiths, A. (2012). Selective droplet coalescence using microfluidic systems. *Lab on Chip*, *12*(10), 1800–1806.

Nagendran, T., & **Taylor**, A. M. (2019). Unique Axon-to-Soma Signaling Pathways Mediate Dendritic Spine Loss and Hyper-Excitability Post-axotomy. *Frontiers in Cellular Neuroscience*, *13*, 431.

Ng, B., Vowles, J., Beccano-Kelly, D., Stefana, M. I., O'Brien, D. P., Bengoa-Vergniory, N., Betherat, F., Abey, A., Carling, P., & Kilfeather, P. (2022). Tau depletion in human neurons mitigates Aβ-driven toxicity. *BioRxiv*, 2012–2022.

Oliveira, N. M., Wheeler, J. H. R., Deroy, C., Booth, S. C., Walsh, E. J., Durham, W. M., & Foster, K. R. (2022). Suicidal chemotaxis in bacteria. *Nature Communications*, *13*(1), 7608.

Pennartz, C. M. A., Berke, J. D., Graybiel, A. M., Ito, R., Lansink, C. S., van der Meer, M., David Redish, A., Smith, K. S., & Voorn, P. (2009). Corticostriatal interactions during learning, memory processing, and decision making. *Journal of Neuroscience*, *29*, 12831–12838.

Ravazzoli, P., González, A., & Diez, J. (2016). Drops with non-circular footprints. *Physics of Fluids*, *28*(4).

Rohr, S., Scholly, D. M., & Kleber, A. G. (1991). Patterned growth of neonatal rat heart cells in culture. Morphological and electrophysiological characterization. *Circulation Research*, *68*(1), 114–130.

Sackmann, E. K., Fulton, A. L., & Beebe, D. J. (2014). The present and future role of microfluidics in biomedical research. In *Nature* (Vol. 507, Issue 7491, pp. 181–189). Nature Publishing Group.

Sandor, C., Robertson, P., Lang, C., Heger, A., Booth, H., Vowles, J., Witty, L., Bowden, R., Hu, M., Cowley, S. A., Wade-Martins, R., & Webber, C. (2017). Transcriptomic profiling of purified patient-derived dopamine neurons identifies convergent perturbations and therapeutics for Parkinson's disease. *Human Molecular Genetics*, *26*(3), 552–566.

Savart, F. (1833). Memoire sur la constitution des veines liquids lancees par des orifices circulaires en mince paroi. *Annales de Chimie*, *53*, 337–386.

Shehab, N., Lovegrove, M. C., Geller, A. I., Rose, K. O., Weidle, N. J., & Budnitz, D. S. (2016). US emergency department visits for outpatient adverse drug events, 2013-2014. *JAMA*, *316*(20), 2115–2125.

Shepherd, G. (2013). Corticostriatal connectivity and its role in disease. *Nature Reviews Neuroscience*, *14*, 278–291.

Smirnova, L., Caffo, B. S., Gracias, D. H., Huang, Q., Morales Pantoja, I. E., Tang, B., Zack, D. J., Berlinicke, C. A., Boyd, J. L., Harris, T. D., Johnson, E. C., Kagan, B. J., Kahn, J., Muotri, A. R., Paulhamus, B. L., Schwamborn, J. C., Plotkin, J., Szalay, A. S., Vogelstein, J. T., … Hartung, T. (2023). Organoid intelligence (OI): the new frontier in biocomputing and intelligence-in-a-dish. *Frontiers in Science*, *0*, 0.

Soitu, C., Feuerborn, A., Deroy, C., Castrejón-Pita, A. A., Cook, P. R., & Walsh, E. J. (2019). Raising fluid walls around living cells. *Science Advances*, *5*(6), 8002–8007.

Soitu, C., Feuerborn, A., Tan, A. N., Walker, H., Walsh, P. A., Castrejón-Pita, A. A., Cook, P. R., & Walsh, E. J. (2018). Microfluidic chambers using fluid walls for cell biology. *Proceedings of the National Academy of Sciences of the United States of America*, *115*(26), E5926–E5933.

Soitu, C., Stovall-Kurtz, N., Deroy, C., Castrejón-Pita, A. A., Cook, P. R., & Walsh, E. J. (2020). Jet-Printing Microfluidic Devices on Demand. *Advanced Science*, *7*(23), 2001854.

Song, J. W., Gu, W., Futai, N., Warner, K. A., Nor, J. E., & Takayama, S. (2004). Computer-controlled microcirculatory support system for endothelial cell culture and shearing. *ACS Publications*, *4*(6),

Strutt of Rayleigh, J. (1879). VI. On the capillary phenomena of jets. *Proceedings of the Royal Society of London*, *29*(196–199), 71–97.

Sweet, R. (1965). High frequency recording with electrostatically deflected ink jets. *Review of Scientific Instruments*, *36*(2), 131–136.

Viravaidya, K., Sin, A., & Shuler, M. (2004). Development of a microscale cell culture analog to probe naphthalene toxicity. *Biotechnology Progress*, *20*(1), 316–323.

Walker, G. M., & **Beebe**, D. J. (2002). A passive pumping method for microfluidic devices. *Lab on a Chip*, *2*(3), 131–134.

Walsh, E. J., Feuerborn, A., Wheeler, J. H. R., Tan, A. N., Durham, W. M., Foster, K. R., & Cook, P. R. (2017). Microfluidics with fluid walls. *Nature Communications*, *8*(1), 816.

Ward, A. J. I., & **Regan**, L. H. (1980). Pendant Drop Studies of Adsorbed Films of Bovine Serum Albumin I. Interfacial Tensions at the Isooctane/Water Interface. *Journal of Colloid and Interface Science*, *78*(2), 395–400.

Whitesides, G. M. (2006). The origins and the future of microfluidics. In *Nature* (Vol. 442, Issue 7101, pp. 368–373).

Wray, A., & **Moore**, M. (2023). Evaporation of non-circular droplets. *Journal of Fluid Mechanics*, *961*, A11.

Yu, J., Berthier, E., Craig, A., de Groot, T. E., Sparks, S., Ingram, P. N., Jarrard, D. F., Huang, W., Beebe, D. J., & Theberge, A. B. (2019). Reconfigurable open microfluidics for studying the spatiotemporal dynamics of paracrine signalling. *Nature Biomedical Engineering 2019 3:10*, *3*(10), 830–841.

Zhang, Q., Feng, S., Lin, L., Mao, S., & Lin, J. (2021). Emerging open microfluidics for cell manipulation. *Chemical Society Reviews*, *50*(9), 5333–5348.

Zhou, J., & **Papautsky**, I. (2013). Fundamentals of inertial focusing in microchannels. *Lab on a Chip*, *13*(6), 1121–1132.